

# Modal Identification of Time-varying Structures Using the Blind Source Separation Techniques

by

Faizuddin Musafere

A thesis submitted to the faculty of the Lakehead University in partial  
fulfillment of the requirements for the degree of

Master of Science in  
Mechanical Engineering

Thunder Bay, Ontario, Canada, 2015

© Faizuddin Musafere, 2015

## **Abstract**

In last few decades, Structural Health Monitoring (SHM) has been an indispensable subject in the field of vibration engineering. With the aid of modern sensing technology, SHM has garnered significant attention towards diagnosis and risk management of large-scale civil and mechanical structures. In SHM, system identification is one of major building blocks through which unknown system parameters are extracted from vibration data of the structures. Such system information is then utilized to detect the damage instant, severity and extent to rehabilitate and prolong the existing health of the structures. In recent years, Blind Source Separation (BSS) has become one of the newly emerging advanced signal processing techniques for output-only system identification of structures. This is attractive for large structures since the input information is not readily available.

In this work, two new damage detection techniques are proposed integrating a special class of BSS known as Second-Order Blind Identification (SOBI); first with the Hilbert transform (HT) and second with the time-varying auto-regressive (TVAR) modeling to track the change of modal parameters of the structure. The proposed method is validated considering discrete damage cases in a suite of numerical studies and experimental models followed by a full-scale structure. The results are then compared with Finite Element (FE) modeling in case of lab-scale study and with the stochastic subspace identification (SSI) method in the case of full-scale structure. The proposed method (SOBI with TVAR) is then employed to identify the instantaneous frequencies (IF) of an axially-moving cantilever beam simulating the case of progressive damage. Identification of the IFs is also carried out using three different algorithms namely the wavelet transform (WT), the Hilbert vibration decomposition (HVD), and the HVD plus the TVAR modeling.

## **Acknowledgements**

I would like to express my deepest gratitude to my supervisor Dr. Kefu Liu for his valuable guidance, patience and encouragement for the course of this study. I greatly appreciate my co-supervisor Dr. Ayan Sadhu for his guidance and valuable suggestions. I wish to thank both my supervisors for introducing me to the challenging field of System Identification and Structural Health Monitoring. This thesis would not have been possible without their supervision.

I am grateful to Dr. Meilan Liu from the Department of Mechanical Engineering and Dr. Yanglin Gong from the Department of Civil Engineering for reviewing my thesis. I would like to thank Mr. Kailash Bhatia for his assistance in the machine shop. I would like to thank Dr. Sadhu's undergraduate students Matthew Bullock, Scott Klasens, Jordan Mitchelmore and Phil Sidorenko for the Finite Element modeling of the experimental model and all other friends that I came across during my stay at Thunder Bay, Ontario.

I wish to extend my utmost thanks to my wife Benafsha, my parents, and my siblings for their invaluable love, patience and courage to undertake this work. This work could not have been completed without them.

# **Dedication**

To Benafsha, my parents, and my siblings

# Table of Contents

<b>Abstract</b> .....	<b>ii</b>
<b>Acknowledgements</b> .....	<b>iii</b>
<b>Dedication</b> .....	<b>iv</b>
<b>Table of Contents</b> .....	<b>v</b>
<b>List of Figures</b> .....	<b>vii</b>
<b>List of Tables</b> .....	<b>x</b>
<b>List of Abbreviations</b> .....	<b>xi</b>
<b>Chapter 1 Introduction</b> .....	<b>1</b>
1.1 Overview .....	1
1.2 Literature Review on Time-varying System Identification.....	2
1.2.1 The Parametric Damage Detection Methods.....	2
1.2.2 The Non-parametric Damage Detection Methods.....	3
1.3 Blind Source Separation (BSS).....	3
1.4 Objectives.....	4
1.5 Thesis Outline .....	5
<b>Chapter 2 Damage Detection Based on Blind Source Separation</b> .....	<b>7</b>
2.1 Proposed Algorithm .....	7
2.1.1 Second-Order Blind Identification (SOBI).....	7
2.1.2 The Hilbert Transform.....	12
2.1.3 Time-varying Auto-Regressive (TVAR) Modeling .....	16
2.2 Damage-Based Studies: Identification of Damage Instant and Modal Parameters.....	18
2.3 Summary .....	28
<b>Chapter 3 Experimental Studies</b> .....	<b>29</b>
3.1 Experimental Setup .....	29
3.2 Damage Cases .....	30
3.2.1 Damage Identification in $C_1$ .....	31
3.2.2 Damage Identification in $C_2$ .....	36

3.3 Full-Scale Study .....	41
3.4 Summary .....	45
<b>Chapter 4 Identification of Instantaneous Frequencies of an Axially-Moving Cantilever Beam.....</b>	<b>46</b>
4.1 Dynamic Model of an Axially-Moving Cantilever Beam.....	46
4.2 Estimation of the Instantaneous Frequencies through the TVAR Modelling .....	50
4.3 Computer Simulation .....	51
4.4 Experimental Setup .....	59
4.5 The Wavelet Transform (WT).....	61
4.6 Identification of the Instantaneous Frequencies of the Axially-Moving Cantilever Beam Using the Wavelet Transform .....	64
4.7 The Hilbert Vibration Decomposition (HVD) .....	72
4.7.1 Instantaneous Frequency (IF) of the Largest Energy Component.....	72
4.7.2 Envelope of the Largest Energy Component.....	75
4.8 Identification of the Instantaneous Frequencies of the Axially-Moving Beam Using the HVD method .....	77
4.9 Identification of the Instantaneous Frequencies of the Axially-moving Beam Using the HVD Method plus the TVAR Modelling.....	87
4.10 Summary .....	90
<b>Chapter 5 Conclusions and Future Works.....</b>	<b>92</b>
5.1 Conclusions .....	92
5.2 Contributions.....	93
5.3 Future Works.....	94
<b>References.....</b>	<b>95</b>

## List of Figures

Figure 2.1: Sources $s_1(t)$ (blue) and $s_2(t)$ (red) obtained from the SOBI are temporally uncorrelated .....	11
Figure 2.2: Sources $s_1(t)$ and $s_2(t)$ obtained from the SOBI are spatially uncorrelated .....	12
Figure 2.3: Drawbacks associated with the Hilbert transform.....	15
Figure 2.4: Flowchart of the proposed method.....	18
Figure 2.5: Mode shapes of the 5-storey simulation model.....	19
Figure 2.6: Fourier spectra of five floor responses of 5-DOF model (a) before and (b) after damage.....	20
Figure 2.7: Fourier spectra of the modal responses of 5-DOF system obtained using SOBI.	21
Figure 2.8: Hilbert spectra of all MMRs of 5-DOF system.....	23
Figure 2.9: TVAR modeling of the first MMR of 5-DOF system.....	25
Figure 2.10: TVAR modeling of all MMRs of 5-DOF system.....	25
Figure 2.11: Separated sources $s_{ud}(t)$ of undamaged states of 5-DOF system.....	27
Figure 2.12: Separated sources $s_d(t)$ of damaged states of 5-DOF model .....	28
Figure 3.1: (a) Actual model and (b) FE model of the 3-DOF experimental setup.....	30
Figure 3.2: Initiation of damage by adding (a) mass and (b) stiffness .....	31
Figure 3.3: Fourier spectra of (a) the observed signals and (b) MMRs of $C_1$ .....	32
Figure 3.4: HT applied to all MMRs of $C_1$ .....	33
Figure 3.5: TVAR modeling of the first MMR of $C_1$ .....	34
Figure 3.6: TVAR modeling of all MMRs of $C_1$ .....	34
Figure 3.7: Separated sources (a) $s_{ud}(t)$ and (b) $s_d(t)$ of $C_1$ .....	35
Figure 3.8: Fourier spectra of (a) the observed signals and (b) MMRs of $C_2$ .....	38
Figure 3.9: HT applied to all MMRs of $C_2$ .....	38
Figure 3.10: TVAR modeling of the first MMR of $C_2$ .....	39
Figure 3.11: TVAR modeling of all MMRs of $C_2$ .....	39
Figure 3.12: Separated sources (a) $s_{ud}(t)$ and (b) $s_d(t)$ of $C_2$ .....	40

Figure 3.13: Layout of the UCLA Factor building and the sensor locations.....	42
Figure 3.14: Vibration measurement of the UCLA Factor building under Parkfield earthquake.....	43
Figure 3.15: Fourier spectra of the top floor response of the UCLA Factor building .....	43
Figure 3.16: TVAR modeling of the first MMR of the UCLA Factor building.....	44
Figure 4.1: Schematic of axially-moving cantilever beam.....	47
Figure 4.2: Axial motion profile of beam extension and beam retraction scenarios .....	52
Figure 4.3: Beam extension: (a) responses and (b) their corresponding FFT spectra .....	53
Figure 4.4: Beam extension: (a) vibratory mode responses obtained from SOBI and (b) their respective FFT spectra.....	54
Figure 4.5: Beam extension: Comparison of the frozen IFs and IFs estimated by the TVAR method .....	55
Figure 4.6: Beam retraction: (a) responses and (b) corresponding FFT spectra.....	57
Figure 4.7: Beam retraction: (a) vibratory mode responses and (b) corresponding FFT spectra .....	58
Figure 4.8: Beam retraction: comparison of the frozen IFs and IFs estimated by the TVAR method .....	59
Figure 4.9: Experimental apparatus .....	60
Figure 4.10: Beam extension: The Wavelet transform of all three vibration signals .....	68
Figure 4.11: Beam retraction: The Wavelet transform of all three vibration signals .....	69
Figure 4.12: Beam extension: (a) Contour plot of $ W(a,b) $ of TAC vibration signal (a) and (b) estimated IF from ridges of WT (dash-dot line) and frozen IF (solid).....	70
Figure 4.13: Beam retraction: (a) Contour plot of $ W(a,b) $ of TAC vibration signal (a) and (b) estimated IF from ridges of WT (dash-dot line) and frozen IF (solid).....	71
Figure 4.14: Block diagram of the HVD algorithm (Feldman, 2011) .....	76
Figure 4.15: Beam extension: BSG vibration signal with the corresponding decomposed components obtained from the HVD method. The identified IFs (dash-dot) are compared with the frozen IFs (solid).....	80

Figure 4.16: Beam extension: TAC vibration signal with the corresponding decomposed components obtained from the HVD method. The identified IFs (dash-dot) are compared with the frozen IFs (solid).....	81
Figure 4.17: Beam retraction: BSG vibration signal with the corresponding decomposed components obtained from the HVD method. The identified IFs (dash-dot) are compared with the frozen IFs (solid).....	85
Figure 4.18: Beam retraction: TAC vibration signal with the corresponding decomposed components obtained from the HVD method. The identified IFs (dash-dot) are compared with the frozen IFs (solid).....	86
Figure 4.19: Beam extension: Comparisons between the IF obtained from the HVD method, the IF obtained the HVD plus TVAR method with the corresponding frozen IF.	89
Figure 4.20: Beam retraction: Comparisons between the IF obtained from the HVD method, the IF obtained the HVD plus TVAR method with the corresponding frozen IF.	90

## List of Tables

Table 2.1: Identified frequencies of undamaged and damaged states of 5-DOF model.....	26
Table 3.1: Identified $\omega$ and $\xi$ of $s_{ud}(t)$ and $s_d(t)$ of the 3-DOF model under $C_1$ .....	36
Table 3.2: Identified $\omega$ and $\xi$ of $s_{ud}(t)$ and $s_d(t)$ of the 3-DOF model under $C_2$ .....	37
Table 3.3: Identification results of the proposed method from UCLA Factor building .....	45
Table 4.1: Comparison between the IFs based on equation (4.3.1) and IFs based on equation (4.4.1).....	67

## List of Abbreviations

---

Abbreviation	Meaning
LTI	Linear Time Invariant
LTV	Linear Time Varying
BSS	Blind Source Separation
SHM	Structure Health Monitoring
SOBI	Second Order Blind Identification
TVAR	Time Varying Auto-Regression
HT	Hilbert Transform
HHT	Hilbert Haung Transform
HVD	Hilbert Vibration Decomposition
WT	Wavelet Transform
FFT	Fast Fourier Transform
SVD	Singular Value Decomposition
EVD	Eigen Value Decomposition
ICA	Independent Component Analysis
PCA	Principal Component Analysis
DOF	Degree-of-freedom
BSG	Base Strain Gauge
MAC	Middle accelerometer
TAC	Tip Accelerometer
IF	Instantaneous Frequency
UCLA	University of California Los Angeles
SSI	Stochastic Subspace Identification
ODE	Ordinary Differential Equation
PDE	Partial Differential Equation
MMR	Mixed Modal Response

---

# Chapter 1

## Introduction

### 1.1 Overview

Vibration analysis is the key to understand the underlying characteristics (e.g., modal parameters) of structural and mechanical systems. The changes in the modal parameters of structures under operational or critical events are inevitable and can be considered as damage in the system. Failures of large-scale civil infrastructure have significant societal and human consequence. Sudden or continuous degradation of these structures is inevitable due to varying environmental conditions, man-made excitations or natural hazards. Early detection of damage under operational or in-service condition is of paramount importance to avoid further risks in life safety and economic losses. In the case of mechanical systems, operational changes could also occur for some applications e.g., rotating machines, continuous change in robotic arms through prismatic joints, thread lines in textile industries, active suspension control in automotive industries and tethered satellite in space exploration. Structures or machines whose parameters change can be considered to be time-varying systems. Recently structural health monitoring (SHM) has garnered tremendous attention towards investigation and rehabilitation of such time-varying systems. Research in SHM has focused on developing sophisticated damage detection methods under a wide range of challenging situations (Doebeling et al., 1996; Carden and Fanning 2004; Yan et al., 2007; Megalhaes et al., 2012; Kuwabara et al., 2012; Chao et al., 2014). This study is motivated to develop a damage detection method which is tailored to SHM using the framework of blind source separation (BSS) (Kerschen et al., 2007; Sadhu, 2013). The BSS has emerged as new and powerful signal processing method for modal identification and in this thesis, it is explored as a possible candidate for robust damage detection algorithm.

## **1.2 Literature Review on Time-varying System Identification**

Over last few decades, numerous vibration-based damage detection algorithms have been proposed in the literature (Doebbling et al., 1996; Carden and Fanning, 2004). These researches can be primarily classified into two parts; parametric methods and non-parametric methods. Details of both the methods are presented in the following subsections.

### **1.2.1 The Parametric Damage Detection Methods**

The parametric damage detection methods estimate the physical parameters (e.g. stiffness or masses) of the structure. In Feng et al. (2015), frequency response functions of measured structural responses are used to estimate the physical parameters of the structure through which damage is detected. Time-series models are also well-known techniques for feature extraction from which the change in stiffness is predicted. Many researchers (Bodeux and Golinval 2001; Nair et al., 2006; Noh et al., 2009; Hsu et al., 2011; Yao and Pakzad 2012) use the auto-regressive (AR) model to approximate the vibration signal then the parameters or features of AR model are utilized to identify damage in the structure. Furthermore, other methodologies (Kuwabara et al., 2012; Bao et al., 2013) use the statistical information of structural responses to estimate the physical parameters and detect any variation. Garcia and Trendafilova, (2014), use principal component analysis that is based on cross-correlation matrices to identify the inherent parameters of laminar composite beam. Another recent method that gains popularity in structural damage detection is the genetic algorithm (GA). The GA is considered to be the most powerful search algorithm according to Chen and Nagarajaiah, (2011). Consequently, the estimated parameters are then successively compared with those from the Finite element (FE) model (Bao et al., 2013; Behmanesh and Moaveni, 2014). Nevertheless, the need for an accurate FE model and the associated computational cost and modeling error in the parametric methods limit their applications towards damage detection algorithms.

### **1.2.2 The Non-parametric Damage Detection Methods**

The non-parametric methods overcome the aforementioned limitations by utilizing advanced signal processing techniques over the vibration measurements to monitor the condition of a structure. In contrast to the parametric damage detection methods, the non-parametric methods assume no models about the structural behaviors. This category of methods exploits classical time-frequency analysis including wavelet transform (WT) (Yun et al., 2011; Su et al., 2014; Dziedziech et al., 2015), empirical mode decomposition (EMD) and Hilbert Huang transform (HHT) (Xu and Chen, 2004; Yang et al., 2004; Lin et al., 2005; Kunwar et al., 2013), synchro-squeezed transform (Amezquita-Sanchez and Adeli, 2014), Hilbert vibration decomposition (HVD) (Feldman, 2006; 2011), to identify damage by tracking the global information such as time-varying modal parameters (i.e., frequency, damping and mode shape). Recently, a newer class of signal processing method called Blind Source Separation (BSS) has garnered a significant attention in the field of ambient modal identification (Antoni, 2005; Poncelet, 2007; Yang and Nagarajaiah, 2011; Hazra et al., 2012; Sadhu et al., 2013; Sadhu et al., 2014; Ghahari et al., 2013; Yang and Nagarajaiah, 2014). In this thesis, BSS has been expanded further to develop a damage detection method.

### **1.3 Blind Source Separation (BSS)**

BSS has been extensively used as a powerful signal decomposition tool in the field of acoustic and image processing (Antoni, 2005). Using BSS, a multi-component signal is primarily decomposed into its inherent signals (called sources) by utilizing its second-order statistics such as auto-correlation functions (Belouchrani et al., 1996) or higher-order statistics such as non-Gaussianity (Antoni, 2005). In the previous studies, independent component analysis (ICA), a variant of higher-order BSS, is employed towards structural damage detection (Zang et al., 2004; Yang and Nagarajaiah, 2011; Chen et al., 2015). However, ICA is underscored due to its poor performance associated with higher damping and measurement noise. Principal component analysis (PCA) is further explored as fault

detection methods with the aid of wavelet transform (Kesavan and Kiremidjian, 2011, Tibaduiza et al., 2015). Successively, using auto-correlation functions, second-order blind identification (SOBI) is undertaken to conduct damage detection (Sadhu and Hazra, 2013; Spiridonakos et al., 2014). In Sadhu and Hazra, (2013), the SOBI method is adopted in multiple windows of incoming data to discriminate the effect of damage. However the SOBI operation in multiple windows of vibration data becomes computationally expensive and insensitive to the lower level of damage. In this thesis, the performance of the SOBI has been improved with the aid of time-varying auto-regressive (TVAR) modeling.

The SOBI method (Belouchrani et al., 1997) is based on the second-order statistics (i.e., auto-correlation) and works under the assumption that modal responses are stationary and uncorrelated with different spectra. However, when an abrupt change occurs in the structure, the vibration response signals would contain the modal information of undamaged and damaged states of the structure. Therefore, the modal response becomes non-stationary containing mixed-modal responses (MMR). In order to capture the behavior of MMR and identify the time-variant modal parameters, time-varying auto-regressive (TVAR) modeling is utilized. This novel approach enhances the use of the SOBI method for damage detection and can be tailored to the SHM application. The proposed algorithm is explored in identifying both discrete and progressive damage based on the output-only measurements. Several experimental and full-scale structures are used to validate the proposed method.

## **1.4 Objectives**

The main objectives of this thesis are summarized as follow:

- The first objective of the thesis is to develop a new method for damage detection of linear time-varying (LTV) systems.
- The second objective of the thesis is to demonstrate the proposed method through numerical simulations, lab-scale and full-scale structures.

- The third objective of the thesis is to identify the instantaneous frequencies (IF) of an axially moving cantilever beam using the proposed algorithm. The validity of the proposed algorithm will be investigated by numerical simulation.
- The fourth objective of the thesis is to employ the Wavelet transform (WT) and the Hilbert vibration decomposition (HVD) method to identify the IF of the axially moving cantilever beam.
- The fifth objective of the thesis is to identify IF of the axially moving cantilever beam by utilizing the HVD plus TVAR method.

## **1.5 Thesis Outline**

The following chapters of the thesis are organized as follows:

Chapter 2 presents the theoretical development of the proposed algorithm. The effectiveness of the proposed algorithm is validated in the case of an abrupt change in the characteristics of the structure with the aid of a numerical example.

Chapter 3 presents the validation of the proposed algorithm using the experimental studies of a lab-scale structure and a full-scale structure respectively. Both of the studies contain an abrupt change in their modal information. The results obtained from both of the studies are compared the parameters obtained using the Finite Element (FE) method and the Stochastic Subspace Identification (SSI) method respectively.

Chapter 4 addresses identification of instantaneous frequencies of an axially-moving cantilever beam. First the performance of the proposed algorithm is tested using computer simulation. Then the three different methods, namely, the WT, the HVD, and the HVD plus TVAR modeling, are employed using the experimental responses.

Chapter 5 presents the summary and main conclusions of the research. Recommendations for future study are also suggested.

## Chapter 2

### Damage Detection Based on Blind Source Separation

In this chapter, a novel approach is undertaken to identify and assess the severity of damage in deteriorating structures under natural excitations (e.g. wind or earthquake). The proposed algorithm is based on the framework of Second-Order Blind Identification (SOBI) (Belouchrani et al., 1997). In addition, two different post-processing steps are adopted to find damage instant in the structure. The extraction of modal responses is first undertaken using the SOBI in both of the proposed algorithms. In one method the Hilbert transform (HT) is utilized to identify the damage instant and in the other method the time-varying auto-regression (TVAR) modeling is employed to find damage instant. The two methods improve the implementation of the SOBI method for the classification and identification of linear time-varying (LTV) systems.

The chapter is organized as follows: Section 2.1 presents the proposed algorithm, Section 2.2 validates the proposed algorithm using a 5-DOF model, and finally Section 2.3 is comprised of summary and conclusions.

#### 2.1 Proposed Algorithm

##### 2.1.1 Second-Order Blind Identification (SOBI)

The basic dynamics of a structure can be considered a linear, classically damped, and lumped-parameter  $n_s$  degrees-of-freedom system, subjected to an excitation force  $F(t)$ .

$$[M]\{\ddot{x}(t)\} + [C]\{\dot{x}(t)\} + [K]\{x(t)\} = \{F(t)\} \quad (2.1.1)$$

where,  $x(t)$  is a vector of displacement coordinates,  $M$ ,  $C$  and  $K$  are the mass, damping and stiffness matrices of the system respectively,  $F(t)$  is the input excitation to the system that is assumed to be Gaussian and broadband. The solution to equation (2.1.1) can be written in terms of superposition of vibration modes with the following matrix form:

$$\{x(n)\} = [A]\{s(n)\} \quad (2.1.2)$$

where,  $x \in n_m \times N$  is the measurement matrix composed of the sampled components of  $x$ ,  $s \in n_s \times N$  is a matrix of the corresponding modal coordinates,  $A_{n_m \times n_s}$  is the modal transformation matrix, and  $N$  is the number of data points of the measurements. The columns of  $A$  matrix are linearly independent and they represent the mode shapes of structure. The main objective of SOBI (Belouchrani et al., 1997) is to formulate two covariance matrices  $[R_x(0)]$  and  $[R_x(p)]$  evaluated at the time lag zero and  $p$  from the observed measurements, then simultaneously diagonalize them in order to find unknown mixing matrix,  $A$ . In this way, the proposed damage detection method takes advantage of the SOBI method in separating the modal responses containing both damaged and undamaged states.

The essence of the SOBI method is as follows,

$$\begin{aligned} [R_x(0)] &= E[\{x(n)\}\{x(n)\}^T] = [A][R_s(0)][A]^T \\ [R_x(p)] &= E[\{x(n)\}\{x(n-p)\}^T] = [A][R_s(p)][A]^T \end{aligned} \quad (2.1.3)$$

where,

$$[R_s(p)] = E[\{s(n)\}\{s(n-p)\}^T] = [I] \quad (2.1.4)$$

There are three main steps of SOBI: whitening, orthogonalization and unitary transformation. The measured responses  $\{x(n)\}$  are zero-mean, and the whitening is obtained as follows. The singular value decomposition is used to diagonalize  $[R_x(0)]$ :

$$[R_x(0)] = E[\{x(n)\}\{x(n)\}^T] = [V_x][\lambda_x][V_x]^T \quad (2.1.5)$$

where  $[V_x]$  is the eigenvectors matrix and  $[\lambda_x]$  is the eigenvalue matrix. The whitened signals are then computed as shown in equation (2.1.6) and the matrix  $[Q]$  is realized as whitening matrix.

$$\begin{aligned}\{\bar{x}(n)\} &= [\lambda_x]^{-1/2} [V_x]^T \{x(n)\} \\ &= [Q] \{x(n)\}\end{aligned}\tag{2.1.6}$$

The reason for whitening is to remove the temporal correlation between the measured responses and it is shown in Figure 2.1.

$$[R_{\bar{x}}(0)] = E[\{\bar{x}(n)\}\{\bar{x}(n)\}^T] = [I]\tag{2.1.7}$$

Due to the whitening process  $[R_x(p)]$  becomes  $[R_{\bar{x}}(p)]$ , which is given by:

$$\begin{aligned}[R_{\bar{x}}(p)] &= \frac{1}{N} \left[ \sum_{n=1}^N \{\bar{x}(n)\}\{\bar{x}(n-p)\}^T \right] \\ &= [Q][R_x(p)][Q]^T \\ &= [Q][A][R_s(p)][A]^T [Q]^T\end{aligned}\tag{2.1.8}$$

Equation (2.1.8) states that whitened covariance matrix at a particular time-lag can be diagonalized; therefore the product  $[Q][A]$  is realized as unitary matrix and can be determined. This process of diagonalization is implemented numerically. During the orthogonalization process, the whitened covariance matrix  $[R_{\bar{x}}(p)]$  is diagonalized such that eigenvalue decomposition satisfies,

$$[V_{\bar{x}}][R_{\bar{x}}(p)][V_{\bar{x}}]^T = [\lambda_{\bar{x}}]\tag{2.1.9}$$

According to (Belouchrani et al., 1997), the diagonal matrix  $[\lambda_{\bar{x}}]$  should always be the same matrix regardless of the lag value  $p$  in  $[R_{\bar{x}}(p)]$  and also eigenvalues be distinct, thus the mixing matrix can be estimated by the following equation,

$$[\hat{A}] = [Q]^{-1}[V_{\bar{x}}] = [V_x][\lambda_x]^T[V_{\bar{x}}] \quad (2.1.10)$$

In order to find the unitary matrix  $[Q][A]$  that diagonalizes the whitened covariance matrix  $[R_{\bar{x}}(p)]$  at one or several non-zero time lags, SOBI undertakes an approximate joint diagonalization approach based on Givens rotation technique (Belouchrani et al., 1997). Consequently, the associated problem becomes to find minimum performance index  $\mathfrak{S}$ , such that unitary diagonalization satisfies  $[D] = [V]^T[R_{\bar{x}}(p)][V]$  (Belouchrani et al., 1997),

$$\mathfrak{S}(V, p) = \sum_p \sum_{1 \leq i \neq j \leq n_s} \|D_{ij}^p\|^2 \quad (2.1.11)$$

where,  $[V]$  is the unitary matrix and also the joint approximate diagonalizer for all  $p$ -shifted covariance (Belouchrani et al., 1997). Therefore, the estimated sources can be obtained once the estimated mixing matrix is calculated,

$$\{\hat{s}(n)\} = [\hat{A}]^{-1}\{x(n)\} \quad (2.1.12)$$

And now the estimated sources are spatially uncorrelated as defined by the equation below, and the illustration is shown in Figure 2.2.

$$[R_{\hat{s}}(0)] = E[\{\hat{s}(n)\}\{\hat{s}(n)\}^T] = [I] \quad (2.1.13)$$

Since the vibration data contains a discrete damage event, each modal response contains sources with both undamaged and damaged states (i.e. mixed modal responses (MMR)). In order to separate them, the Hilbert Transform (Feldman, 2006) seems to be an ideal choice because of its time-varying nature.

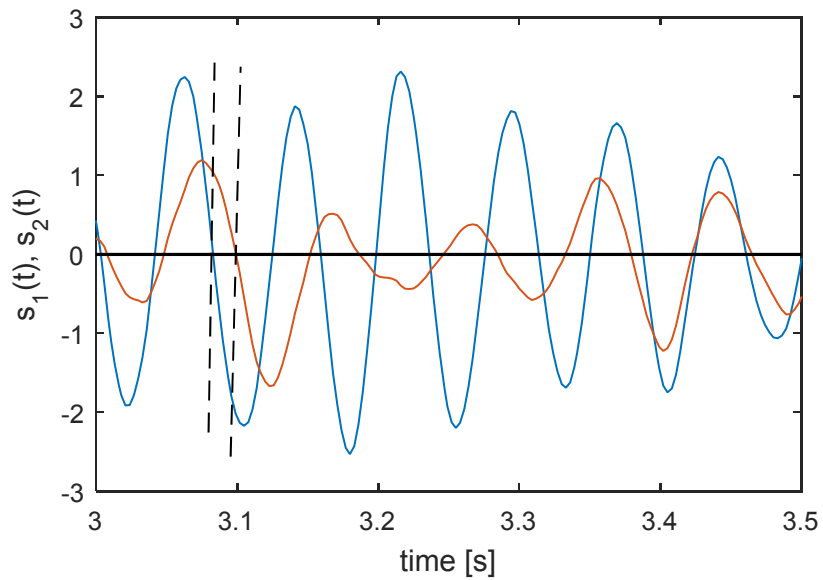


Figure 2.1: Sources  $s_1(t)$  (blue) and  $s_2(t)$  (red) obtained from the SOBI are temporally uncorrelated

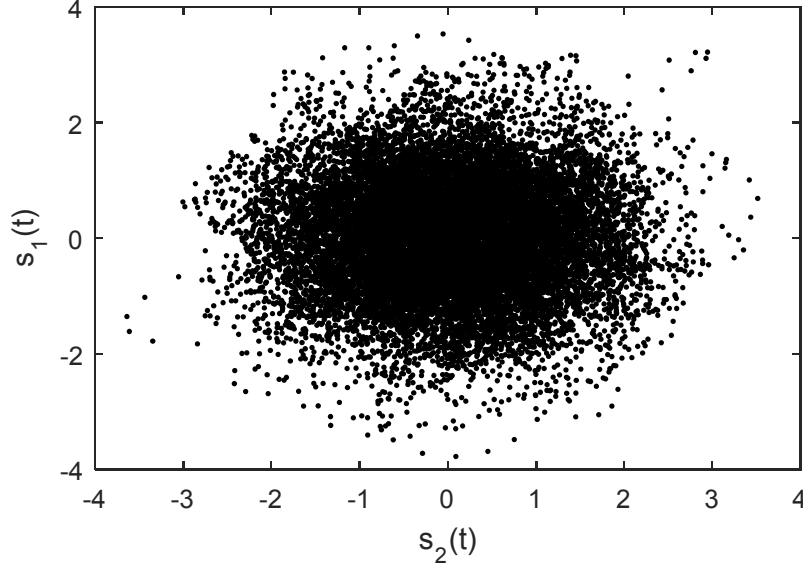


Figure 2.2: Sources  $s_1(t)$  and  $s_2(t)$  obtained from the SOBI are spatially uncorrelated

### 2.1.2 The Hilbert Transform

After the sources are obtained from the SOBI algorithm, it can be shown that there still exists some mode-mixing in each individual source and an acronym used throughout the thesis to represent this phenomenon; mixed-modal-response (MMR), which corresponds to undamaged and damaged states of the structure. Thus, there is a need to separate the undamaged modal source  $s_{ud}(t)$  and damaged modal source  $s_d(t)$  in order to obtain the accurate mixing matrices  $A_{ud}$  and  $A_d$ . Therefore, Hilbert transform is employed to trace the change in frequencies of all the MMR. Once the time instant of the change is obtained, the separation of damaged and undamaged states can be obtained easily. The Hilbert transform (HT) of a signal can be obtained using the following equation:

$$H(s(t)) = s(t) * \frac{1}{\pi t} = \frac{1}{\pi} P \int_{-\infty}^{\infty} \frac{s(\tau)}{t - \tau} d\tau = y(t) \quad (2.1.14)$$

where,  $H$  represents the Hilbert function, which states that any real signal  $s(t)$  convolves with  $\frac{1}{\pi t}$  resulting in a quadrature signal of the real signal. Because of integral formulation the quadrature signal could be obtained by using Cauchy principal value. In other word, from equation (2.1.14), one could get the conjugate pair of the observed signal. Consequently, adding the initial signal with its counterpart quadrature signal, a complex signal is formed that only has the positive spectrum. The combined new signal is known as the analytic signal in the literature.

$$z(t) = s(t) + iy(t) = A(t)e^{j\theta(t)} \quad (2.1.15)$$

where,

$$A(t) = [s^2(t) + y^2(t)]^{1/2} \quad (2.1.16)$$

$$\theta(t) = \tan^{-1} \frac{y(t)}{s(t)} \quad (2.1.17)$$

To find the instantaneous phase information from equation (2.1.15), it is recognized that equation (2.1.17) is a piece-wise function. At a damage instant, this piece-wise function might increase or decrease in slope thus taking the time derivative of instantaneous phase resulting in instantaneous frequency (IF) as shown in equation (2.1.18).

$$\omega(t) = \frac{d\theta(t)}{dt} = \frac{1}{A^2(t)} \left[ s(t) \frac{dy(t)}{dt} - y(t) \frac{ds(t)}{dt} \right] \quad (2.1.18)$$

The primary idea of the current research is to use the SOBI method which is robust in delineating modal responses, but fails in the case of closely spaced modes. The modal responses obtained from the SOBI exhibit bi-spectral component (Ann et al., 2013) (i.e. MMR), meaning the presence of damage and undamaged states. As a result, the HT is an ideal method to detect the change in frequencies of MMRs.

There are two drawbacks with the HT (Feldman, 2006). First, the frequency resolution decreases when modulated amplitude  $A(t)$  becomes small, as shown in equation (2.1.18), especially in case of free vibration where the transient response  $A(t)$  converges to zero faster specifically in higher modes. The second drawback is the incomplete periodicity that is present at the beginning and end of a signal which affects the estimation of IF in equation (2.1.18). A simple sinusoidal function with a discrete change in frequency after some interval is considered to illustrate the two problems associated with the HT. The first drawback is illustrated in the first row of Figure 2.3. The second drawback is illustrated in second row of Figure 2.3. These drawbacks make the identification of damage instant difficult. Thus, a more sophisticated method to detect the damage instant is needed.

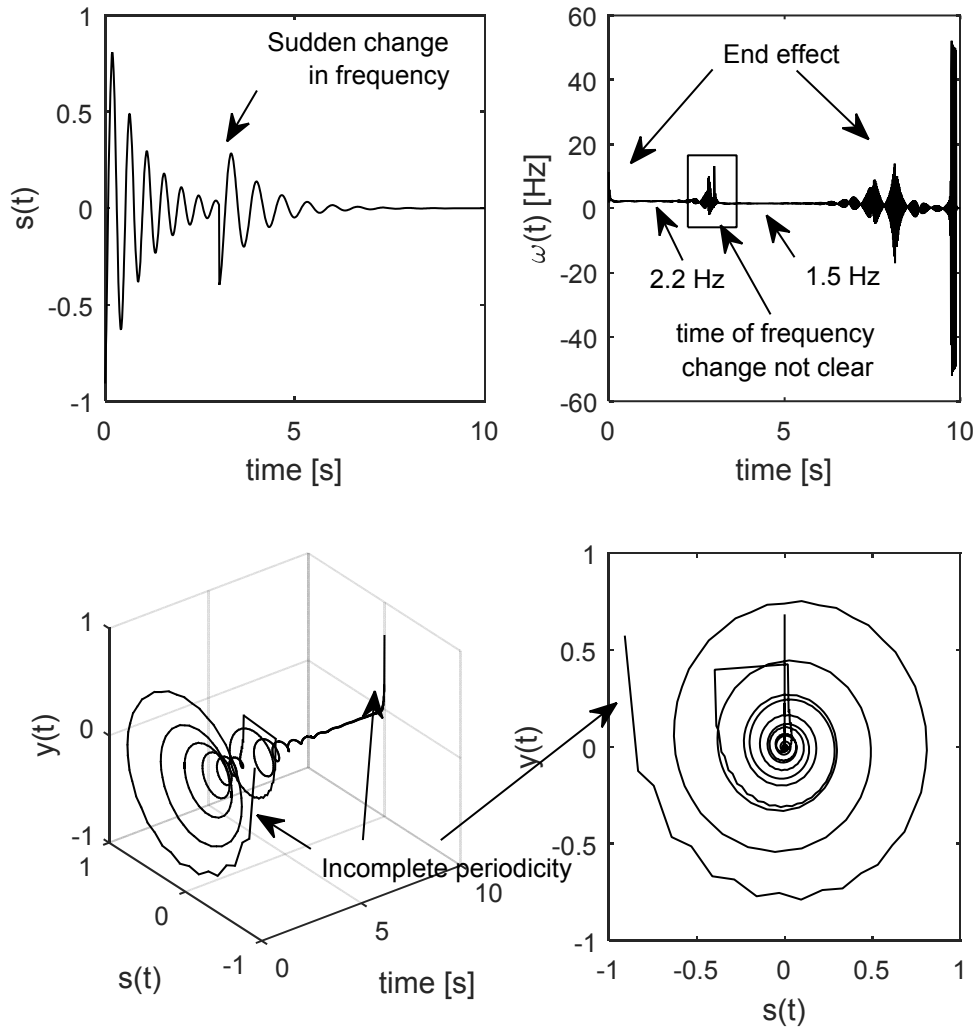


Figure 2.3: Drawbacks associated with the Hilbert transform

### 2.1.3 Time-varying Auto-Regressive (TVAR) Modeling

Once the modal responses are obtained from SOBI, the next step is to identify the damage instant. In order to characterize the behavior of MMR sources, the TVAR modeling (Nguyen, 2009) is adopted here instead of the HT. Such a model tracks the real-time changes of the model coefficients revealing the faults in the structures. Let,  $y(n)$  represents the MMR sources, and  $v(n)$  denotes the zero-mean Gaussian measurement noise with variance  $\sigma_v^2$ . Then the AR model of order  $p$  can be represented as:

$$y(n) = \sum_{k=1}^p a_k y(n-k) + v(n) \quad (2.1.19)$$

However, because of the non-stationary nature of the MMR sources, recursive modeling requires a time-varying approach in which  $a_k$  becomes  $a_k(t)$ . For this purpose, the Kalman filter is utilized to estimate these time-varying coefficients, from the vibration measurements (Nguyen, 2009). The following equation is the discrete representation of the  $a_k(t)$  coefficients and  $w(n)$  is the process noise with variance  $\sigma_w^2$  and covariance of  $P_w = I_{p \times p} \sigma_w^2$ . Both noise measurements  $v(n)$  and  $w(n)$  are mutually independent and uncorrelated.

$$x(n) = \Gamma(n-1)x(n-1) + w(n) \quad (2.1.20)$$

$$y(n) = C(n)x(n) + v(n) \quad (2.1.21)$$

where,  $x(n) = (a_1(n), a_2(n), \dots, a_p(n))^T$  is the unknown state vector. The matrix  $\Gamma(n-1) = I_{p \times p}$  is assumed to be an identity matrix.  $C(n) = (y(n-1), \dots, y(n-p))$  is the observation data with discrete  $n$ -step. The Kalman filter has mainly two processes: one is the

time update (prediction) and the other is measurement update (correction). At each step the Kalman filter equations can be written as (Bodeux and Golinval, 2001; Nguyen, 2009):

$$x(n | n - 1) = x(n - 1 | n - 1) \quad (2.1.22)$$

$$P_x(n | n - 1) = P_x(n - 1 | n - 1) + I\sigma_w^2 \quad (2.1.23)$$

$$y(n | n - 1) = C(n)x(n | n - 1) \quad (2.1.24)$$

$$\sigma_y^2(n | n - 1) = C(n)P_x(n | n - 1)C(n)^T + \sigma_v^2 \quad (2.1.25)$$

and

$$K(n) = P_x(n | n - 1)C(n)^T \sigma_y^2(n | n - 1)^{-1} \quad (2.1.26)$$

$$x(n | n) = x(n | n - 1) + K(n)[y(n) - y(n | n - 1)] \quad (2.1.27)$$

$$P_x(n | n) = [I - K(n)C(n)]P_x(n | n - 1) \quad (2.1.28)$$

where,  $x(n | n - 1)$  represents a *priori* estimate and its linear combination would result in  $x(n | n)$  which is a *posteriori*. The Kalman gain,  $K(n)$  gives a weightage to the prediction error  $y(n) - y(n | n - 1)$ , to minimize the state estimation error  $x(n | n)$  (Nguyen, 2009).

$P_x(n | n - 1)$  and  $P_x(n | n)$  are the *priori* and *posteriori* error covariance estimates.

The details of the proposed method is now illustrated using the flowchart as shown in Figure 2.4. Vibration response  $x_i(t)$  is first processed by the SOBI to obtain the MMR signals, then TVAR is utilized to extract the time-varying coefficients  $a_i(t)$  through which damage instant  $t_d$  is detected. Furthermore, all the MMR signals are then segmented using  $t_d$  into undamaged  $s_{ud}(t)$  and damaged  $s_d(t)$  modal responses respectively, and then modal parameters of damaged and undamaged states are estimated.

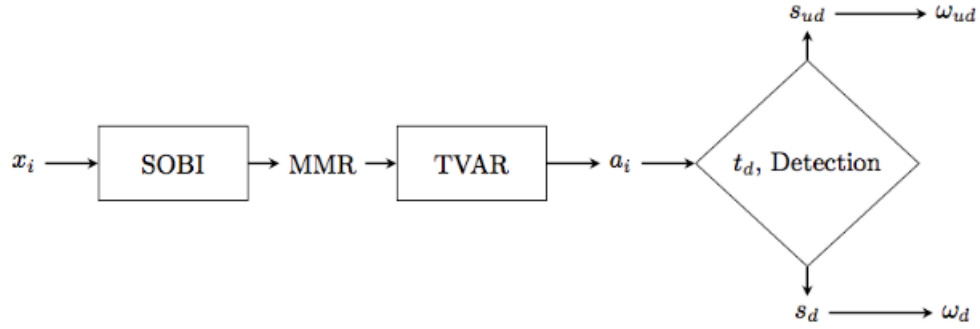


Figure 2.4: Flowchart of the proposed method

## 2.2 Damage-Based Studies: Identification of Damage Instant and Modal Parameters

In this section, the proposed damage detection algorithm is applied to a 5-storey shear-beam structural model (Sadhu, 2013). The governing equations of the system are represented in the following state-space model:

$$\begin{aligned} \{\dot{x}(t)\} &= [A]\{x(t)\} + [B]\{u(t)\} \\ \{y(t)\} &= [\tilde{C}]\{x(t)\} \end{aligned} \quad (2.2.1)$$

where  $\{x(t)\}$  is the state vector,  $[A]$  is referred to as the state matrix,  $\{u(t)\}$  represents the excitation, and  $[B]$  is the input influence matrix,  $[\tilde{C}]$  is the observation matrix and  $\{y(t)\}$  represents the system's output. In this example, the model is excited by Gaussian white noise at the base. The state matrix  $[A]$  is composed of  $-[M]$ ,  $[C]$  and  $[K]$  matrices as follows.

$$[A] = \begin{bmatrix} 0_{5 \times 5} & I_{5 \times 5} \\ -M^{-1}K & -M^{-1}C \end{bmatrix} \quad (2.2.2)$$

The mass of each floor is taken as 19.57 kg. The lateral stiffness of five columns is assumed to be 14.6, 52.7, 58.3, 58.6 and, 77.2 kN/m, respectively. The modal damping for

all the modes is assumed to be 2%. The resulting natural frequencies of the model are 0.91, 3.37, 7.1, 10.66 and 12.73 Hz respectively. The mode shapes of the undamaged (UD) structure (normalized with respect to first floor) are shown in Figure 2.5.

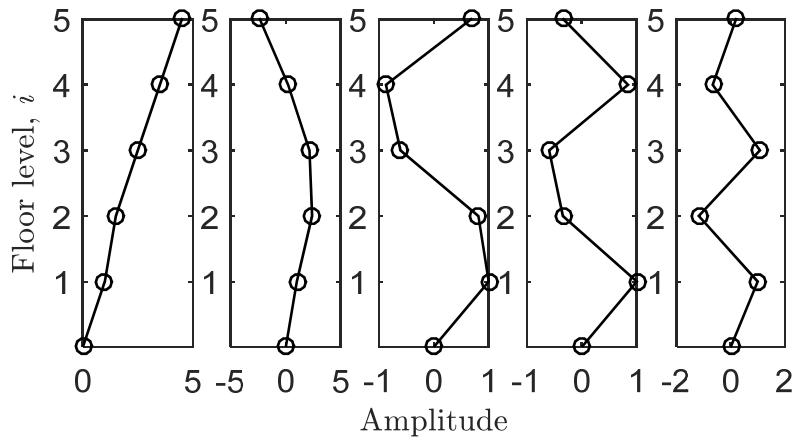


Figure 2.5: Mode shapes of the 5-storey simulation model

To demonstrate the proposed method, the stiffness of each column of the 5-DOF model is reduced by 35% at time instant  $t_d = 25$  seconds. The overall reduction in stiffness subsequently decreases the natural frequencies of each mode of the structure. Figure 2.6 (a) shows the Fourier spectra of the observed signal from each floor with measurements up to  $t_d = 25$  seconds that primarily contains the undamaged frequencies. The measurement from each floor shows approximately five peaks in frequency domain which corresponds to a linear combination of five individual modes. Figure 2.6 (b) shows the Fourier spectra of the measurements up to 50 seconds which contain the natural frequencies of both the damaged and undamaged structures. Subsequently, five pairs of frequencies (a total of 10 peaks – 5 peaks from undamaged states and 5 from damaged states) are observed in this data. This data is now utilized to conduct the damage detection using the proposed method.

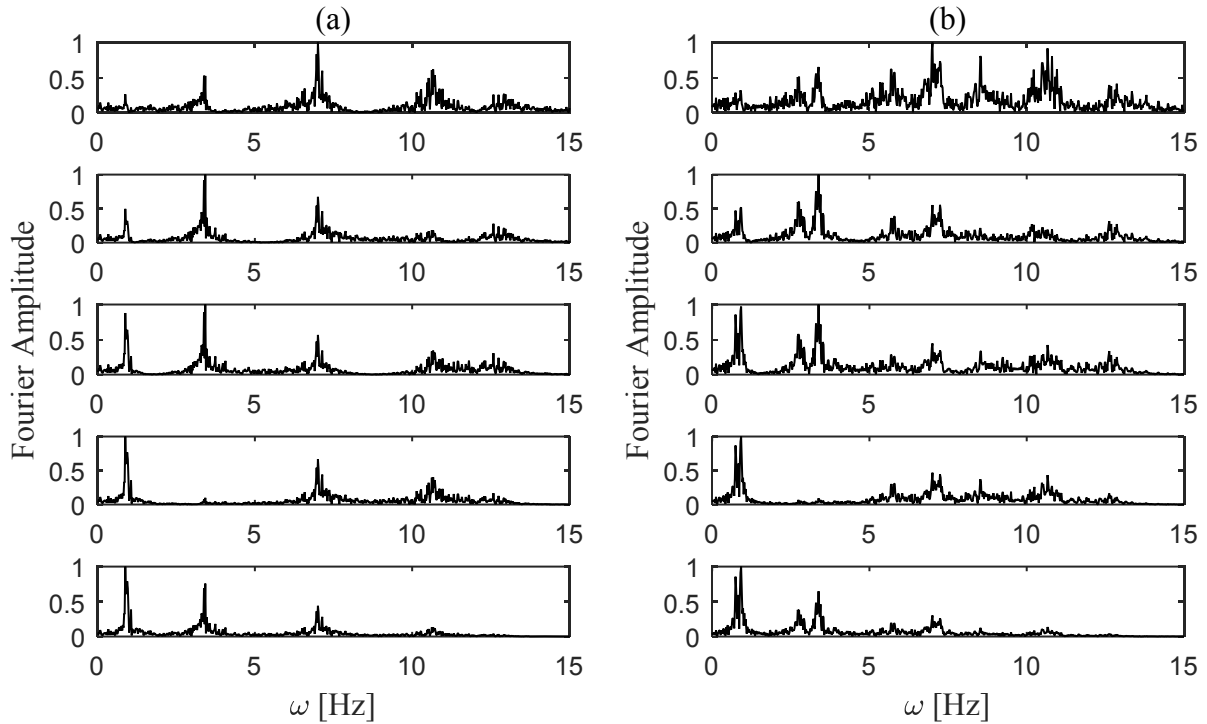


Figure 2.6: Fourier spectra of five floor responses of 5-DOF model (a) before and (b) after damage

The SOBI algorithm (Belouchrani et al., 1997) is first employed to extract the modal responses of the structure. The Fourier spectra of the resulting modal responses are shown in Figure 2.7. It may be noted that the data contains a total of 10 modes, whereas only five measurements are used in the SOBI method resulting an *underdetermined system identification* problem where the number of measurements is less than the number of target modes of interest. However, the SOBI algorithm works only for a fully-determined case or over-determined problem (Sadhu 2013). Therefore, it is expected that the SOBI method alone cannot separate individual undamaged and damaged frequencies (i.e. 10 frequencies), which is also reflected in Figure 2.7 where each modal response contains a pair of damaged and

undamaged frequencies of each mode (e.g., 0.71 and 0.91 Hz, and so on). The reduction in frequencies represents the damaged frequencies of the building which are 0.71, 2.68, 5.74, 8.64 and 10.2 Hz respectively. The estimated mixing matrix obtained from equation (2.1.10) contains the mixed information of the damaged and the undamaged modal responses and such contamination of both the states is referred in this study as mixed-modal-response (MMR). As the standard SOBI algorithm is unable to separate damaged and undamaged modal responses, the time-varying autoregressive (TVAR) modeling is utilized to address this limitation of SOBI. In what follows, it will be shown how HT and TVAR modeling of modal responses will be utilized to detect damage instant and the severity of damage.

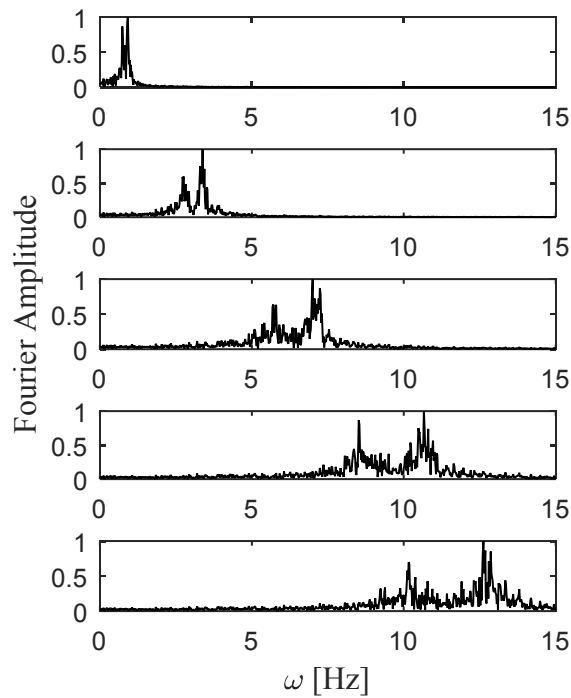


Figure 2.7: Fourier spectra of the modal responses of 5-DOF system obtained using SOBI

The key idea to separate the undamaged and damaged modal frequencies resulted from SOBI would be to track the damage instant. As soon as the damage instant is identified, the signal can be separated into two segments containing undamaged and damaged states. A popular technique to find instantaneous frequency for a non-stationary signal is Hilbert transforms (HT) (Yang et al., 2004). As an initial attempt, HT is first applied to individual modal responses. The results are shown in Figure 2.8. In this figure, the sudden reduction of frequencies can be seen in all MMRs (i.e. modal responses), however because of relatively small difference between  $\omega_{ud}$  and  $\omega_d$ , it is somewhat difficult to accurately identify the damage instant. Moreover, as mentioned in section 2.1.2 the end effects of HT (Yang et al., 2004; Xu and Chen, 2004) pullulates further complexities to this problem. Therefore, a more robust isolation of damage instant is required to solve this problem.

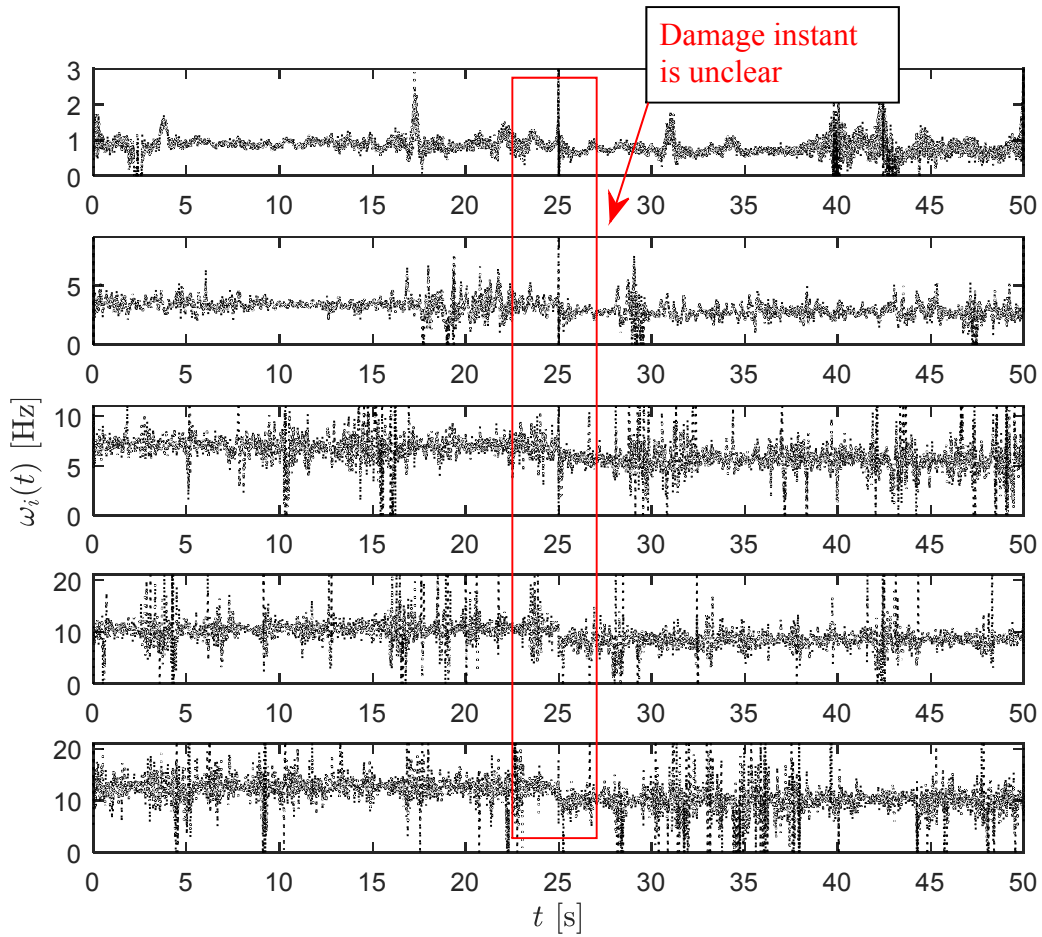


Figure 2.8: Hilbert spectra of all MMRs of 5-DOF system

In order to address the limitations of the HT, the TVAR method is utilized to detect damage instant. Since, the MMRs are mono-component in nature; a low model order would be sufficient (Sadhu, 2013). Figure 2.9 shows that by taking the first MMR and processing it through the TVAR method, the time-dependent coefficients of the TVAR reveal the accurate damage instant at  $t_d = 25$  seconds. Figure 2.10 shows the TVAR coefficients of all sources and it is clear that, except the TVAR coefficients for the fourth MMR, the damage instant can

be readily detected using the TVAR coefficients. In this study, only the first MMR is utilized to detect the damage instant. This confirms the suitability of the TVAR method for damage instant detection, and addresses the limitation of the SOBI in delineation of mode-mixing. It may be noted that the model order selection for a time series is a mathematically intensive exercise. However, since each of the modal responses resulting from the SOBI contains a single frequency; relatively low model order (say, 2) can be readily used instead. Such simple yet powerful decomposition and modeling tool makes the proposed method amenable towards online damage detection scheme for civil engineering structures.

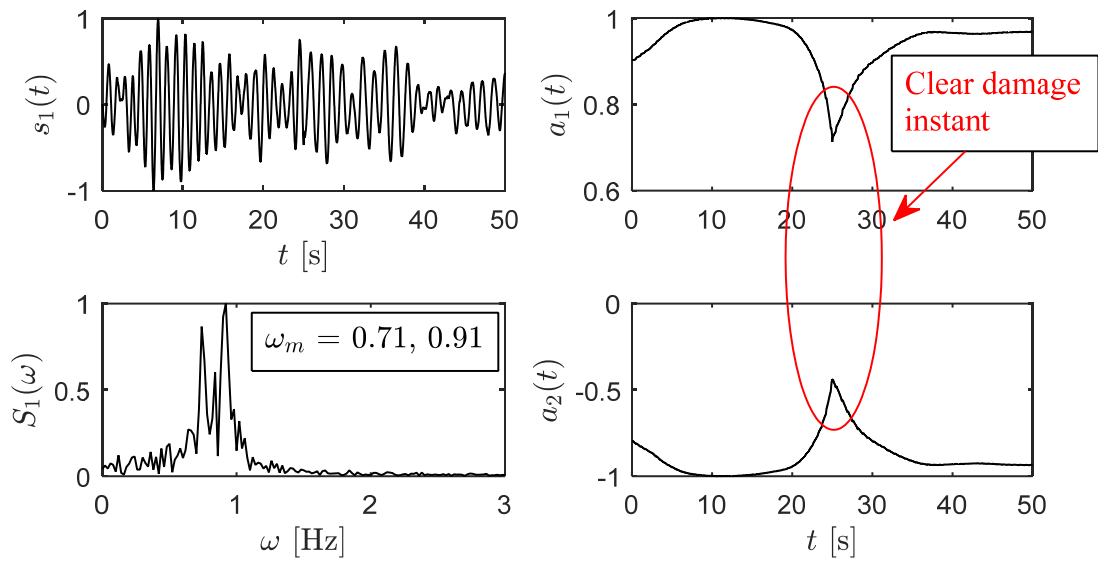


Figure 2.9: TVAR modeling of the first MMR of 5-DOF system

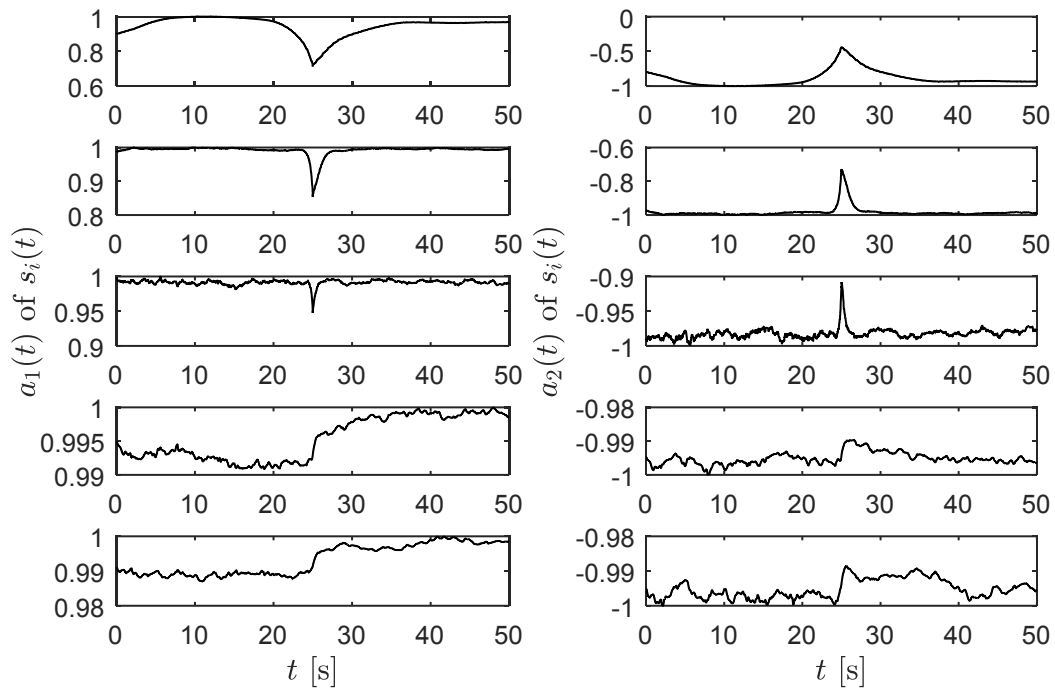


Figure 2.10: TVAR modeling of all MMRs of 5-DOF system

Table 2.1: Identified frequencies of undamaged and damaged states of 5-DOF model

Mode #	$\omega_{ud}$ [Hz]	$\omega_d$ [Hz]	Severity of damage [%]
1	0.91	0.71	21.9
2	3.37	2.68	20.5
3	7.11	5.74	19.3
4	10.66	8.64	18.9
5	12.73	10.2	19.8

As soon as the damage instant is identified, the modal responses are divided into undamaged and damaged segments. Considering that the mixing matrix from equation (2.1.10) is significantly erroneous due to the presence of mode mixing in the sources; the SOBI algorithm can be utilized again on the separated modal responses to obtain the correct estimation of  $\hat{A}_{ud}$  and  $\hat{A}_d$  mixing matrices (i.e., mode shapes) respectively. Figure 2.11 and Figure 2.12 show the separated sources of the 5-DOF model for the undamaged and damaged states. The detailed modal identification results are finally summarized in Table 2.1 which are well matching with their theoretical values. Moreover, the percentage difference in the frequencies represents the severity of damage.

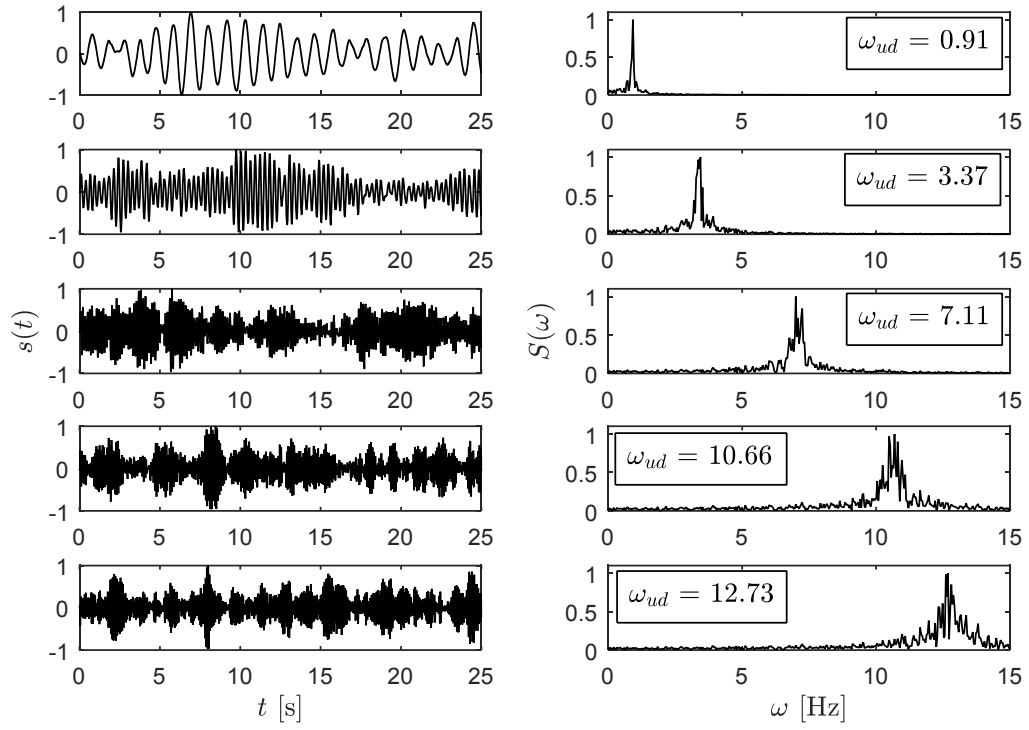


Figure 2.11: Separated sources  $s_{ud}(t)$  of undamaged states of 5-DOF system

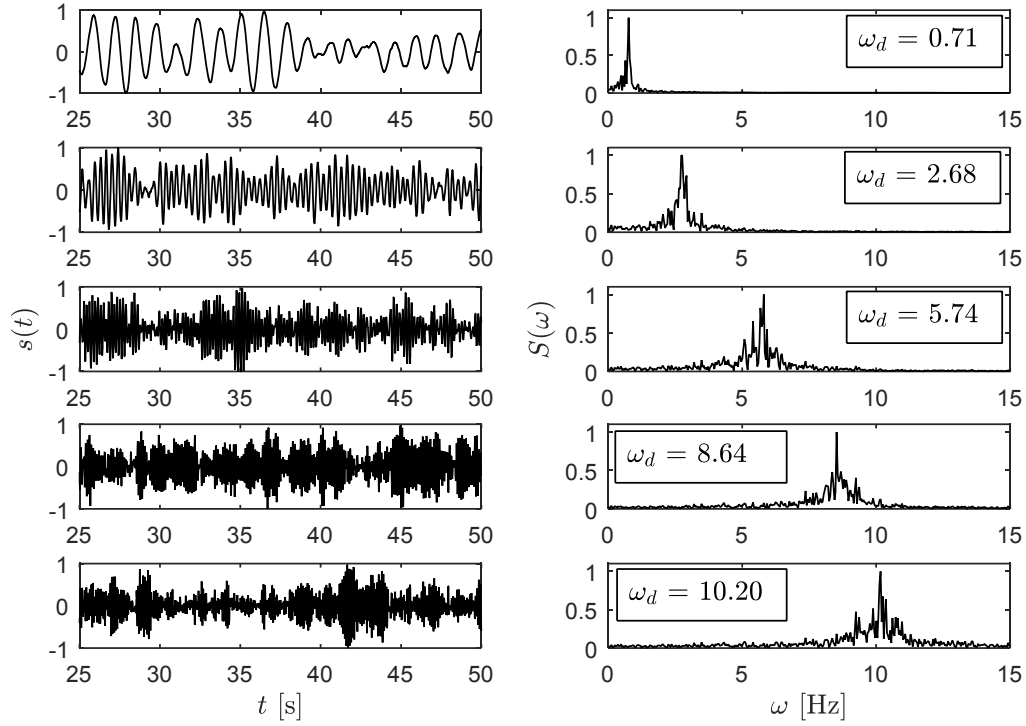


Figure 2.12: Separated sources  $s_d(t)$  of damaged states of 5-DOF model

### 2.3 Summary

In this chapter, a new damage instant detection method is presented which is tailored to the advanced structural health monitoring. The proposed method overcomes the limitation of SOBI in terms of separating the damaged and undamaged state information of the structure by employing TVAR algorithm. The HT method was initially attempted to identify the damage instant, however because of time-frequency resolution issue the damage instant was un-identifiable. In addition, the HT also affects the ends of a signal, which comes from incomplete periodicity (Feldman, 2006), therefore HT was not exploited further.

# Chapter 3

## Experimental Studies

This chapter demonstrates the validity of the proposed algorithm considering two lab-scale models and UCLA Factor building. The chapter is organized as follows: Section 3.1 presents the experimental setup, Section 3.2 presents two lab-scale models in terms of damage cases, Section 3.3 presents full-scale study of UCLA Factor building, and the summary and key conclusions are presented in Section 3.4.

### 3.1 Experimental Setup

An experimental model is constructed to validate the proposed damage detection method in a real-time setting. Figure 3.1 shows the experimental building model and its finite element (FE) model used for this study. Three accelerometers with a sensitivity of 1 V/g are attached to the individual floors of the structure, and a data acquisition system manufactured by Data Translation<sup>(R)</sup> is used to collect the vibration data subjected to an impulse hammer. The masses from top to first floor are 3.2, 1.1 and 0.656 kg, respectively. The two-side columns are made of aluminum with a mass of 0.718 kg and the dimensions are 776.5 mm (height) x 107.2 mm (width) x 3.08 mm (thickness) with 257.1 mm (height) between floors. The FE model of this structure is constructed using S-Frame<sup>®</sup> software. This model can be readily utilized to validate the accuracy of the proposed method in the subsequent sections

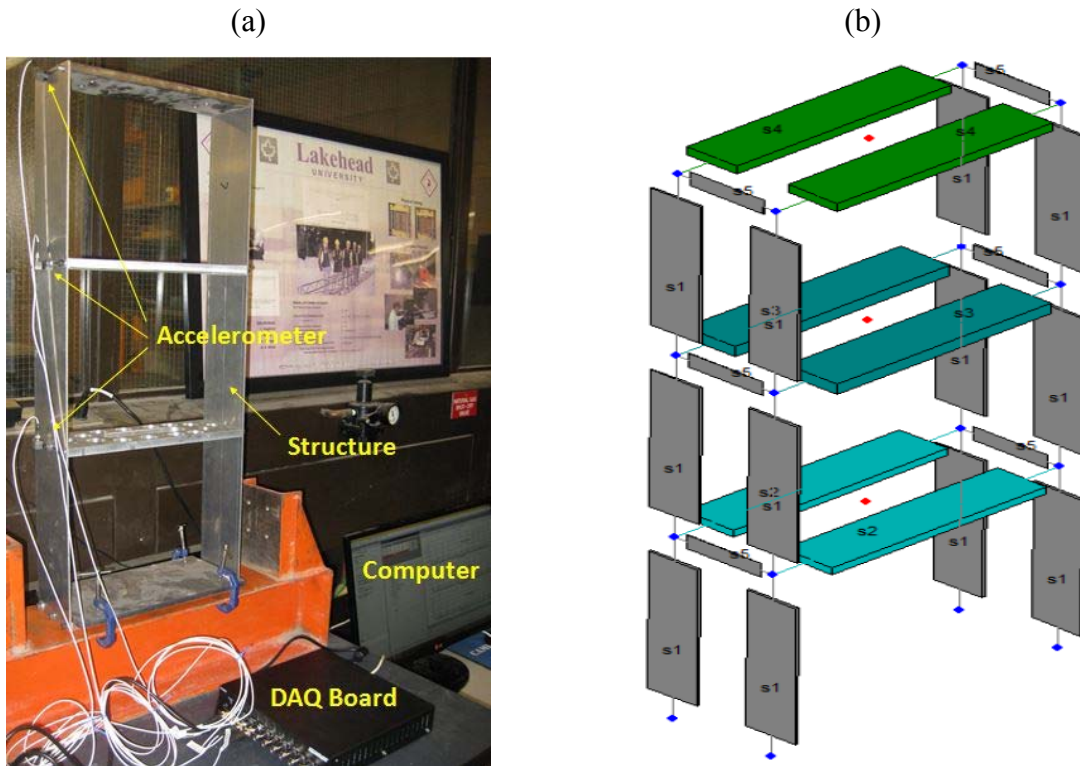


Figure 3.1: (a) Actual model and (b) FE model of the 3-DOF experimental setup

### 3.2 Damage Cases

Two realistic cases of damage are employed in this study; one with changes in mass and the other with changes in stiffness. Therefore, the 3-DOF model has two baseline systems (say,  $C_1$  and  $C_2$ ). In the first case ( $C_1$ ), an additional mass of 1.6 kg was added to the top floor during the vibration as shown in Figure 3.2 (a). In the second case ( $C_2$ ); a more realistic scenario is considered which is changing the stiffness of the structure. To do this, additional steel wire bracing connected to the 2<sup>nd</sup> floor from the red-colored base is used to stiffen the structure. During its vibration, the steel wires were cut suddenly and thereby, the overall stiffness of the structures is reduced. This case is analogous to a practical situation where the columns of a civil engineering structure get damaged due to earthquake or blast event. The

proposed output-only damage detection method is now applied to the vibration data collected using the accelerometers.

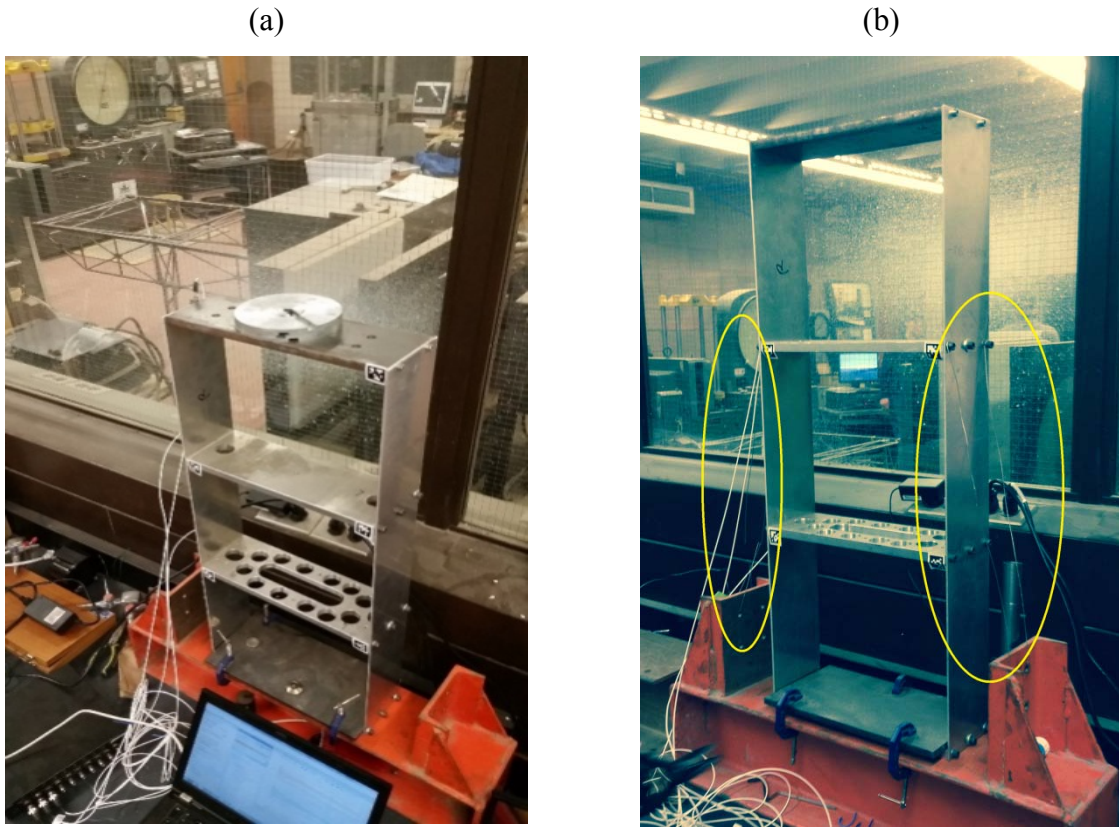


Figure 3.2: Initiation of damage by adding (a) mass and (b) stiffness

### 3.2.1 Damage Identification in $C_1$

Figure 3.3 shows the FFT spectra of the measured signals and their modal responses resulting from SOBI. There are three pairs of frequencies existing in the vibration data of each floor. Each pair of frequencies corresponds to individual modes of the undamaged and damaged states. The contribution of the higher modes in the 3<sup>rd</sup> floor response is significantly small; this is because the mass of the 3<sup>rd</sup> floor is low compared to the other two floors. First, the

SOBI is employed to delineate the modal sources as shown in Figure 3.3 (b). As expected, the MMRs can be observed in each resulting modal responses.

To observe the sudden reduction of frequencies in MMR, the HT is first utilized. Consequently, as shown in Figure 3.4, the neighborhood of the damage instant cannot be accurately identified using the HT. The damage induced in the structure is approximately between 2 to 4 seconds.

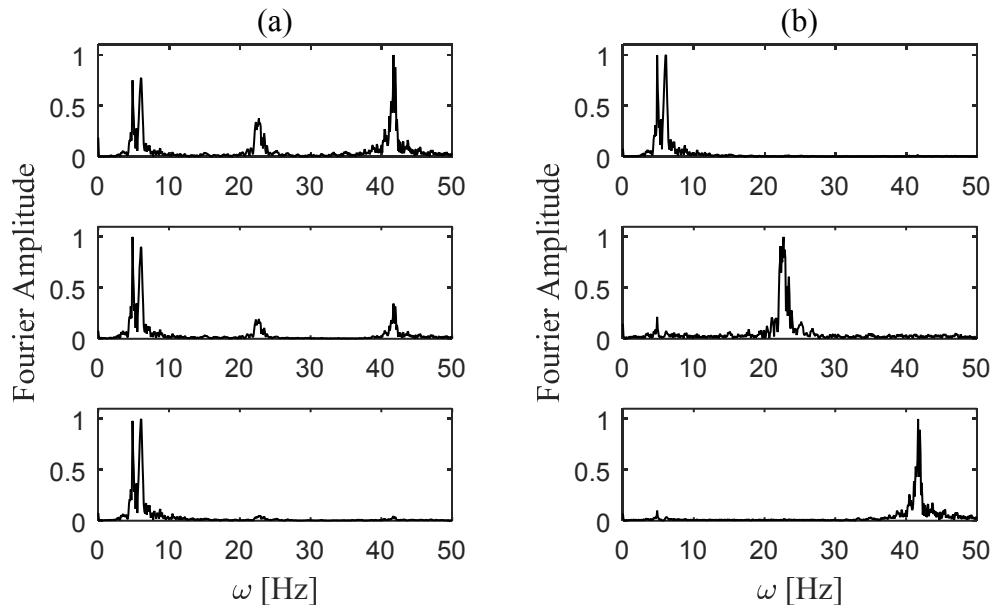


Figure 3.3: Fourier spectra of (a) the observed signals and (b) MMRs of  $C_1$

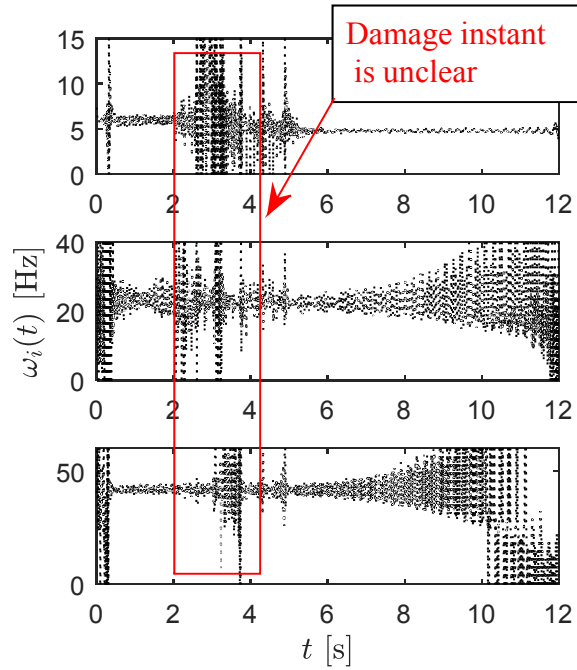


Figure 3.4: HT applied to all MMRs of  $C_1$

Now, the modal responses of SOBI are fed into TVAR and the time-varying coefficients of the TVAR algorithm detect the damage instant  $t_d$  accurately as shown in Figure 3.5 and Figure 3.6. The damage occurred in  $S_1$  at  $t_d = 3.2$  seconds due to increase in mass at the top floor level. It is observed that the damage instant could only be detected through dominant modes because the difference between the damaged and undamaged frequencies of third mode is significantly low. Therefore,  $a_1(t)$  and  $a_2(t)$  of  $s_3(t)$  in Figure 3.6 shows insignificant changes.

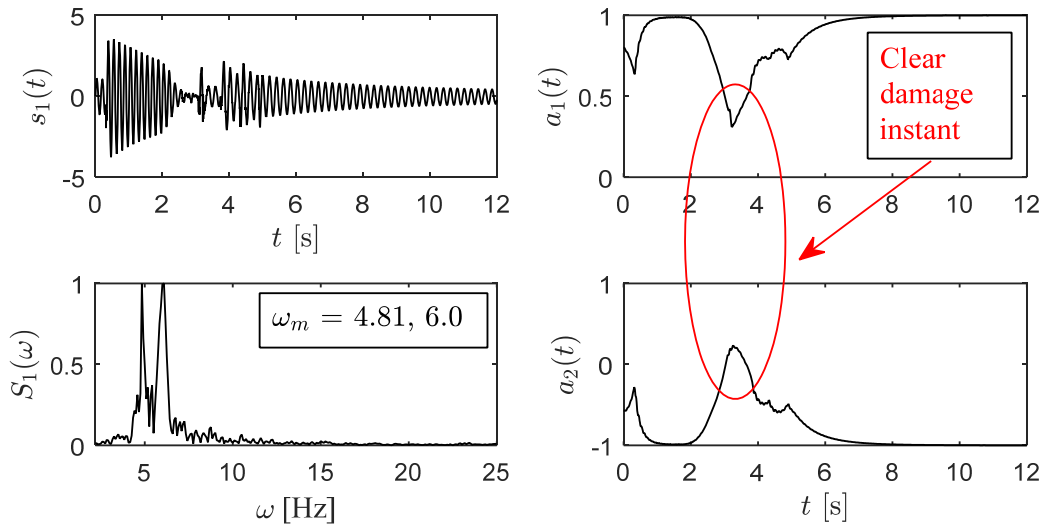


Figure 3.5: TVAR modeling of the first MMR of  $C_1$

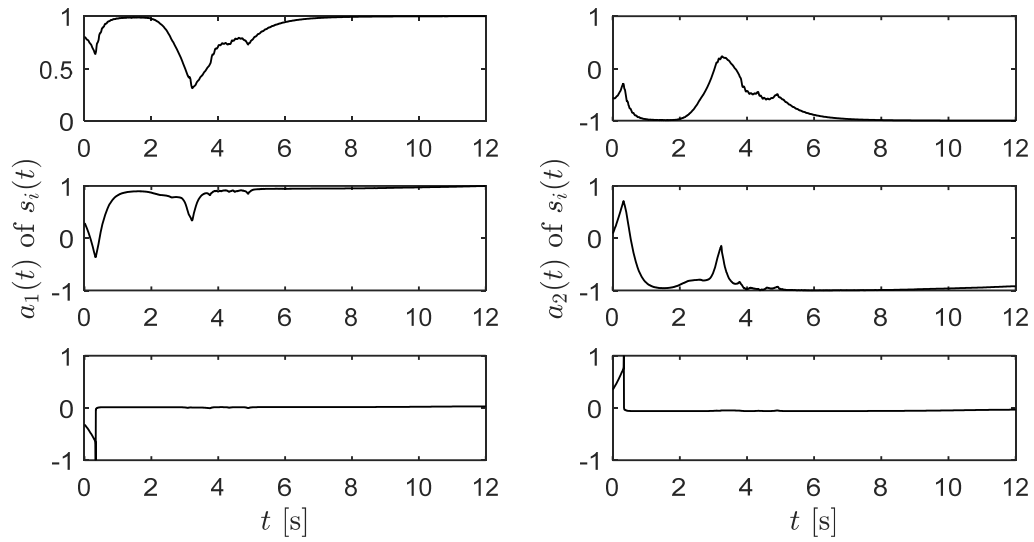


Figure 3.6: TVAR modeling of all MMRs of  $C_1$

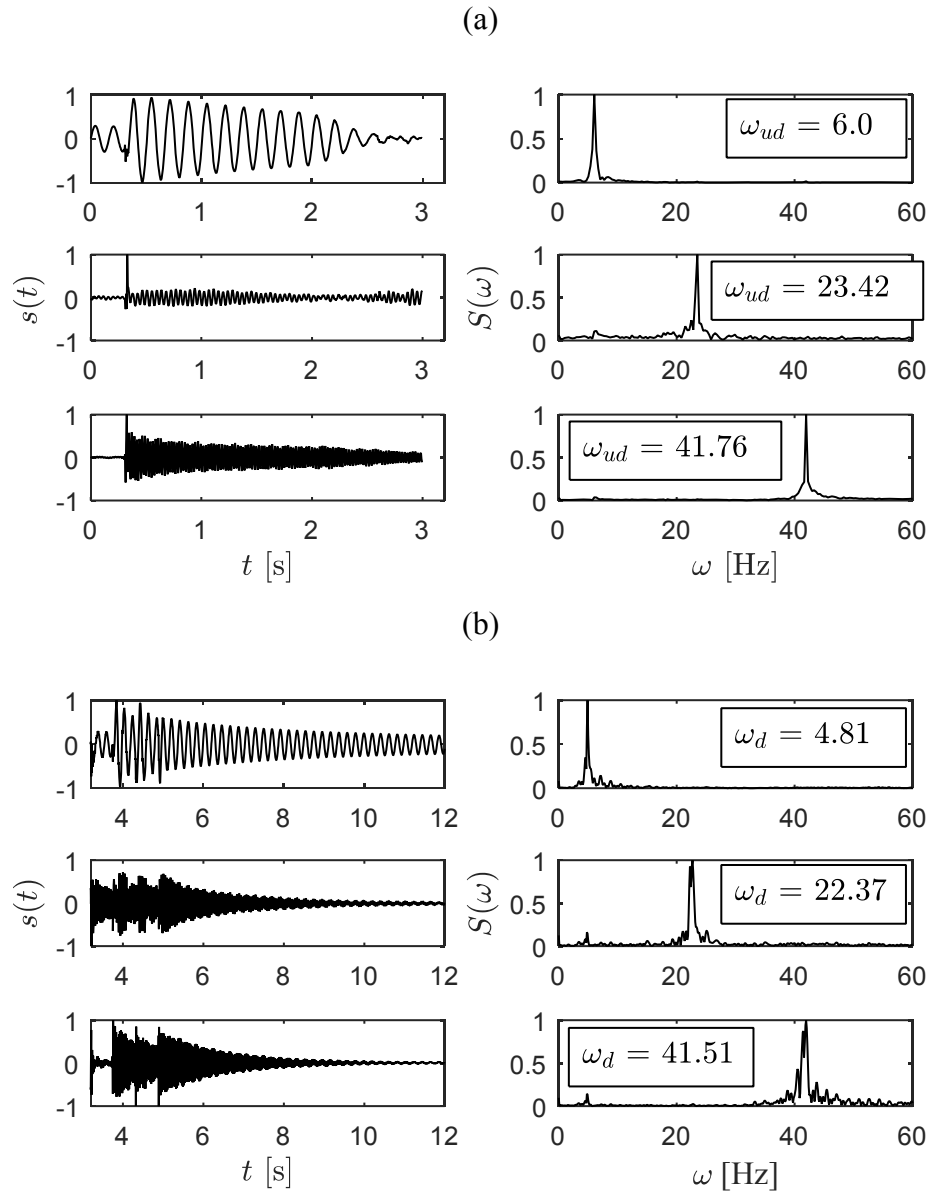


Figure 3.7: Separated sources (a)  $s_{ud}(t)$  and (b)  $s_d(t)$  of  $C_1$

Using the information of damage instant, the MMRs are separated and the damaged  $s_d(t)$  and undamaged  $s_{ud}(t)$  modal responses are extracted to obtain the accurate natural frequencies,  $\omega_d$  and  $\omega_{ud}$  and mode shape matrices,  $\hat{A}_d$  and  $\hat{A}_{ud}$  respectively. Figure 3.7 (a) and (b) show the separated results of both the cases and the modal information such as natural frequencies, damping ratios and mode shapes are calculated from herein.

The modal parameters for both the damaged and undamaged cases are tabulated in Table 3.1 along with a comparison of FE analysis. The prediction of the natural frequencies from FE model are within acceptable range to the natural frequencies determined through the proposed method. The logarithmic decrement method is employed to estimate damping ratios of the undamaged and damaged modal responses.

Table 3.1: Identified  $\omega$  and  $\xi$  of  $s_{ud}(t)$  and  $s_d(t)$  of the 3-DOF model under  $C_1$

Mode #	Proposed method					FE	
	$\omega_{ud}$ [Hz]	$\xi_{ud}$ [%]	$\omega_d$ [Hz]	$\xi_d$ [%]	Severity of damage [%]	$\omega_{ud}$ [Hz]	$\omega_d$ [Hz]
1	6.00	6.35	4.81	1.58	19.83	6.32	4.84
2	23.42	1.12	22.37	0.47	4.48	23.85	23.03
3	41.76	1.07	41.51	0.64	0.59	40.84	40.36

### 3.2.2 Damage Identification in $C_2$

Figure 3.2 (b) shows the model of  $C_2$ , which is a 3-DOF structure with steel wire bracing as depicted in the picture with yellow circles. The data was collected from the healthy state of the structure for some moment and then, the steel wires were cut to introduce sudden reduction in stiffness. Figure 3.8 (a) and (b) show the Fourier spectra of the measured signals

and the resulting modal responses as obtained from the SOBI, respectively. Again, the damage instant is hardly distinguishable from the HT analysis as shown in Figure 3.9. Then the TVAR algorithm is employed on the modal responses. Figure 3.10 and Figure 3.11 clearly indicate that the damage occurs at  $t_d = 2$  seconds. The resulting modal parameters for both damaged and undamaged states of  $C_2$  are then extracted as shown in Figure 3.12 and are tabulated in Table 3.2.

Table 3.2: Identified  $\omega$  and  $\xi$  of  $s_{ud}(t)$  and  $s_d(t)$  of the 3-DOF model under  $C_2$

Mode #	Proposed method					FE	
	$\omega_{ud}$ [Hz]	$\xi_{ud}$ [%]	$\omega_d$ [Hz]	$\xi_d$ [%]	Severity of damage [%]	$\omega_{ud}$ [Hz]	$\omega_d$ [Hz]
1	6.57	4.46	6.34	3.67	3.50	7.10	6.32
2	24.94	1.28	23.87	1.13	4.29	24.90	23.85
3	43.08	0.79	42.62	0.94	1.07	42.80	41.24

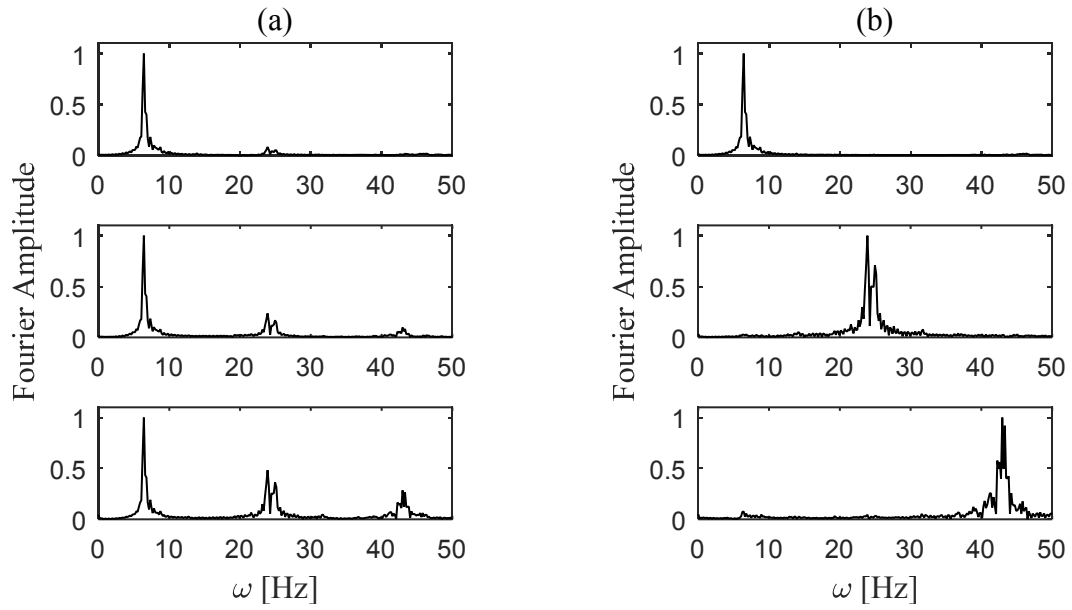


Figure 3.8: Fourier spectra of (a) the observed signals and (b) MMRs of  $C_2$

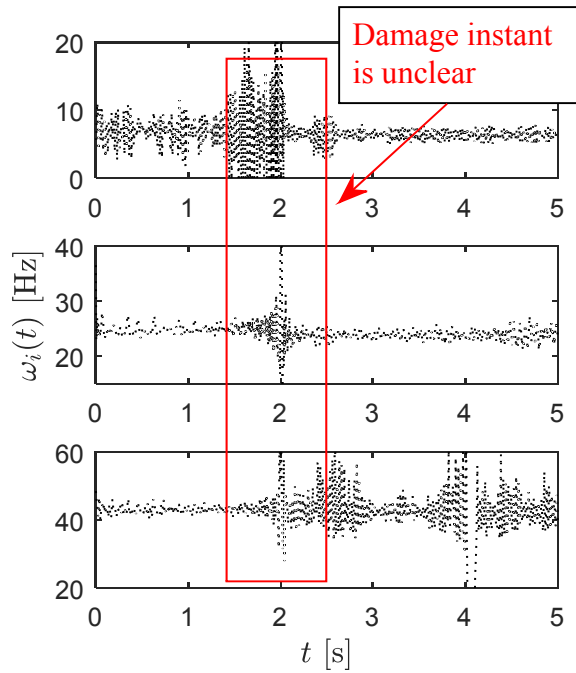


Figure 3.9: HT applied to all MMRs of  $C_2$

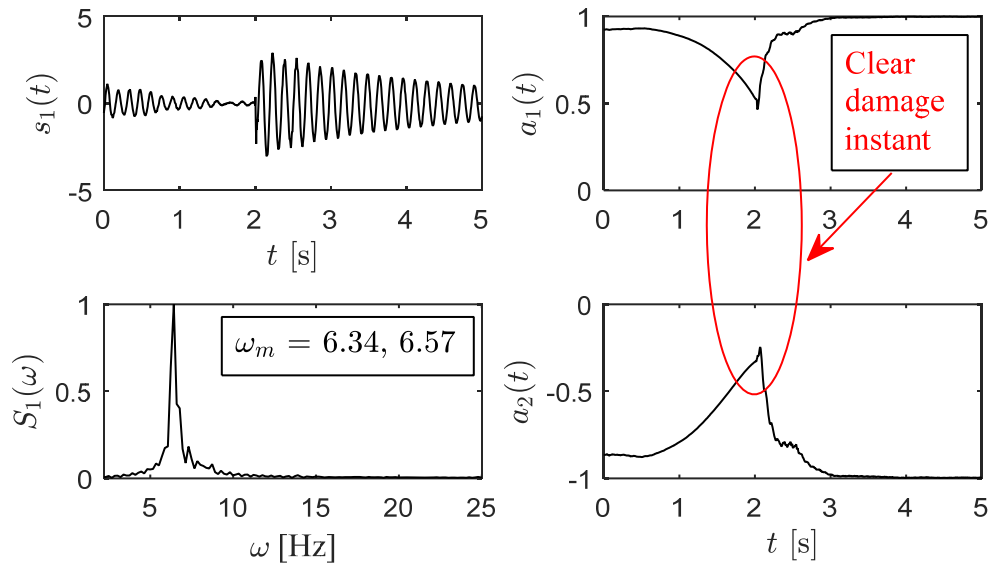


Figure 3.10: TVAR modeling of the first MMR of  $C_2$

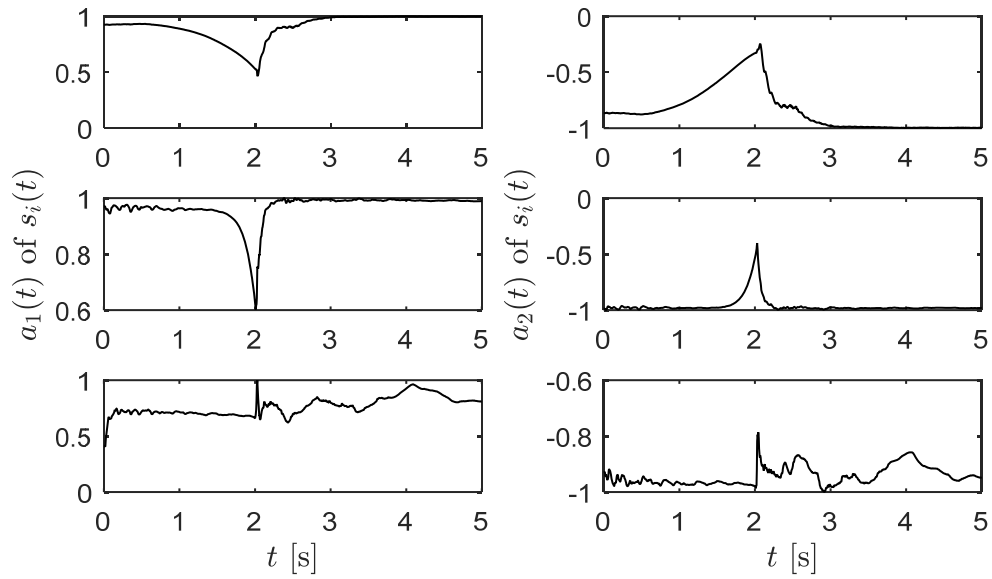


Figure 3.11: TVAR modeling of all MMRs of  $C_2$

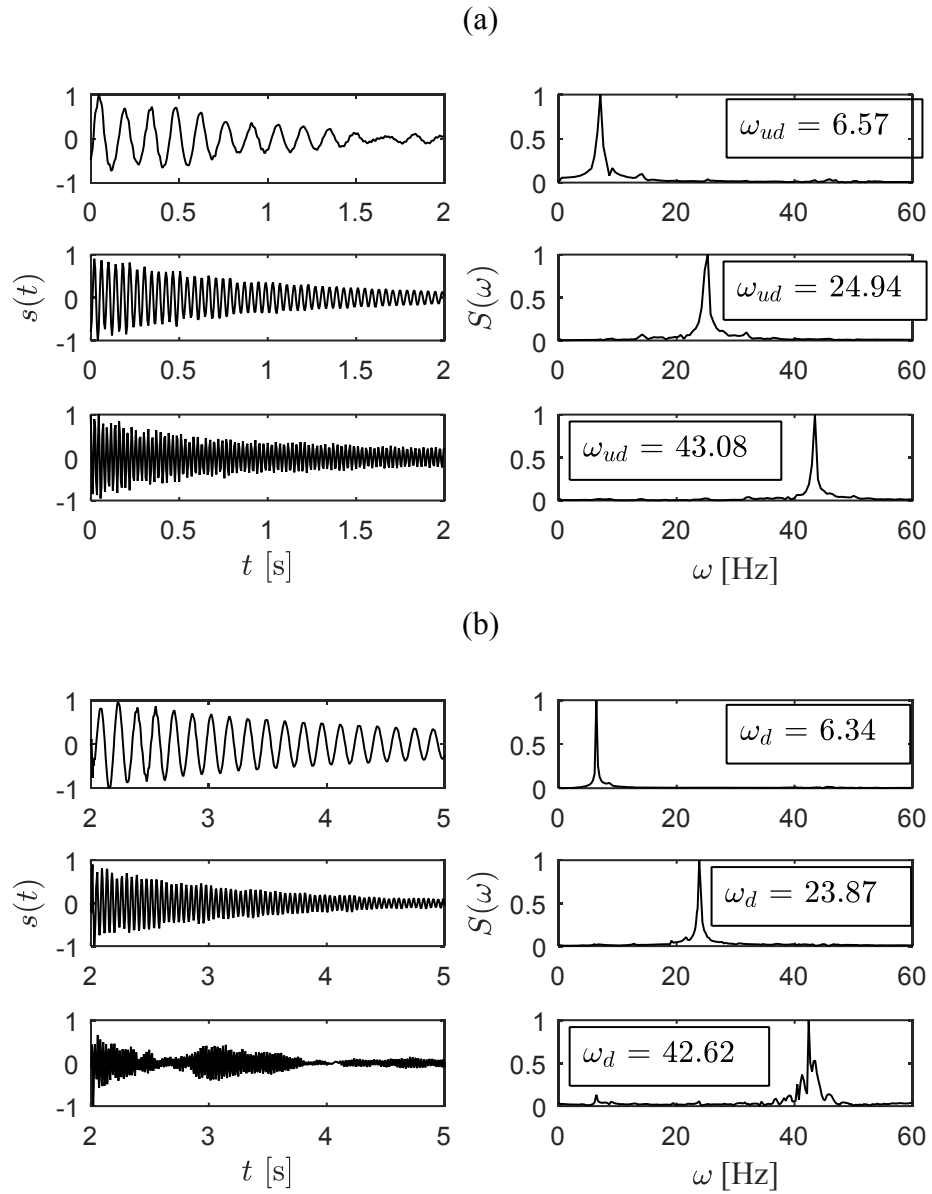


Figure 3.12: Separated sources (a)  $s_{ud}(t)$  and (b)  $s_d(t)$  of  $C_2$

### 3.3 Full-Scale Study

In this section, recorded ambient and earthquake-excited responses from the University of California, Los Angeles, (UCLA) Doris and Louis Factor building (Kohler et al., 2005) are utilized to illustrate the proposed damage detection method. A general elevation and floor plan of this building is shown in Figure 3.13 consisting of several centers for the health sciences and other biomedical facilities of UCLA. This building is one of the heavily instrumented buildings in North America, whose vibration data is made available for researchers world-wide through a remote data-base server designed and constructed in the late 1970s. The 17-storey building is composed of special moment resisting steel frames (SMFs) supported by concrete bell caissons and spread footings. Following the 1994 Northridge earthquake, the building was instrumented with an array of 72 Kinematics FB-11 uniaxial-accelerometers at the floor levels including the basement and the sub-basement levels. Each level has two pairs of orthogonal sensors parallel to the NS and EW directions as shown in Figure 3.13 (Sadhu, 2013).

In this chapter, floor accelerations recorded on September 28, 2004 at 10:15 AM PDT are used. Typical measured accelerations at roof and middle floor are plotted in Figure 3.14. Sudden jump in the roof acceleration around  $t = 400$  sec indicates the occurrence of the Parkfield earthquake. This earthquake, with  $M_w = 6.0$  on the moment magnitude scale originated in Parkfield, CA, epi-centered 163 miles from the UCLA. The peak acceleration response recorded at the roof of the building was 0.0025 g. Due to the earthquake, there were damages in the building for which the natural frequencies of the structure were reduced by significant amount (Nayeri et al., 2008). Figure 3.15 shows the Fourier spectra of the vibration data and reveals that the most of the energies were concentrated within 5 Hz. Also the presence of frequency coupling (i.e., both undamaged and damaged frequencies) is anticipated due to the occurrence of Parkfield earthquake. Therefore, this data sets an appropriate test bed for the proposed algorithm.

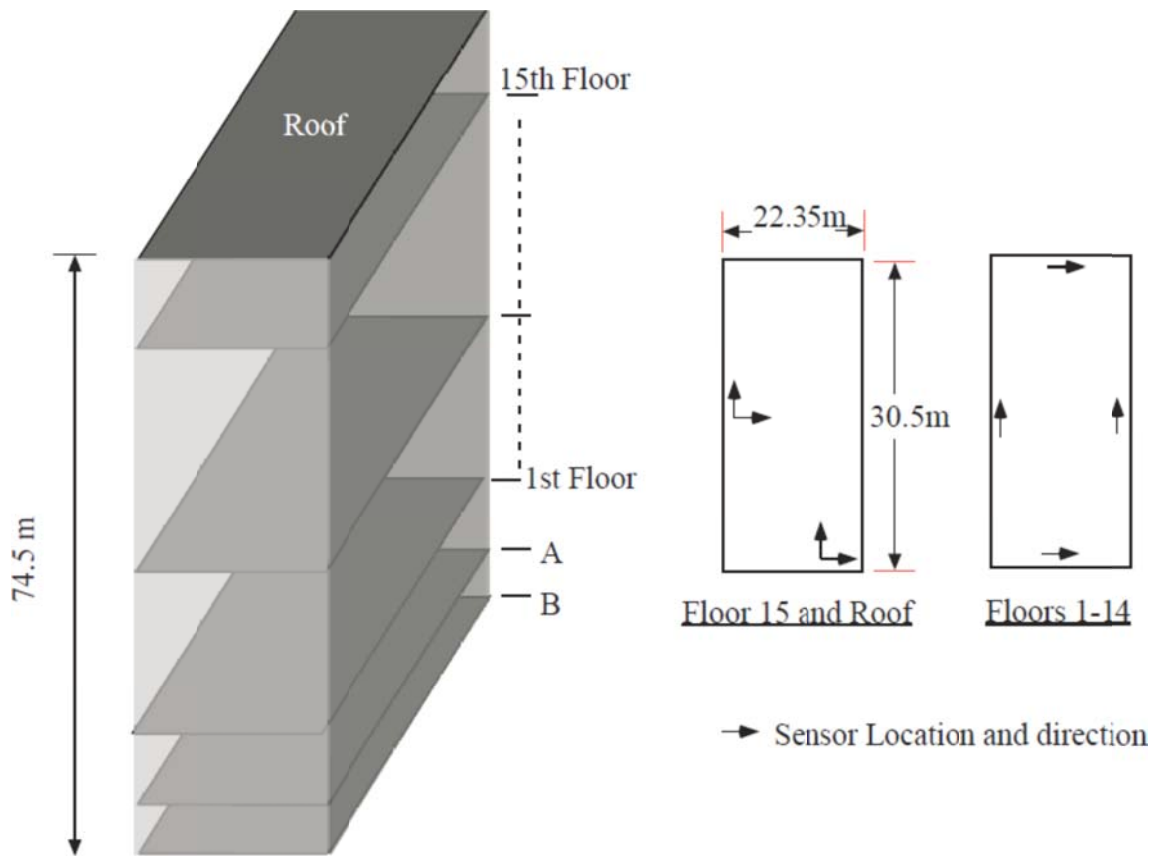


Figure 3.13: Layout of the UCLA Factor building and the sensor locations

In order to delineate undamaged and damaged frequencies, the SOBI is undertaken in the vibration data and all the modal responses with MMR are extracted. Figure 3.16 (left sub-figures) shows the resulting first modal response and its Fourier spectra containing both undamaged and damaged states. Then the TVAR modeling is undertaken over this modal response, and the resulting AR coefficients are plotted in the right sub-figures which clearly reveal the initiation of damage due to the occurrence of earthquake around  $t_d = 400$  seconds.

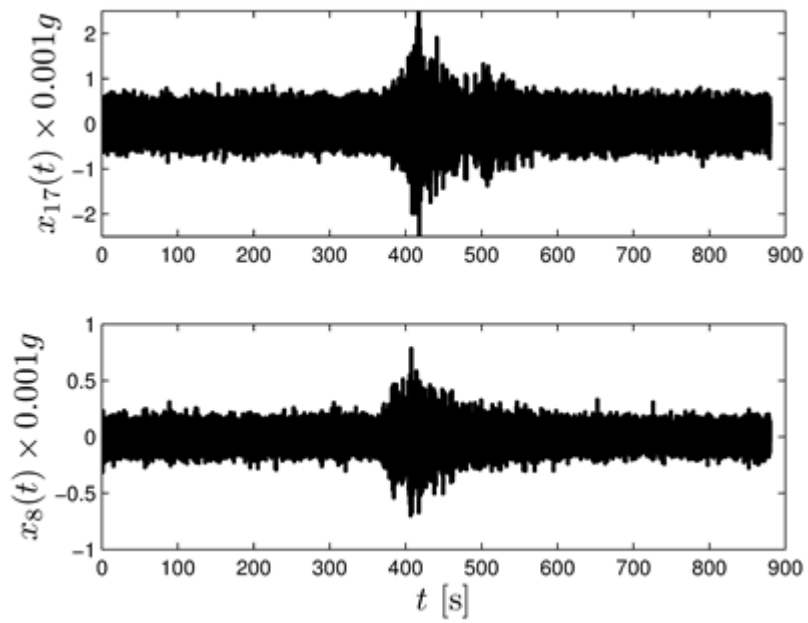


Figure 3.14: Vibration measurement of the UCLA Factor building under Parkfield earthquake

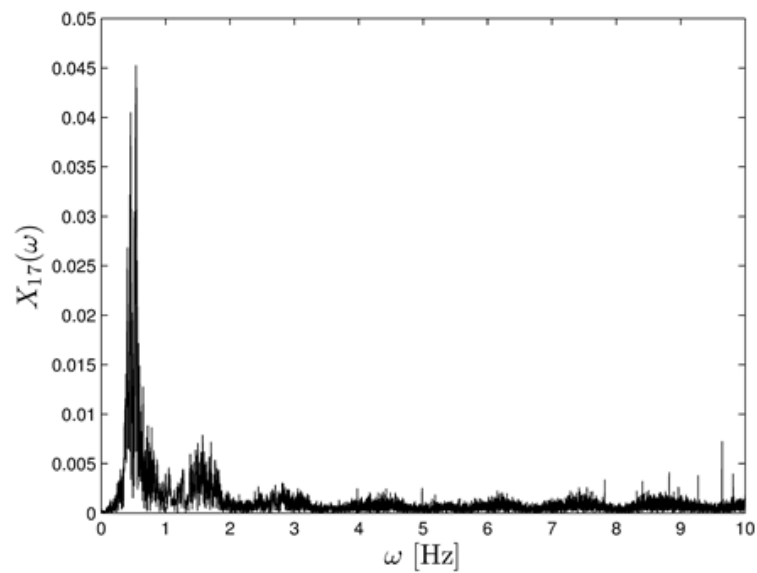


Figure 3.15: Fourier spectra of the top floor response of the UCLA Factor building

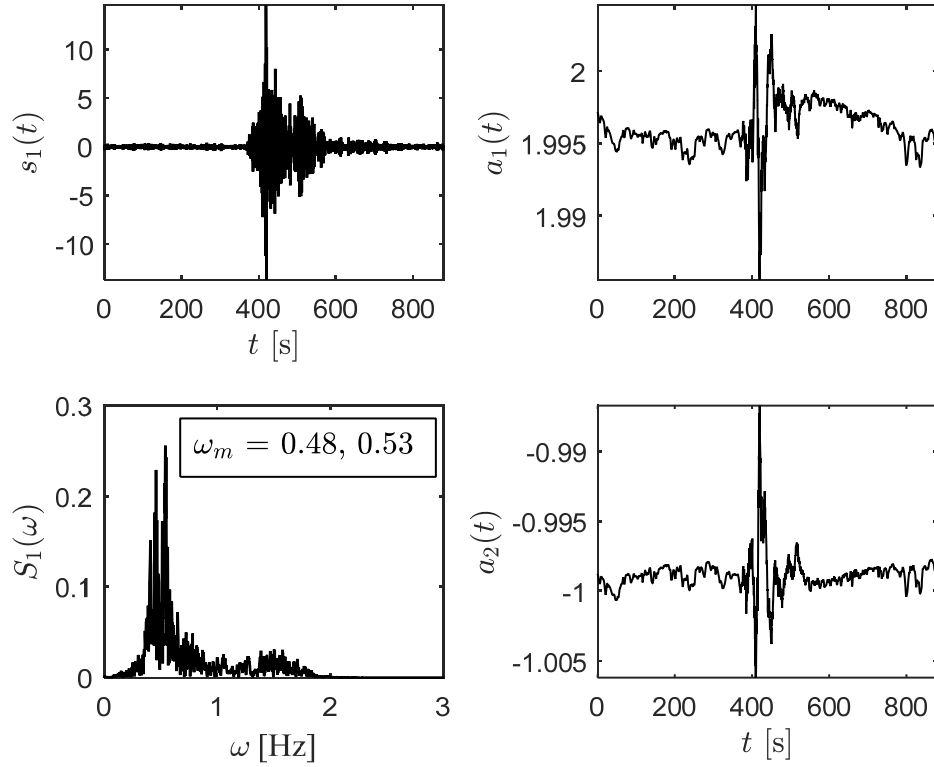


Figure 3.16: TVAR modeling of the first MMR of the UCLA Factor building

Once the damage instant is identified, the modal responses are separated for both the segments and the natural frequencies of both undamaged and damaged states can be easily identified as demonstrated in section 3.1. Similar analysis can be performed in all other modal responses and the detailed identification results are shown in Table 3.3. The results are also compared with a traditional system identification method, stochastic subspace identification (SSI) (Skolnik et al., 2006). It may be noted that SSI is employed on undamaged and damaged segments of the raw data separately as soon as the damage instant is identified using the proposed method. Furthermore, unlike the proposed method, SSI is a computationally intensive method that includes several user interventions including model-

order selection and stability diagram (Skolnik et al., 2006). It may be observed that the results are closely corroborating with the SSI results. With the modal parameters of undamaged and damaged states, the severity of damage can be also assessed.

Table 3.3: Identification results of the proposed method from UCLA Factor building

Mode #	Directions	Frequency [Hz]		Damping [%]	
		SSI	Proposed	SSI	Proposed
		$\omega_{ud}(\omega_d)$	$\omega_{ud}(\omega_d)$	$\xi_{ud}(\xi_d)$	$\xi_{ud}(\xi_d)$
1	EW	0.55(0.47)	0.53(0.48)	5.1(4.8)	5.5(4.2)
2	NS	0.59(0.51)	0.58(0.51)	8.3(4.7)	7.3(4.9)
3	Tor	0.81(0.68)	0.82(0.69)	10.8(5.8)	10.1(6.2)
4	EW	1.63 (1.49)	1.65(1.53)	2.1(5.4)	2.4(5.9)
5	NS	1.79(1.67)	1.77(1.68)	1.4(4.9)	1.7(4.6)
6	Tor	2.48(2.36)	2.5(2.37)	2.9(7.4)	2.8(7.8)
7	EW	2.83(2.68)	2.82(2.66)	2.2(4.4)	2.6(4.7)
8	NS	3.06(2.86)	3.09(2.89)	1.3(4.9)	2.1(4.8)
9	Tor	4.02(3.83)	4.05(3.89)	2.9(4.6)	2.8(4.9)

### 3.4 Summary

In this chapter, the applicability of the proposed damage detection method is validated on the vibration data obtained from the two lab-scale damage cases. The modal parameters obtained from the proposed algorithm are also compared with the FE model. The proposed algorithm is further demonstrated on “real-life” vibration data of the UCLA Factor building. The results from the proposed method are in agreement with the SSI method.

## Chapter 4

# Identification of Instantaneous Frequencies of an Axially-Moving Cantilever Beam

In this chapter, identification of instantaneous frequencies (IF) of an axially-moving cantilever beam is investigated. The axially-moving cantilever beam is a typical linear time-varying (LTV) system. Different from the parameters in the systems dealt with in the previous chapters, the IFs of this system vary continuously when the beam is moving axially. This poses a challenge to identification. First the dynamic model governing the axially-moving beam is briefly reviewed. Then the algorithm proposed in Chapter 2 is applied to identify the IFs. In addition, the other two existing methods, namely the wavelet transform (WT) and Hilbert vibration decomposition (HVD), are also employed.

The rest of the chapter is organized as follows. Section 4.1 presents an overview of the dynamic model for the axially-moving cantilever beam system. Section 4.2 discusses how to identify the IFs using the proposed algorithm. Section 4.3 presents computer simulations in which the proposed algorithm is used to identify the IFs. Section 4.4 presents the experimental setup. Section 4.5 studies the WT to identify the IFs of the axially-moving cantilever beam. Section 4.6 discusses the results of the identified IFs using the WT. Section 4.7 presents the HVD method for the system identification. Section 4.8 presents the identified IFs obtained from the HVD method. Section 4.9 presents the identified IFs obtained from the HVD plus TVAR method. Finally, section 4.10 contains summary and conclusions.

### 4.1 Dynamic Model of an Axially-Moving Cantilever Beam

Figure 4.1 shows a schematic of an axially-moving beam in which  $w(s, t)$  denotes the lateral displacement of the beam. In order to transfer a partial differential equation (PDE) to  $n$

ordinary differential equation (ODE)  $w(s, t)$  is decomposed as

$$w(s, t) = \sum_{i=1}^n \phi_i(s) q_i(t) = \mathbf{\Phi}(s) \mathbf{q}(t) \quad (4.1.1)$$

where,  $w(s, t)$  represents the lateral displacement of axial location  $s$  at time  $t$ ,  $n$  is the number of modes, and  $q_i(t)$  and  $\phi_i(s)$  are the  $i^{th}$  generalized coordinate and mode shape or eigenfunction of the “stationary” cantilever beam. In Deng, (2002), the relation between the axial location  $s$  and the length of beam  $l$  is related by

$$s = \alpha l, \quad 0 \leq \alpha \leq 1 \quad (4.1.2)$$

Consequently, the lateral displacement can then be expressed as

$$w(\alpha, t) = \mathbf{\Phi}(\alpha) \mathbf{q}(t) \quad (4.1.3)$$

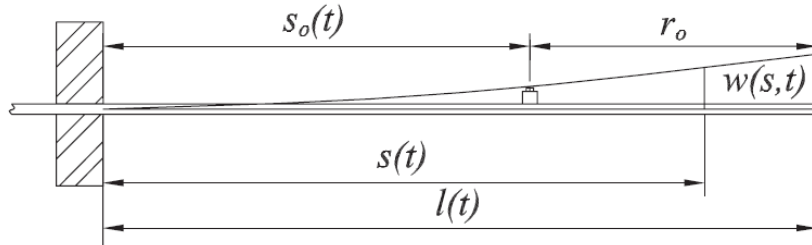


Figure 4.1: Schematic of axially-moving cantilever beam

where,

$$\mathbf{\Phi}(\alpha) = [\phi_1(\alpha) \phi_2(\alpha) \dots \phi_n(\alpha)], \quad \mathbf{q}(t) = [q_1(t) q_2(t) \dots q_n(t)]^T \quad (4.1.4)$$

The dynamic model of the beam was developed based on the following assumptions (Deng, 2002):

- The beam is assumed to be an Euler-Bernoulli beam
- Axial motion is only function of time
- Lateral displacement gradients are small
- The axial rigidity is much higher than the flexural rigidity
- Axial force is negligible

The simplified ODE governing the lateral motion of the beam subjected to zero external force is given as follows,

$$\ddot{\mathbf{q}}(t) + \mathbf{D}(t)\dot{\mathbf{q}}(t) + \mathbf{K}(t)\mathbf{q}(t) = \mathbf{0}_{n \times 1} \quad (4.1.5)$$

$$\mathbf{D}(t) = \frac{2\dot{l}}{l} \mathbf{A}_1 + \frac{\gamma}{m} \mathbf{I}_{n \times n}, \quad \mathbf{K}(t) = \left[ \frac{\ddot{l}}{l} - 2 \left( \frac{\dot{l}}{l} \right)^2 + \frac{\gamma \dot{l}}{m l} \right] \mathbf{A}_1 + \left( \frac{\dot{l}}{l} \right)^2 \mathbf{A}_2 + \frac{EI}{ml^4} \mathbf{A}_3 \quad (4.1.6)$$

where,  $\mathbf{A}_1$ ,  $\mathbf{A}_2$ , and  $\mathbf{A}_3 \in \mathbb{R}^{n \times n}$  are constant matrices, the over-dots represent derivative with respect to time.  $EI$  is the flexural rigidity of the beam.  $\gamma$  is the damping value per unit length of the beam.  $m$  is the mass per unit length of the beam, and  $\mathbf{A}_3$  is a diagonal matrix or  $A_3 = \text{diag}[(\beta_1 L)^4 \quad (\beta_2 L)^4 \quad \dots \quad (\beta_n L)^4]$ . Equation (4.1.5) can be transformed into a state space representation by introducing the following state vector  $\mathbf{x} = [\mathbf{q}^T \quad \dot{\mathbf{q}}^T]^T$

$$\dot{\mathbf{x}}(t) = \mathbf{A}(t)\mathbf{x}(t) \quad (4.1.7)$$

where, system matrix  $\mathbf{A}(t)$  is given by

$$\mathbf{A}(t) = \begin{bmatrix} \mathbf{0}_{n \times n} & \mathbf{I} \\ -\mathbf{K}(t) & -\mathbf{D}(t) \end{bmatrix} \quad (4.1.8)$$

To observe vibration at a particular location  $r_o$  on the beam using sensors such as strain gauge and accelerometer, the output vector  $\mathbf{y}(t)$  which is related to the state vector  $\mathbf{x}(t)$  by an output matrix  $\mathbf{C}(t)$  could be constructed as follows. First, lets define

$$s_o = l - r_o \quad or \quad \alpha_o = 1 - \frac{r_o}{l} \quad (4.1.9)$$

where,  $r_o$  is measured from the tip of the beam. The output of strain gauge sensor  $\mathbf{y}_{sg}(t)$  is a voltage signal proportional to the strain with the system measurement gain  $K_{sg}$ .

$$\mathbf{y}_{sg}(t) = \frac{K_{sg}}{l^2} \Phi''(\alpha_o) \mathbf{q}(t), \quad (4.1.10)$$

where primes denote partial derivative with respect to  $\alpha$ . The output of accelerometer sensor  $\mathbf{y}_a(t)$  is a voltage signal proportional to acceleration of the beam with the system measurement gain of  $K_a$

$$\mathbf{y}_a(t) = -K_a \left[ \left( \frac{\gamma \dot{l}}{ml} \right) (1 - \alpha_o) \Phi'(\alpha_o) + \frac{EI}{ml^4} \Phi'''(\alpha_o) \right] \mathbf{q}(t) + K_a \frac{\gamma}{m} \Phi(\alpha_o) \dot{\mathbf{q}}(t) \quad (4.1.11)$$

In the numerical and experimental studies, three locations are chosen to observe the vibration  $r_{o1} = 0.643$  m for strain gauge sensor which is close at the base near clamp boundary and denoted as BSG,  $r_{o2} = 0.335$  m for middle accelerometer sensor (MAC), and  $r_{o3} = 0.001$  m for tip accelerometer sensor (TAC). The output vector is related to state vector by

$$\mathbf{y}(t) = \mathbf{C}(t)\mathbf{x}(t) \quad (4.1.12)$$

where,  $\mathbf{C}(t)$  is  $3 \times 2n$  time-varying output matrix defined by

$$\mathbf{C}(t) = \begin{bmatrix} \frac{K_{sg}}{l^2} \Phi''(\alpha_{o1}) & \mathbf{0}_{1 \times 3} \\ -K_a \left[ \left( \frac{\gamma \dot{l}}{ml} \right) (1 - \alpha_{o2}) \Phi'(\alpha_{o2}) + \frac{EI}{ml^4} \Phi'''(\alpha_{o2}) \right] & K_a \frac{\gamma}{m} \Phi(\alpha_{o2}) \\ -K_a \left[ \left( \frac{\gamma \dot{l}}{ml} \right) (1 - \alpha_{o3}) \Phi'(\alpha_{o3}) + \frac{EI}{ml^4} \Phi'''(\alpha_{o3}) \right] & K_a \frac{\gamma}{m} \Phi(\alpha_{o3}) \end{bmatrix} \quad (4.1.13)$$

## 4.2 Estimation of the Instantaneous Frequencies through the TVAR Modelling

A well-known technique for estimating the instantaneous frequencies or IF of a nonstationary signal is to use the time-varying coefficients  $a_i(t)$  of the TVAR model (Ravi & Rao, 2014; Wang & Liu, 2009; Yao & Pakzad, 2012). This approach is slightly more accurate compared to the time varying power spectral density estimation process according to Nguyen, (2009). Since, in the time varying power spectrum, one has to locate the IF as the largest spectral peak location. Thus, by extracting the IF from the TVAR model we can eliminate the process of selecting the largest spectral peak.

The time varying transfer function of the TVAR model can be represented as (Peijun et al., 1998),

$$H(z, t) = \frac{1}{1 + \sum_{i=1}^p a_i(t) z^{-i}} \quad (4.2.1)$$

Depending on the model order  $p$ , the above equation would have  $z_i(t)$ ,  $i = 1, 2, \dots, p$  roots or poles at each instant  $t$ . At each instant, the poles that correspond to the nonstationary

signal appear on or near the unit circle and the poles away from the unit circle correspond with the noise. Furthermore, in case of real signal, these roots are most likely pairs of complex conjugate, therefore one may only need to use one pair of complex conjugate root for frequency estimation. Using the poles correspond to the nonstationary signal, we can

estimate the instantaneous phase  $\phi(t) = \arctan\left(\frac{\text{Im}(z_i(t))}{\text{Re}(z_i(t))}\right)$  and by taking the time

derivative of  $\phi(t)$ , the instantaneous frequency can be calculated as  $f(t) = \frac{1}{2\pi} \frac{d}{dt} \phi(t)$ .

### 4.3 Computer Simulation

The algorithm developed in Chapter 2 assumes that the parameter change is abrupt such that the responses are piece-wise stationary. However, the parameters of the axially-moving beam vary continuously when the beam is moving. In order to test whether the proposed algorithm is capable of identifying the IFs of the axially-moving beam, a computer simulation is conducted. The numerical study is based on the following data: the beam is made of aluminum and its cross-sectional dimension is 3.175 mm (thickness)  $\times$  50.8 mm (width). The length density of the beam is  $m=0.4516$  kg/m, the flexural rigidity of the beam is  $EI=9.7148 \left[ \frac{N}{m^2} \right]$ , and the damping value per unit length of the beam is  $\gamma = 0.1240 \left[ \frac{Ns}{m^2} \right]$ . Two scenarios are considered; beam extension and beam retraction. The beam length varies from  $L_{\min}= 0.66$  [m] to  $L_{\max}=1.09$  [m] in beam extension and vice versa in beam retraction. The first three modes are considered or  $n=3$  for identification. The trapezoidal velocity profile shown in Figure 4.2 is used as the axial motion of the beam (Deng, 2002). The fourth-order Runge-Kutta method is used to solve equation (4.1.7) with the time step of 0.001 second and the whole simulation is run for 9 seconds. The measurement gains of the three sensors are chosen as  $K_{sg} = 1$  [V],  $K_a = 1$  [V/m.s<sup>-2</sup>] and the initial conditions are chosen as

$[q_1(0) \ q_2(0) \ q_3(0) \ \dot{q}_1(0) \ \dot{q}_2(0) \ \dot{q}_3(0)] = [0.5 \ -0.1 \ 0.05 \ 0 \ 0 \ 0]$  for both of the scenarios.

The initial conditions are chosen in such a way that all three modes are sufficiently excited out.

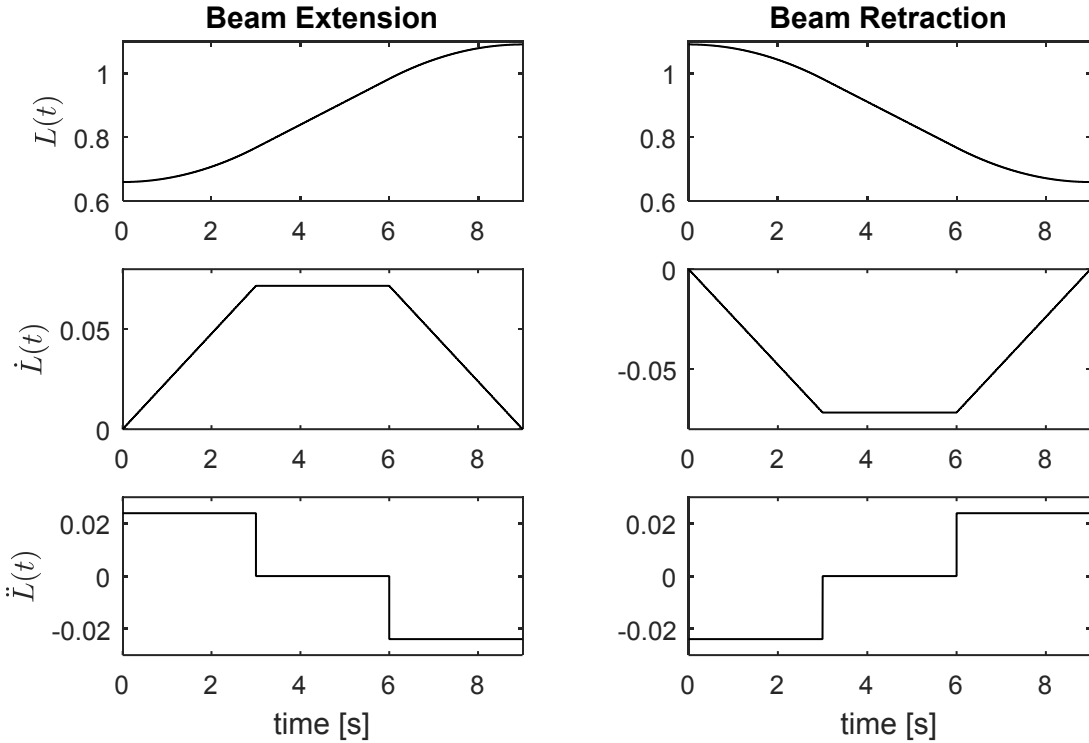


Figure 4.2: Axial motion profile of beam extension and beam retraction scenarios

### *Beam Extension Scenario*

The vibrations observed at the three locations are shown in Figure 4.3 (a), where  $x_1(t)$ ,  $x_2(t)$ , and  $x_3(t)$  represents vibration signals obtained from BSG, MAC and TAC sensor, respectively. Figure 4.3 (b) show, the corresponding FFT spectra of the signals. The vibration signal obtained from the BSG sensor has little contribution from the 2<sup>nd</sup> and 3<sup>rd</sup> modes. Similarly, the vibration signal obtained from the MAC sensor has little contribution of the 3<sup>rd</sup> mode. The vibration observed at the tip is rich in the modal responses.

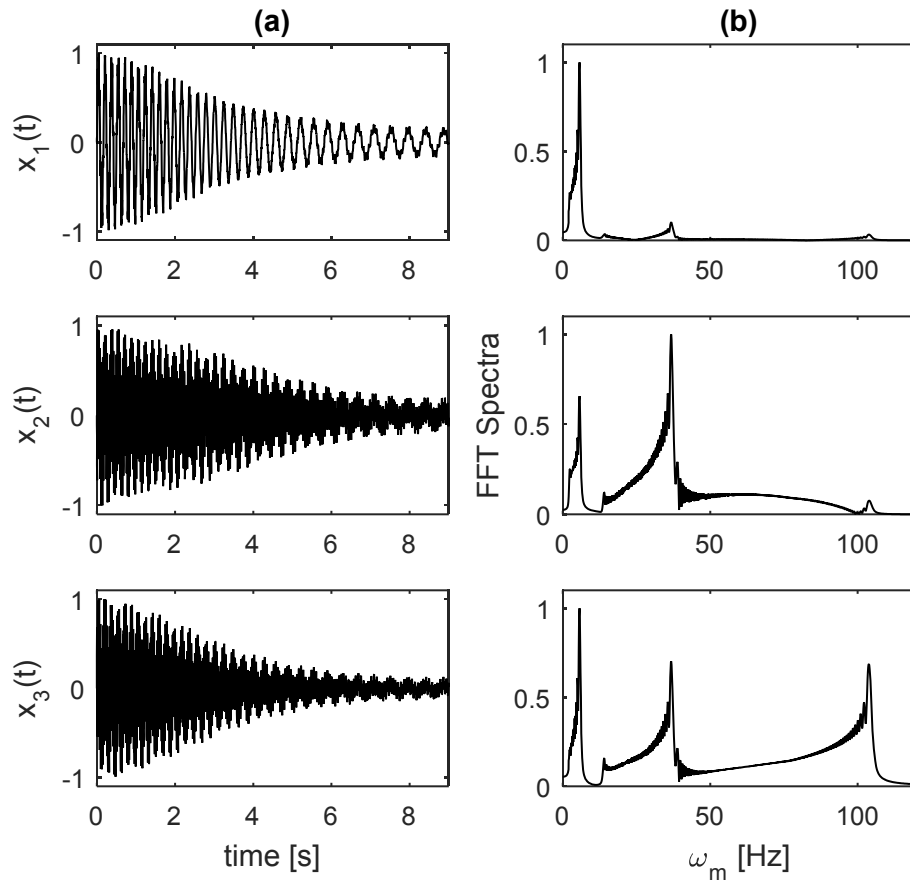


Figure 4.3: Beam extension: (a) responses and (b) their corresponding FFT spectra

Now the SOBI method is utilized to decompose all three vibration signals. The results are shown in Figure 4.4. It can be seen from the figure that the SOBI was able to decompose the vibration signals into the modal responses. However, the obtained modal responses are not exactly unimodal, especially in the second and third modes. It is known that the SOBI method works on the statistical properties of a signal assuming that the amplitude and frequency do not change over time. This assumption holds true for stationary signal only. In contrast, the acquired vibration signals in this study are fast modulated in amplitude (or variance change over time) and in frequency (Sadhu, 2013). Therefore, when the SOBI

formulates the covariance matrices, the change in the statistical properties of the nonstationary signals are not considered hence resulting in the mixed modal responses (MMRs). In other words, the SOBI does a global decomposition as opposed to local one.

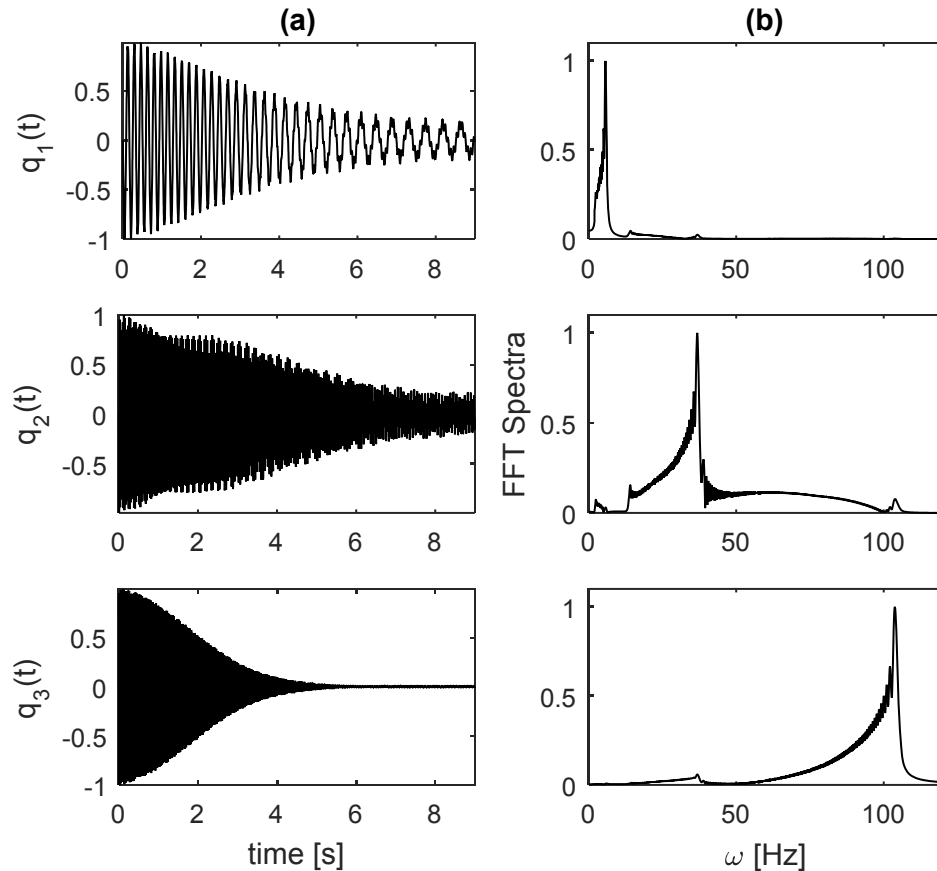


Figure 4.4: Beam extension: (a) vibratory mode responses obtained from SOBI and (b) their respective FFT spectra

It should be noted that the SOBI does minimize the energy of other modes at each decomposed mode. This observation can be explained by the SVD applied on the covariance matrix  $[R_x(0)]$  to obtain global singular values and eigenvectors associated with them. Using

this global singular values, the estimated mixing matrix  $\hat{A}$  is obtained where the contribution of other modes at each decomposed mode has been suppressed.

Next, the IF of each decomposed vibratory mode is estimated by utilizing the TVAR method. The model order  $p = 2$  is used for the TVAR method to estimate the MMR obtained from the SOBI. The time-varying coefficients  $a_1(t)$  and  $a_2(t)$  of the TVAR method are utilized in equation (4.2.1) to estimate the IF. The results are shown in Figure 4.5. In Figure 4.5 the black solid line represents the so-called frozen IFs which are calculated by (Deng, 2002)

$$f(t) = \frac{1}{2\pi} \left( \frac{\beta_j L}{L(t)} \right)^2 \sqrt{\frac{EI}{\rho A}}, \quad j = 1, 2, 3 \quad (4.3.1)$$

where,  $\beta_1 L = 1.8751$ ,  $\beta_2 L = 4.6941$  and  $\beta_3 L = 7.8547$ .

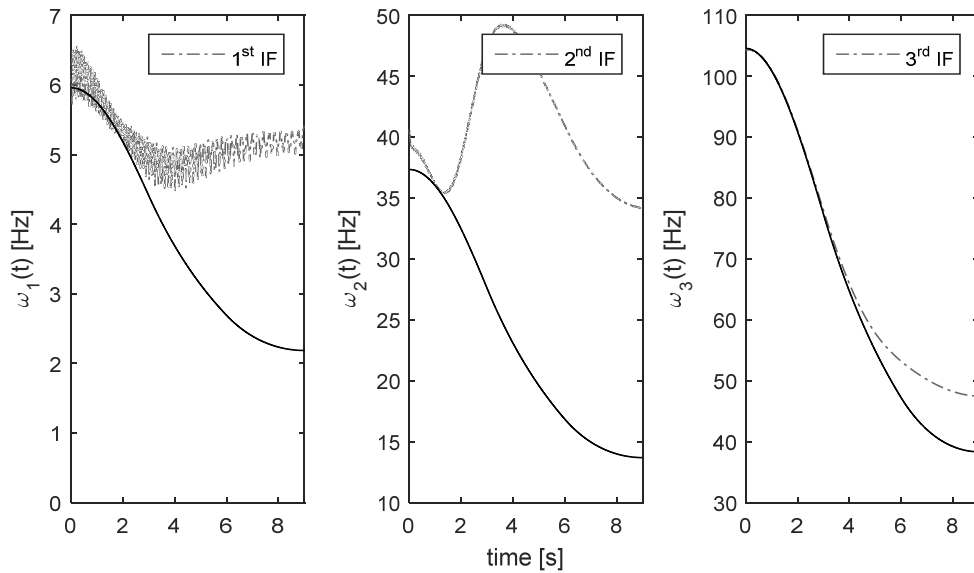


Figure 4.5: Beam extension: Comparison of the frozen IFs and IFs estimated by the TVAR method

From Figure 4.5, it can be seen that for the first and second modes, the estimated IFs fail to track the frozen IFs while for the third mode; the estimated IF follows the frozen IF up to 4 seconds.

#### *Beam Retraction Scenario*

Figure 4.6 shows the responses at the three sensor locations and their corresponding FFT spectra. It can be seen that the FFT spectra fail to reveal the varying trend of the IFs. Figure 4.7 shows the modal responses decomposed by the SOBI method and their corresponding FFT spectra. It can be seen that the SOBI is able to decompose the responses into individual modal responses. However, the FFT spectra still fail to reveal the varying trends of the IFs. Figure 4.8 compares the frozen IFs and IFs estimated using the coefficients of the TVAR model of the modal responses extracted by the SOBI. Again, for the first and second modes, the estimated IFs fail to track the frozen values while for the third mode; the estimated IF is able to track the frozen IF towards the end of the beam motion.

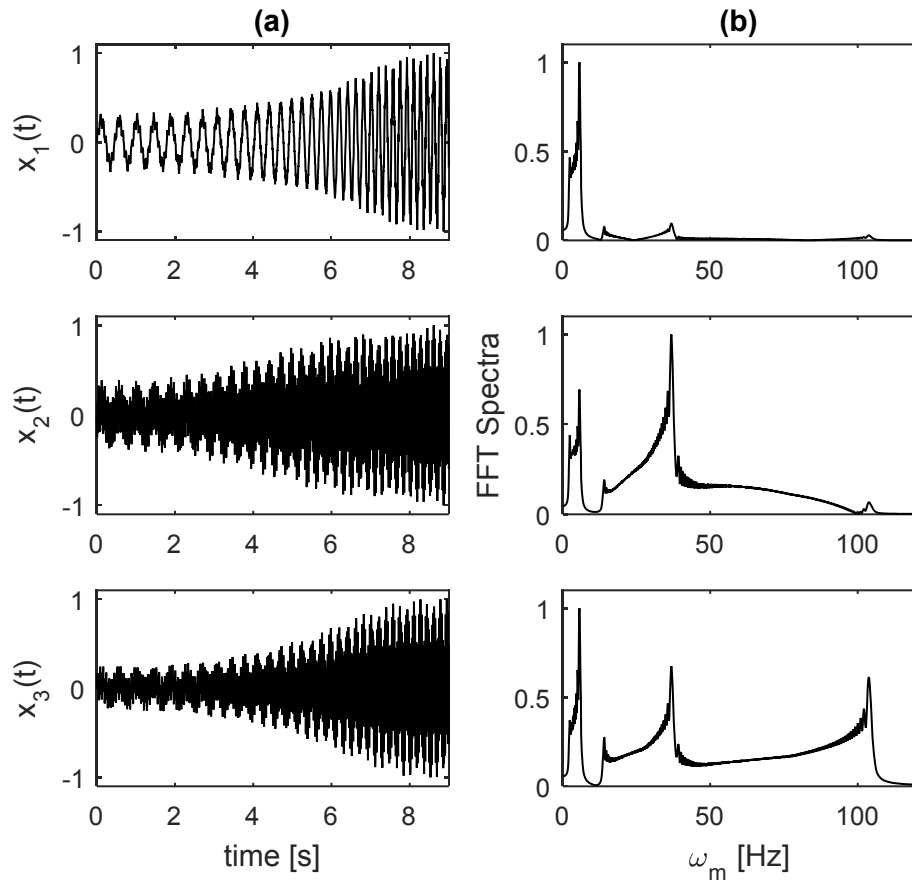


Figure 4.6: Beam retraction: (a) responses and (b) corresponding FFT spectra

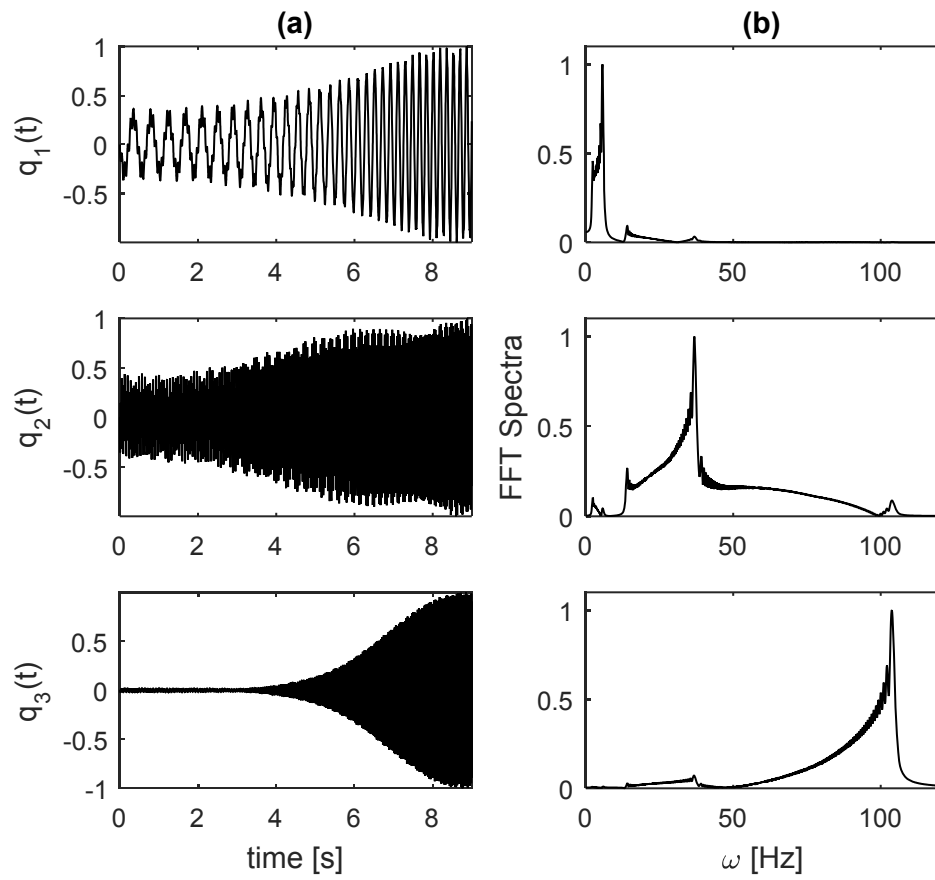


Figure 4.7: Beam retraction: (a) vibratory mode responses and (b) corresponding FFT spectra

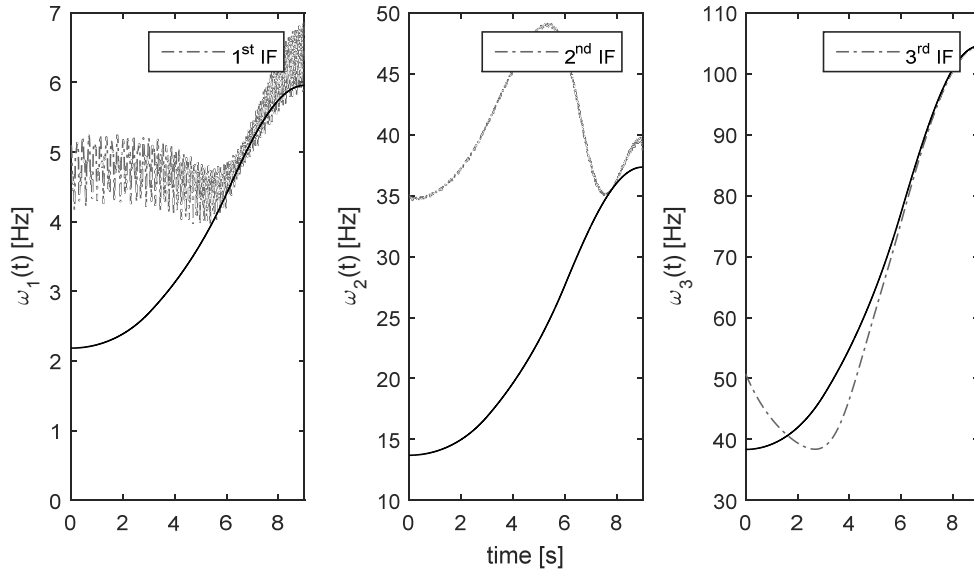


Figure 4.8: Beam retraction: comparison of the frozen IFs and IFs estimated by the TVAR method

The above numerical study has shown that the proposed algorithm fails to estimate the instantaneous frequencies of the axially-moving beam. In what follows, the other two different methods will be applied to identify the IFs using the experimental data.

#### 4.4 Experimental Setup

The experimental setup is shown in Figure 4.9. The cantilever beam is made of aluminum (6061-T6). A 12 Volt permanent magnet DC motor (DUMORE) is used to move the beam axially. The linear length variation of the beam is measured by the angular position of a potentiometer which is mounted on top of the pinion shaft. The cross-sectional dimension of the beam is 3.175 mm (thickness)  $\times$  50.8 mm (width). The length of the beam varies from 0.66 m to 1.09 m. Three sensors are utilized to measure the lateral vibration of the beam; BSG, MAC, and TAC sensors (B & K 4393V) at  $r_{o1} = 0.643$  m,  $r_{o2} = 0.335$  m and  $r_{o3} = 0.001$  m respectively. Further information on the experimental setup can be found in

Deng (2002). In Deng (2002), the natural frequencies of the first three modes of the beam at a constant length  $L$  were identified. The following relationships were established

$$\bar{f}_{d1} = \frac{2.287}{L(t)^{1.854}}, \quad \bar{f}_{d2} = \frac{14.53}{L(t)^{1.866}}, \quad \bar{f}_{d3} = \frac{40.93}{L(t)^{1.851}} \quad (4.4.1)$$

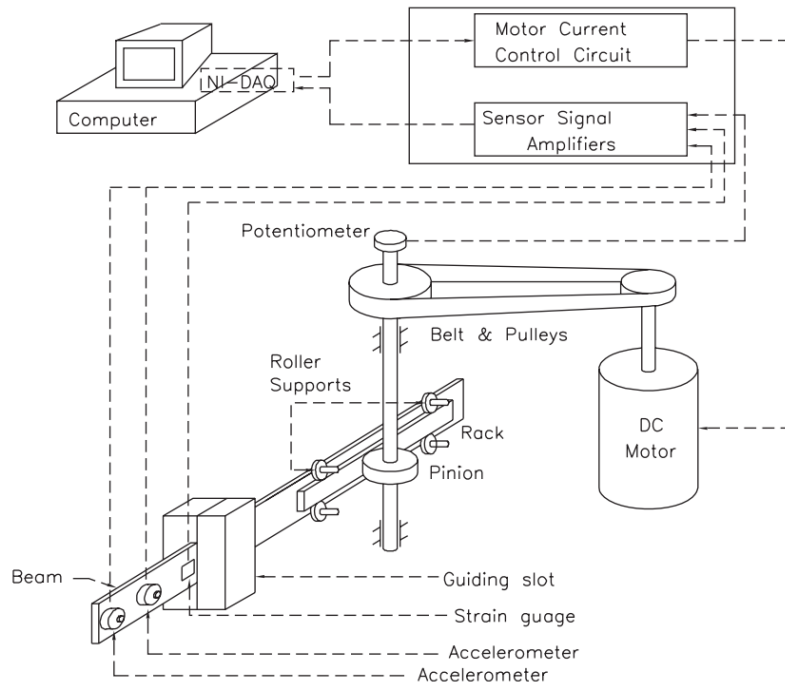


Figure 4.9: Experimental apparatus

In what follows, the experimental data obtained by Deng, (2002) was used. For each testing scenario, 40 sets of data were collected. The best of the 40 sets of data was used in the following identification. The best set of data is the one in which the responses are richest in the modal information.

## 4.5 The Wavelet Transform (WT)

The wavelet transform as discussed in Introduction is by far the most powerful method of analyzing all types of non-stationary signals (Amezquita-Sanchez & Adeli, 2014; Chen et al., 2014; Dziedziech et al., 2015; Hazra & Narasimhan, 2010; Su et al., 2014). What makes the wavelet analysis robust is its ability to change its window function (also known as wavelet basis) both in time and frequency domain, thus allowing it to analyze non-stationary signals locally. In other words, wavelet analyzes the energy concentration of non-stationary signal in time-frequency domain (Liu, 2007).

There are many wavelet bases to choose from (e.g., Haar wavelet, Gabor wavelet, Daubechies wavelet, Morlet wavelet and many more). These wavelet bases have rapid decay characteristics and when correlated with the observed signal under the transformation process, relative amount of energy that is present in each component of the observed signal at a particular time-frequency is produce. The WT of signal  $y(t)$  is a linear transformation as defined by

$$W(a,b) = \int_{-\infty}^{\infty} y(t)g_{a,b}(t)dt, \quad a > 0 \quad (4.5.1)$$

where,  $a$  is a dilation parameter,  $b$  is the translation parameter, and  $g_{a,b}(t)$  is known as mother wavelet defined by

$$g_{a,b}(t) = \frac{1}{\sqrt{a}}g\left(\frac{t-b}{a}\right) \quad (4.5.2)$$

In the above equation the function  $g$  represent the basis for wavelet transform. There are mainly two conditions that a basis function needs to satisfy and they are given in equation (4.5.3).

$$\int_{-\infty}^{\infty} g_{a,b}(t)dt = 0, \quad \int_{-\infty}^{\infty} |g_{a,b}(t)|^2 dt < \infty \quad (4.5.3)$$

In this study, Morlet wavelet is used as basis function.

$$g(t) = e^{-t^2/2} e^{j\omega_0 t} \quad (4.5.4)$$

$$G_{a,b}(\omega) = \sqrt{a} e^{-(a\omega - \omega_0)^2/2} e^{-j\omega b} \quad (4.5.5)$$

The Morlet wavelet is chosen because of its fast decay and oscillatory nature. The center frequency of the function is  $\omega_0$ . By substituting wavelet basis equation (4.5.4) into mother wavelet equation (4.5.2) then transforming the result into Fourier domain, one can obtain equation (4.5.5). In order to see how WT analyzes the nonstationary signals, let's first consider a mono-component stationary signal given by

$$y(t) = A e^{-\sigma t} \cos(\omega_d t + \phi) \quad (4.5.6)$$

where,  $A$  is the constant amplitude,  $\omega_d = \omega_n \sqrt{1 - \xi^2}$  is the damped natural frequency which depends on the natural frequency  $\omega_n$  and damping ratio  $\xi$ ,  $\sigma = \xi \omega_n$  is referred to as damping rate, and  $\phi$  is the phase. Taking Fourier transforms of  $y(t)$  and then taking product with equation (4.5.5) the wavelet coefficients  $W(a,b)$  could be obtained which defines the map of the signal  $y(t)$  in three dimensions.

$$W(a,b) = \sqrt{a} A e^{-\sigma b} e^{-\frac{(a\omega_d - \omega_0)^2}{2}} e^{j\omega_d(t+b)} \quad (4.5.7)$$

The modulus or energy of  $W(a,b)$  is as follow,

$$|W(a,b)| = \sqrt{a} A e^{-\sigma b} e^{-(a\omega_d - \omega_0)^2/2} \quad (4.5.8)$$

Taking the derivative of the above equation with respect to scale variable  $a$ , reveals that the maximum energy is concentrated at

$$a_r = \frac{\left(\omega_0 + \sqrt{2 + \omega_0^2}\right)}{2\omega_d} \approx \frac{\omega_0}{\omega_d}, \quad \text{as } \omega_0^2 \gg 2 \quad (4.5.9)$$

Substituting equation (4.5.9) back into equation (4.5.8) results in

$$|W(a_r, b)| = \sqrt{a_r} A e^{-\sigma b} \quad (4.5.10)$$

It is shown that it is possible to track  $a_r$  which is known as the ridge of wavelet in order to extract the damped natural frequency of a signal. Now coming back to nonstationary signal, again considering single-DOF response (equation (4.5.11)); analogous to stationary signal the WT performs the linear transformation on nonstationary signal as well, but because of its localization property equation (4.5.9) gives an approximation of the damped natural frequency  $\omega_d(t)$ . Furthermore, In the case of multiple-DOF LTV systems responses can be expressed as,

$$y(t) = \sum_{k=1}^n A_k(t) e^{-\sigma_k(t)t} \cos(\omega_{dk}(t)t + \phi_k) \quad (4.5.11)$$

where,  $k = 1, 2, \dots, n$  represents modes and  $n$  represents number of modes to consider. By applying the WT (equation (4.5.1)), we can achieve a 3D representation of vibration signal. Of course, one needs to set the dilation parameter  $a$  in order to cover the frequency range of the vibration signal.

#### 4.6 Identification of the Instantaneous Frequencies of the Axially-Moving Cantilever Beam Using the Wavelet Transform

All three vibration signals (i.e. BSG, MAC and TAC) are used on the WT in order to identify the IFs. The Morlet wavelet centre frequency used is  $\omega_0 = 2\pi$  rad/s or  $f_0 = 1$  Hz. The relationship between the dilation parameter  $a$  and frequency  $f_k$

$$a_k = \frac{f_0}{dt \cdot f_k} \quad (4.6.1)$$

where  $f_k$  represents frequency and  $dt$  represent the time step. Moreover, a prior knowledge of vibration signals frequency range is needed in order to specify the range for  $a$ . Thus from the numerical study equation (4.3.1) and also Table 4.1, we know the damped natural frequency of all three vibratory modes at two extreme length  $L_{\min} = 0.66$  m and  $L_{\max} = 1.09$  m. Substituting the damped natural frequencies corresponding to  $L_{\min}$  and  $L_{\max}$  into equation (4.6.1) we can find the start and end value  $a_k$  of the dilation parameter and choosing an appropriate step size  $\Delta a$ . Each of this dilation parameter is translated over the entire time domain by  $b$  parameter. Below is the setup of  $a_k$  for each vibratory mode.

- Mode 1:  $a_1 = 100 : 1 : 560$
- Mode 2:  $a_2 = 22 : 0.5 : 90$
- Mode 3:  $a_3 = 7 : 0.1 : 38$

First, considering the beam extension scenario, Figure 4.10 shows the results obtained from the WT of each vibration signal, in order to show the first three modes the dilation parameter range is chosen as  $a_{all} = 7 : 1 : 560$ . It is observed that two ridges are visible and

they correspond to the 1<sup>st</sup> and 2<sup>nd</sup> vibratory modes. For the third mode the ridge is very small compared to the first two modes and it can be observed in the wavelet transform of TAC vibration signal. In contrast, during the beam retraction scenario, the ridge of the third mode is very dominant compared to the other two modes and it can be seen in Figure 4.11 especially in the MAC and TAC's wavelet transforms. It should also be noted that during the beam retraction, the vibration observed at MAC and TAC locations also contain the fourth mode and it is due to the fact that it is easier to excite higher mode when the beam is retracting; it is shown in Figure 4.11.

As shown in Figure 4.10 and Figure 4.11, the ridge represents the maximum signal energy. To find the frequency at which the ridge occurs, the dilation parameter  $a_m$  corresponding to a ridge is found by the following condition

$$|W(a_m, b)| > |W(a_k, b)| \quad (4.6.2)$$

By tracking the dilation parameter at which the maximum value of  $|W(a, b)|$  occurs over time we can find the IF using equation (4.6.1). In both of the scenarios, it is important to select a vibration signal that contains information from all three vibratory modes. Therefore, we choose the TAC vibration signal. Figure 4.12 and Figure 4.13 show the contour plots of the wavelet transform for both the scenarios. These figures also compare the IFs identified using the condition of equation (4.6.2) and the IFs computed using equation (4.4.1). Based on these figures, some observation can be drawn:

*Beam Extension Scenario:*

1. For the first mode, the identified IF follows the frozen IF well.
2. For the second mode, the identified IF follows the frozen IF satisfactorily with some fluctuations. The fluctuation is due to searching for maximum value of  $|W(a_k, b)|$  at each time instant. Therefore, during the search process the other modes might have higher  $|W(a_k, b)|$  value than the targeted mode; hence at some instant the identified IF would jump to the other value.
3. For the third mode, the identified IF follows the frozen IF somewhat with a significant fluctuation.

*Beam Retraction Scenario:*

1. For the first mode, the identified IF follows the frozen IF well.
2. For the second mode, the identified IF follows the frozen IF well in the first 6 seconds, but in the beginning and after 6 seconds there are lots of jumps.
3. For the third mode, the identified IF follows the frozen IF well at some intervals but fluctuation happens at others.

Table 4.1: Comparison between the IFs based on equation (4.3.1) and IFs based on equation (4.4.1)

$\omega_{di}$ (Hz)	Analytic frozen IFs based on equation (4.3.1)		Experimental frozen IFs based on equation (4.4.1)	
	$L_{\min} = 0.66$ (m)	$L_{\max} = 1.09$ (m)	$L_{\min} = 0.66$ (m)	$L_{\max} = 1.09$ (m)
$\omega_{d1}$	2.184	5.958	1.948	4.941
$\omega_{d2}$	13.690	37.339	12.370	31.548
$\omega_{d3}$	38.332	104.553	34.979	88.547

It should be noted that the experimental IFs are lower than the analytical ones. This discrepancy may be attributed to the fact that the guiding slot fails to emulate an ideal clamped end since there is a clearance needed between the beam and the guiding slot (Deng, 2002).

**Beam Extension**

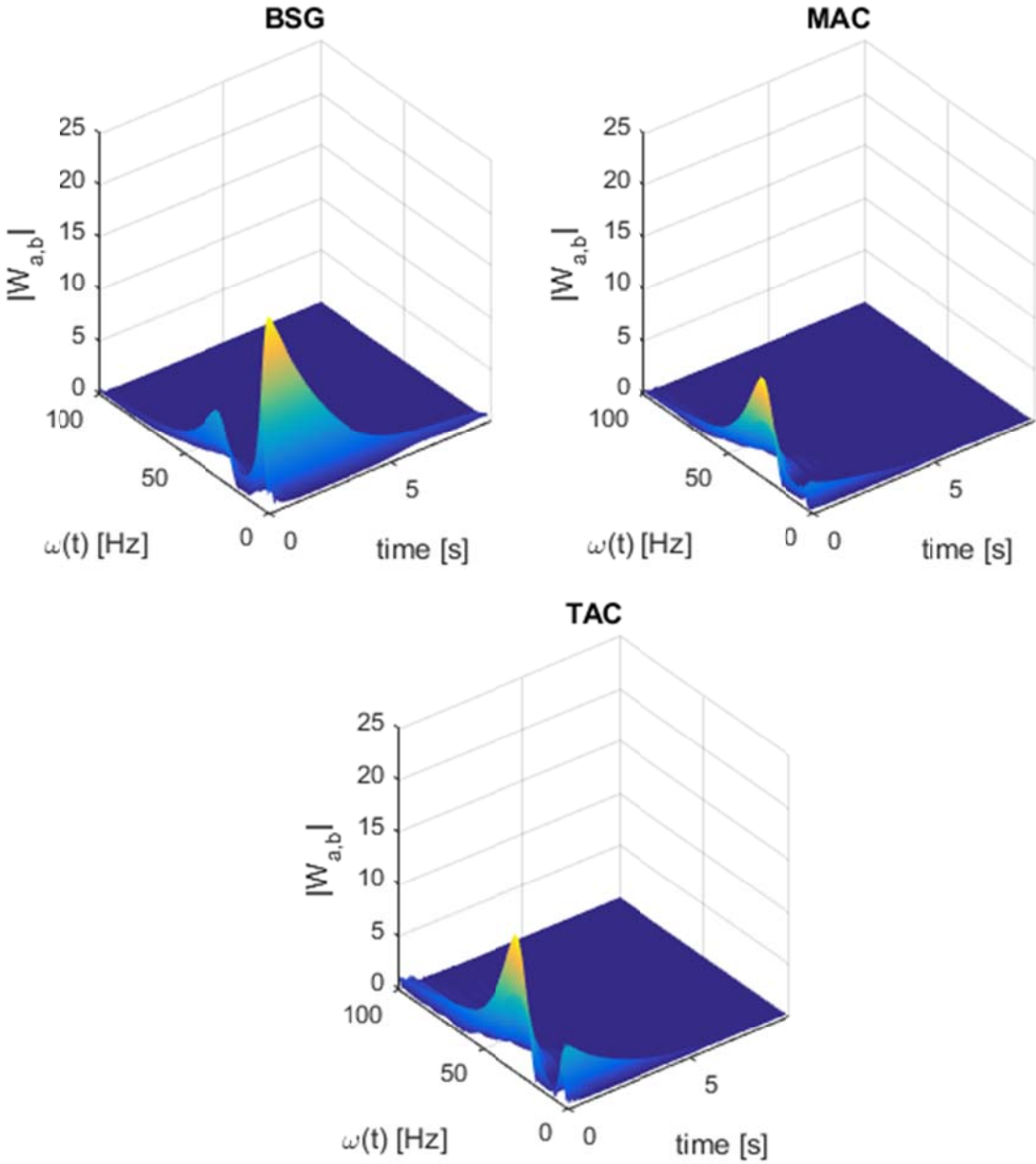


Figure 4.10: Beam extension: The Wavelet transform of all three vibration signals

### Beam Retraction

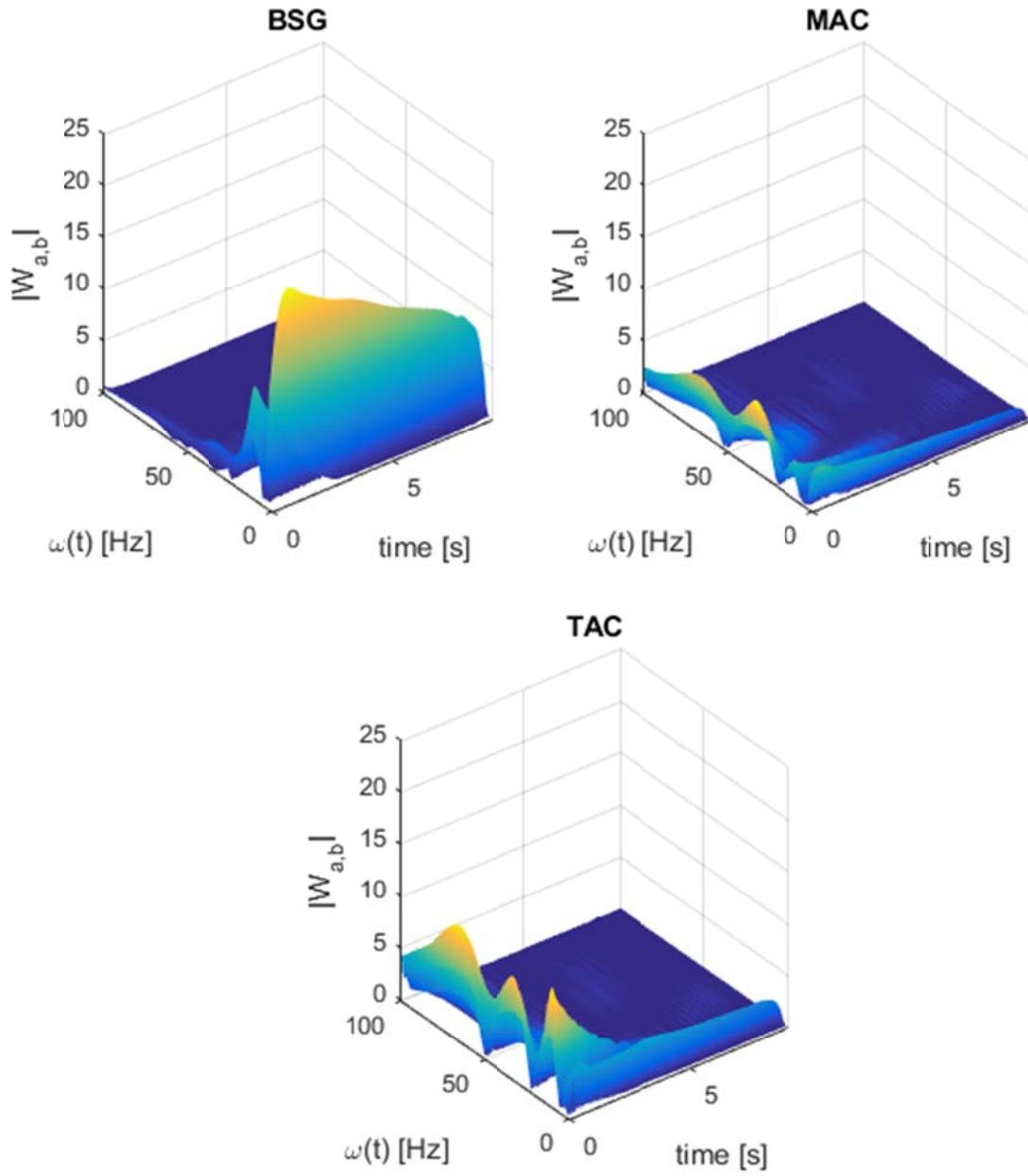


Figure 4.11: Beam retraction: The Wavelet transform of all three vibration signals

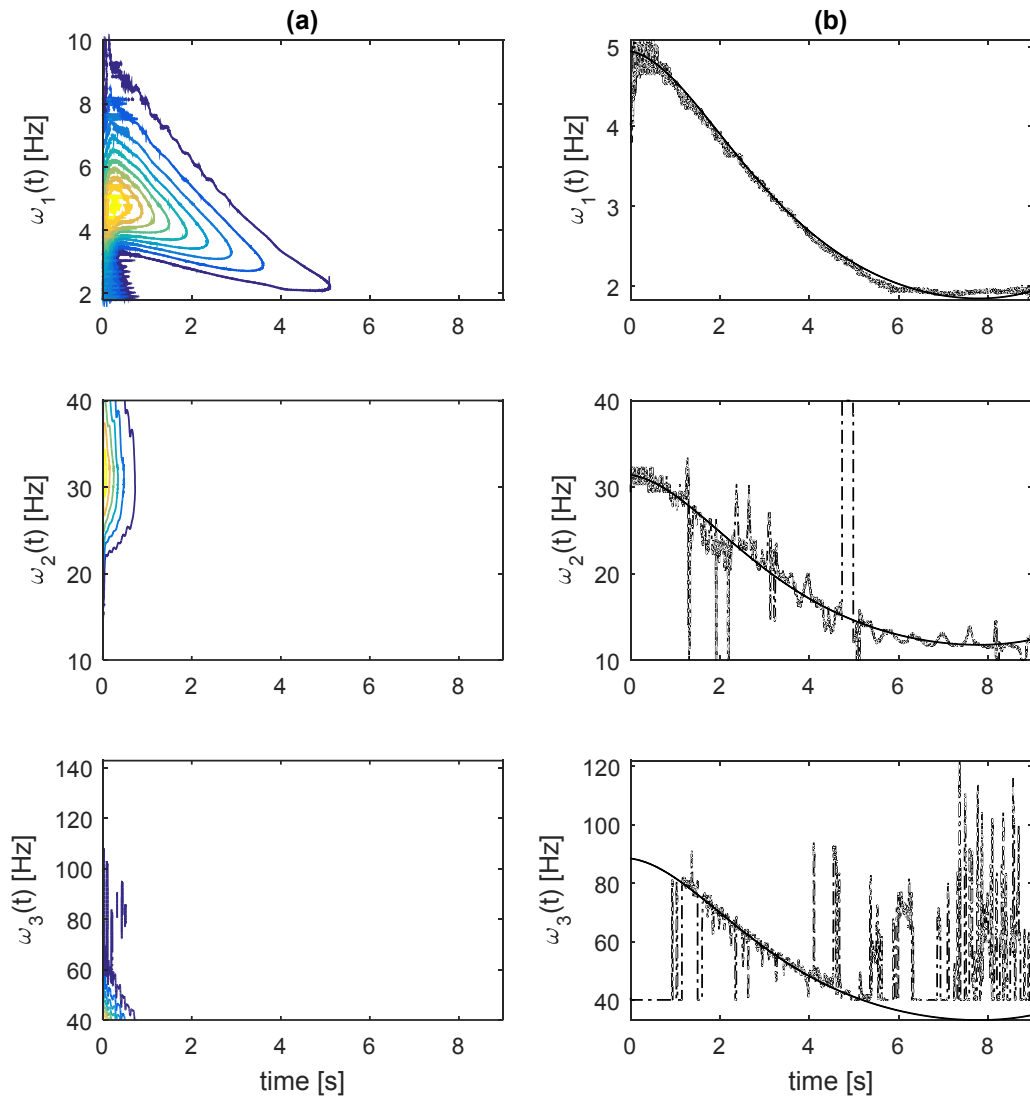


Figure 4.12: Beam extension: (a) Contour plot of  $|W(a,b)|$  of TAC vibration signal (a) and (b) estimated IF from ridges of WT (dash-dot line) and frozen IF (solid)

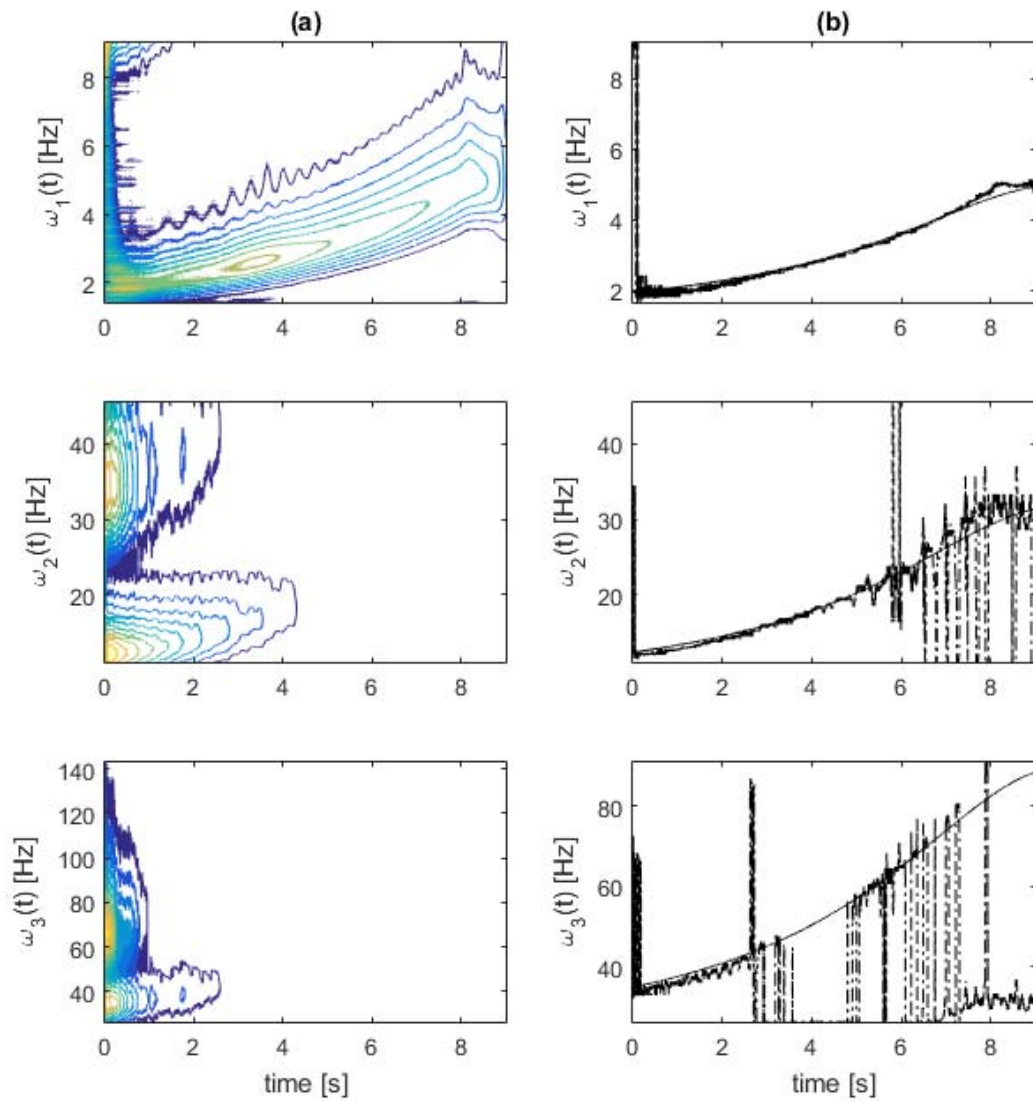


Figure 4.13: Beam retraction: (a) Contour plot of  $|W(a,b)|$  of TAC vibration signal (a) and (b) estimated IF from ridges of WT (dash-dot line) and frozen IF (solid)

## 4.7 The Hilbert Vibration Decomposition (HVD)

In this section a recently developed technique called Hilbert vibration decomposition (HVD) is introduced. The HVD method is developed by Feldman, (2006) for decomposition of the multicomponent nonstationary signal. Many other researchers also used this method on their respective time variant signals (Ramos et al., 2014; Wang, 2011; Bertha & Golival, 2014).

A representation of a nonstationary signal with multicomponent would have such form

$$x(t) = \sum_k A_k(t) \cos\left(\int \omega_k(t) dt\right) \quad (4.7.1)$$

where,  $A_k(t)$  and  $\omega_k(t)$  are the instantaneous amplitude (IA) and instantaneous frequency (IF) of the  $k^{th}$  component, respectively and these parameters are considered as slow-varying. Each mono-component  $A_k(t) \cos\left(\int \omega_k(t) dt\right)$  is an intrinsic mode of the original signal with wideband spectrum.

### 4.7.1 Instantaneous Frequency (IF) of the Largest Energy Component

In order to get the IF, a quadrature signal  $x_H(t)$  needs to be formed based on using the Hilbert Transform (HT). The HT of original signal can be obtained from equation (4.7.2). Adding the original signal  $x(t)$  with its counterpart “quadrature”  $x_H(t)$ , the analytic signal  $z(t)$  could be formed as below

$$x_H(t) = \frac{1}{\pi} \int_{-\infty}^{\infty} \frac{x(\tau)}{t - \tau} d\tau \quad (4.7.2)$$

$$z(t) = x(t) + x_H(t) = A(t)e^{i\phi(t)} \quad (4.7.3)$$

From above equation the instantaneous amplitude  $A(t)$  and instantaneous phase  $\phi(t)$  are obtain as follows,

$$\begin{aligned} A(t) &= \sqrt{x^2(t) + x_H^2} \\ \phi(t) &= \arctan\left(\frac{x_H(t)}{x(t)}\right) \end{aligned} \quad (4.7.4)$$

Thus taking the derivative of the instantaneous phase with respect to time would give instantaneous frequency,

$$\omega(t) = \frac{d}{dt}\phi(t) = \frac{x(t)\dot{x}_H(t) - \dot{x}(t)x_H(t)}{x^2(t) + x_H^2(t)} \quad (4.7.5)$$

In order to understand how the HVD extracts the instantaneous frequency of the largest energy component, a symbolic example is used. Suppose the original signal  $x(t)$  is composed of two components, both with modulated amplitude and frequency. Considering  $A_1(t) > A_2(t)$  and  $\omega_1(t) > \omega_2(t)$  which implies that  $A_1(t)\cos\left(\int \omega_1(t)dt\right)$  has the largest energy. Thus the original signal with its analytic representation is given below

$$\begin{aligned} x(t) &= A_1(t)\cos\left(\int \omega_1(t)dt\right) + A_2(t)\cos\left(\int \omega_2(t)dt\right) \\ z(t) &= A_1(t)e^{i\int_0^t \omega_1(t)dt} + A_2(t)e^{i\int_0^t \omega_2(t)dt} \end{aligned} \quad (4.7.6)$$

By using equation (4.7.4) and equation(4.7.5), the instantaneous parameters of  $x(t)$  are

$$A(t) = \sqrt{A_1^2(t) + A_2^2(t) + 2A_1(t)A_2(t)\cos\left(\int_0^t [\omega_2(t) - \omega_1(t)]dt\right)} \quad (4.7.7)$$

$$\omega(t) = \omega_1(t) + \frac{[\omega_2(t) - \omega_1(t)] \left[ A_2^2(t) + 2A_1(t)A_2(t) \cos\left(\int_0^t [\omega_2(t) - \omega_1(t)] dt\right) \right]}{A^2(t)} + \frac{[A_1(t)A_2'(t) - A_1'(t)A_2(t)] \sin\left(\int_0^t [\omega_2(t) - \omega_1(t)] dt\right)}{A^2(t)} \quad (4.7.8)$$

The instantaneous amplitude  $A(t)$  consists of the sum of the squared individual component amplitudes, and a rapidly varying oscillating part. The instantaneous frequency  $\omega(t)$  consists of a slowly varying part  $\omega_1(t)$  and two rapidly varying asymmetrical oscillating parts. The third term of the instantaneous frequency is negligible, because the time derivatives of  $A_1(t)$  and  $A_2(t)$  are very small. It follows that in order to make  $\omega(t) = \omega_1(t)$  the second term must be equal to zero. This is obtained by integrating the rapid oscillatory term over the period of the difference frequency  $T = \frac{2\pi}{\omega_2 - \omega_1}$  (Feldman, 2006; 2011).

$$\int_0^T \left( \frac{[\omega_2(t) - \omega_1(t)] \left[ A_2^2(t) + 2A_1(t)A_2(t) \cos\left(\int_0^t [\omega_2(t) - \omega_1(t)] dt\right) \right]}{A^2(t)} + \frac{[A_1(t)A_2'(t) - A_1'(t)A_2(t)] \sin\left(\int_0^t [\omega_2(t) - \omega_1(t)] dt\right)}{A^2(t)} \right) dt = 0 \quad (4.7.9)$$

In implementation, a low-pass filter is used to get rid of the second term and leave only the frequency  $\omega_1(t)$ . If there are more than two components present in the original signal, the IF would have a complicated form but again the low-pass filtering will extract the

only IF of the largest energy component. The next step of the HVD method is to extract the envelope of the large energy component and it is described in the following section.

#### 4.7.2 Envelope of the Largest Energy Component

Once the instantaneous frequency of the largest energy component is found, the envelope can be readily estimated by the synchronous demodulation technique (Ramos et al., 2014). Let  $x(t)$  be a sum of  $k$  components with instantaneous phase  $\theta_k(t)$ ,

$$x(t) = \sum_{k=1}^N A_k(t) \cos\left(\int \omega_k(t) dt + \theta_k\right) \quad (4.7.10)$$

$$x_H(t) = \sum_{k=1}^N A_k(t) \sin\left(\int \omega_k(t) dt + \theta_k\right) \quad (4.7.11)$$

where,  $x_H(t)$  is obtained with the Hilbert transform. The synchronous demodulation technique is based on using two reference signals that are exactly  $90^\circ$  out of phase with a known frequency. Multiplying these reference signals with the initial signal and its quadrature counterpart one could extract the largest energy component corresponding to that known frequency. For convenience, the two reference signals are selected as  $\cos\left(\int \omega_1(t) dt\right)$  and  $\sin\left(\int \omega_1(t) dt\right)$ .

$$\begin{aligned} x_{\cos}(t) &= x(t) \cos\left(\int \omega_1(t) dt\right) \\ x_{\sin}(t) &= x(t) \sin\left(\int \omega_1(t) dt\right) \\ x_{H\cos}(t) &= x_H(t) \cos\left(\int \omega_1(t) dt\right) \\ x_{H\sin}(t) &= x_H(t) \sin\left(\int \omega_1(t) dt\right) \end{aligned} \quad (4.7.12)$$

Then the signal in phase  $y_{\cos}(t)$  and quadrature  $y_{\sin}(t)$  are obtained using equation (4.7.10), equation (4.7.11) and equation (4.7.12),

$$\begin{aligned}
y_{\cos}(t) &= x_{\cos}(t) + x_{H \sin}(t) \\
&= \underbrace{A_1(t) \cos(\theta_1)}_{\bar{y}_{\cos}(t)} + \sum_{k=2}^N A_k(t) \cos\left(\int \omega_k(t) dt - \int \omega_1(t) dt + \theta_k\right)
\end{aligned} \tag{4.7.13}$$

$$\begin{aligned}
y_{\sin}(t) &= x_{H \cos}(t) - x_{\sin}(t) \\
&= \underbrace{A_1(t) \sin(\theta_1)}_{\bar{y}_{\sin}(t)} + \sum_{k=2}^N A_k(t) \sin\left(\int \omega_k(t) dt - \int \omega_1(t) dt + \theta_k\right)
\end{aligned} \tag{4.7.14}$$

Let  $\bar{y}_{\cos}(t)$  and  $\bar{y}_{\sin}(t)$  be the obtained signals after above equations are passed through a low-pass filter. The analytic signal  $\bar{y}(t) = A_1(t) \cos(\theta_1) + jA_1(t) \sin(\theta_1)$  can be formed and the largest energy component is obtain as below,

$$A_1(t) = \sqrt{\left(\bar{y}_{\cos}(t)\right)^2 + \left(\bar{y}_{\sin}(t)\right)^2} \tag{4.7.15}$$

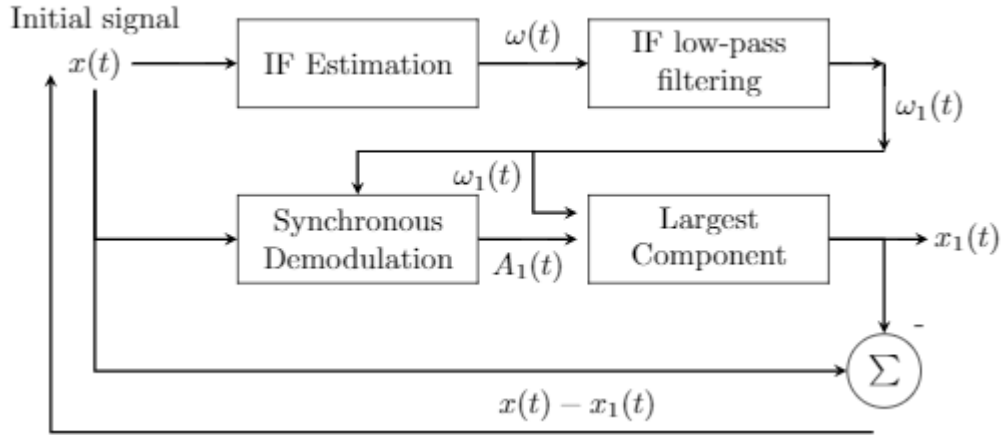


Figure 4.14: Block diagram of the HVD algorithm (Feldman, 2011)

Once  $A_1(t)$  and  $\omega_1(t)$  are found, they are put together in  $x_1(t) = A_1(t) \cos\left(\int \omega_1(t) dt\right)$  which has cosine base. Consequently all components get decompose by the HVD method. The detail of the HVD method is now illustrated using the flowchart as shown in Figure 4.14. Starting the first iteration, the vibration signal or initial signal  $x(t)$  is processed through HT in order to estimate the average IF  $\omega(t)$ , and then the average IF gets smooth by a low-pass filter to minimize high fluctuation resulting in a dominant IF  $\omega_1(t)$ . After that, the synchronous demodulation technique is applied using  $\omega_1(t)$  and  $x(t)$  to estimate the envelope of the largest energy component  $A_1(t)$ . Furthermore, the first component  $x_1(t)$  is produced using  $\omega_1(t)$ , and  $A_1(t)$ . Then  $x_1(t)$  is subtracted from  $x(t)$ , the whole process starts over for the next iteration using the remaining  $x(t)$  to be decomposed.

#### **4.8 Identification of the Instantaneous Frequencies of the Axially-Moving Beam Using the HVD method**

To evaluate the performance of the HVD method, again two motion scenarios are considered; beam extension and beam retraction. For the vibratory mode decomposition only the data obtained at the base location (from BSG sensor) and the tip location (from TAC sensor) is considered for both the scenarios. The vibration signal from middle location (MAC sensor) does not have rich modal information compared to tip location. Before applying the HVD method two parameters are need to set; the cut-off frequency of the low-pass filter and number of components need to extract. According to (Feldman, 2006) the cut-off frequency value for the low-pass filter should be as small as possible but not smaller than the frequency of the lowest component. Choosing a large value for the cut-off frequency decrease the IF resolution and choosing a small value will increase the IF resolution but at the cost of time resolution. It should be also noted that the difference between close frequencies should be

more than the cut-off frequency value, otherwise the IF result would fluctuate between the respective close frequencies of each component.

In beam extension scenario; the response obtained from the BSG sensor was processed by the HVD method to decompose the three vibratory modes. Figure 4.15 shows the three decomposed components with their respective envelopes and the IFs. It can be observed that after 1 second the contribution from the second and third modes is negligible. There are two reasons for it. First, it is difficult to excite the higher modes of the beam when the initial beam length is small. Second, as the length of the beam changes from  $L_{\min}$  to  $L_{\max}$  the stiffness decreases and the mass increases, this also greatly affects the energy of the higher modes. Furthermore, it can be seen that the first mode is extracted satisfactorily and the IF of the first mode fluctuates around the frozen IF. The second mode is extracted properly in the beginning for one second and after that higher fluctuation happens because of no energy in the second mode and the same thing holds for the third mode. Next, the TAC vibration signal is used. It contains rich dynamical response, because the displacement at the free end of the beam is larger; hence the contribution from the higher modes is more desirable. By examining Figure 4.16, the first modal response between 0 to 1 seconds contains information of the second mode. In the second and third modal responses same modal mixing issue exists. This incorrect decomposition issue can be explained by closely examining equation (4.7.8).

Equation (4.7.8) can be rewritten in the general form as given below. A new parameter is introduced as  $\alpha = \frac{A_1(t)}{A_2(t)}$  to show the time varying ratio of the two instantaneous amplitudes.

$$\begin{aligned}
\omega(t) &= \frac{A_1^2\omega_1 + A_2^2\omega_2 + (\omega_2 + \omega_1)A_1A_2 \cos\left(\int(\omega_2 - \omega_1)dt\right) + (A_1A_2' - A_1'A_2) \sin\left(\int(\omega_2 - \omega_1)dt\right)}{A_1^2 + A_2^2 + 2A_1A_2 \cos\left(\int(\omega_2 - \omega_1)dt\right)} \\
&= \frac{\alpha\omega_1 + \frac{1}{\alpha}\omega_2 + (\omega_2 + \omega_1) \cos\left(\int(\omega_2 - \omega_1)dt\right) - \frac{\alpha'}{\alpha} \sin\left(\int(\omega_2 - \omega_1)dt\right)}{\alpha + \frac{1}{\alpha} + 2 \cos\left(\int(\omega_2 - \omega_1)dt\right)}
\end{aligned} \tag{4.8.1}$$

where,  $\alpha' = (A_1'A_2 - A_1A_2') / A_2^2$  is the time derivative of the time-varying ratio of the two instantaneous amplitudes. The above equation of the average IF could further simplified by letting  $\beta = \alpha + \frac{1}{\alpha} + 2 \cos\left(\int(\omega_2 - \omega_1)dt\right)$ . The simplified version of average IF is shown below,

$$\omega(t) = \underbrace{\frac{\alpha}{\beta}\omega_1}_1 + \underbrace{\frac{1}{\alpha\beta}\omega_2}_2 + \underbrace{\frac{(\omega_2 + \omega_1)}{\beta} \cos\left(\int(\omega_2 - \omega_1)dt\right)}_3 - \underbrace{\frac{\alpha'}{\alpha\beta} \sin\left(\int(\omega_2 - \omega_1)dt\right)}_4 \tag{4.8.2}$$

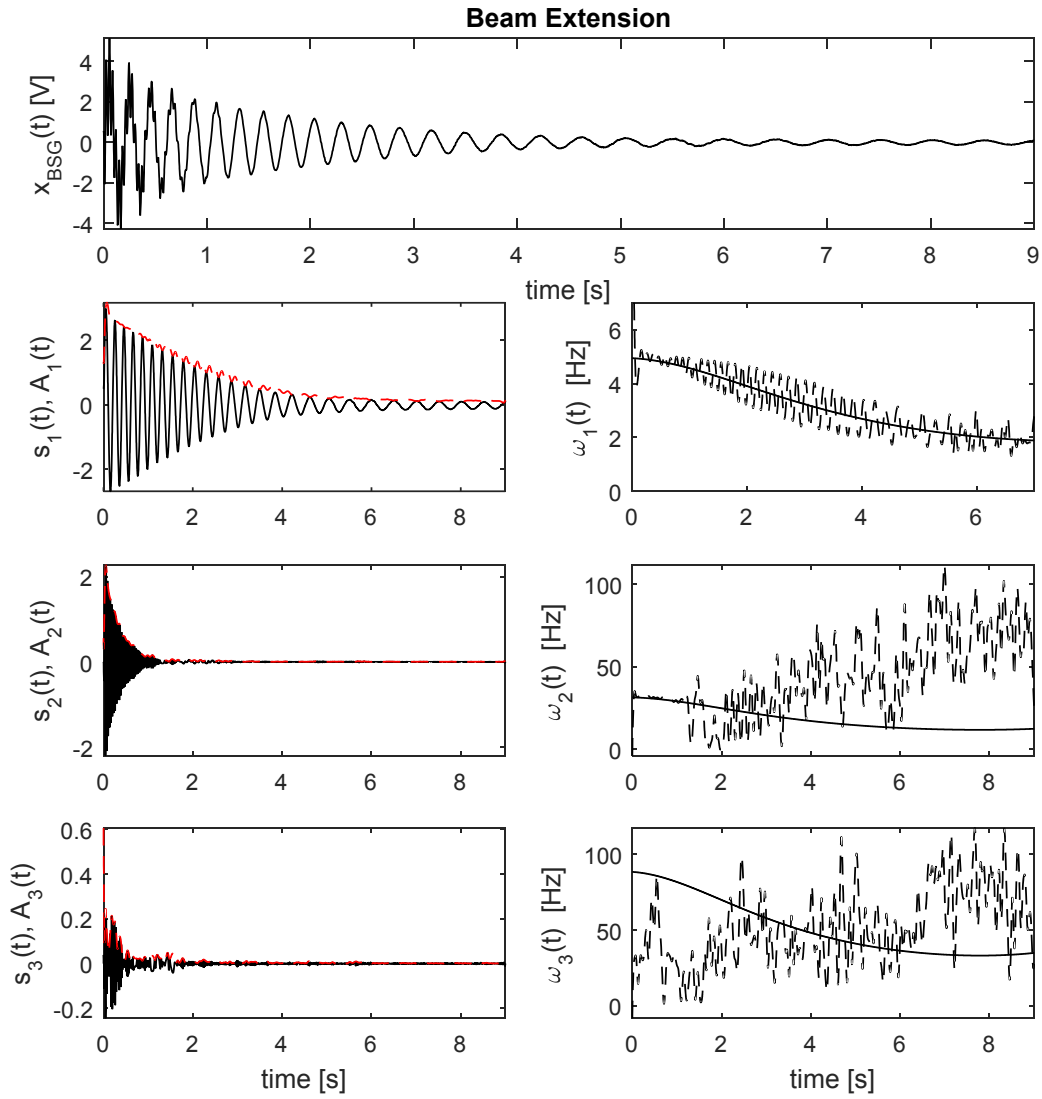


Figure 4.15: Beam extension: BSG vibration signal with the corresponding decomposed components obtained from the HVD method. The identified IFs (dash-dot) are compared with the frozen IFs (solid)

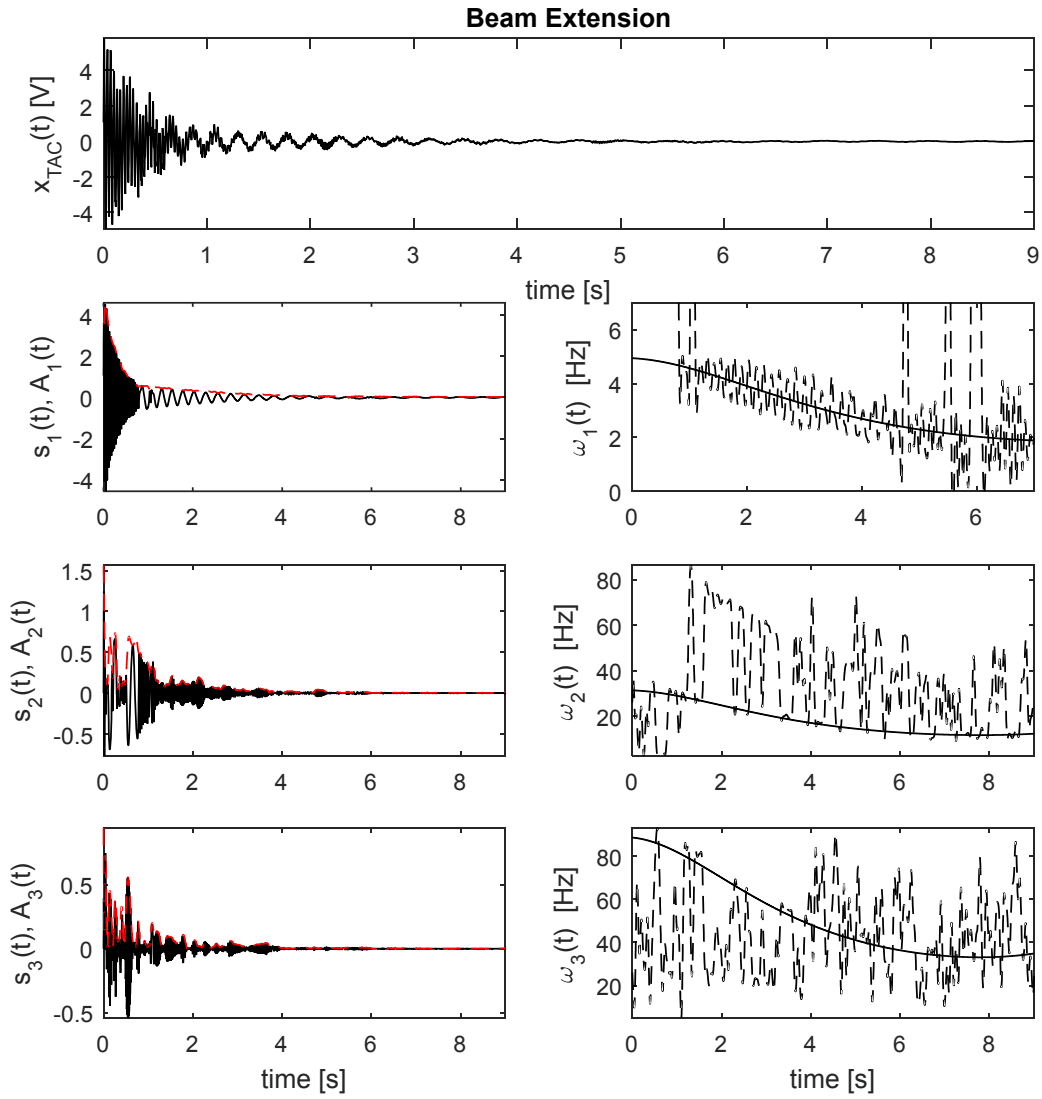


Figure 4.16: Beam extension: TAC vibration signal with the corresponding decomposed components obtained from the HVD method. The identified IFs (dash-dot) are compared with the frozen IFs (solid)

From equation (4.8.2), it is clear that the average IF is dependent on  $\alpha$  (Ramos et al., 2014), so for better understanding the following cases are considered to analyze both scenarios and stating the obvious that the IF of the 1<sup>st</sup> mode is smaller than the IF of the 2<sup>nd</sup> mode.

*Cases for identifying the average IF  $\omega(t)$*

1.  $\alpha \gg 1$  and  $\omega_1(t) < \omega_2(t)$ ; the average IF  $\omega(t)$  fluctuates around  $\omega_1(t)$
2.  $\alpha > 1$  and  $\omega_1(t) < \omega_2(t)$ ; the average IF  $\omega(t)$  fluctuates between  $\omega_1(t)$  and  $\omega_2(t)$
3.  $\alpha \approx 1$  and  $\omega_1(t) < \omega_2(t)$ ; the average IF  $\omega(t)$  fluctuates around  $\omega_2(t)$
4.  $\alpha < 1$  and  $\omega_1(t) < \omega_2(t)$ ; the average IF  $\omega(t)$  fluctuates around  $\omega_2(t)$

In the above analyses a vibration signal composed of two components is considered, but generalizing it to three or more vibration components, the average IF in equation (4.8.2) would have much more complicated form and so as the cases. These cases give an in-depth understanding of how the HVD estimates the IF from a vibration signal. It should be noted that the HVD method estimates the average IF before extracting the corresponding modal responses. Thus, the observations of the results of the HVD method using four vibration signals; two from each scenario are as follows,

*Beam Extension Scenario:*

Figure 4.15 shows the HVD results using the BSG signal.

**1<sup>st</sup> Mode:** The HVD is able to extract the modal response of the 1<sup>st</sup> mode well. The identified IF fluctuates about the corresponding frozen IF.

**2<sup>nd</sup> Mode:** The HVD is able to extract the modal response of the 2<sup>nd</sup> mode from 0 to 1 second. During this interval, the identified IF follows the corresponding frozen IF well. However, after that the identified IF is not sensible due to weak information about the 2<sup>nd</sup> mode.

**3<sup>rd</sup> Mode:** The extracted modal response of the 3<sup>rd</sup> mode is unsatisfactory.

*Beam Extension Scenario:*

Figure 4.16 shows the HVD results using the TAC signal.

**1<sup>st</sup> Mode:** The HVD is able to extract the 1<sup>st</sup> modal response from 1 to 9 second. During this interval, the identified IF follows the corresponding frozen IF well. However from 0 to 1 second, the extracted modal response contains information of the higher modes.

**2<sup>nd</sup> Mode:** The HVD extracts the 2<sup>nd</sup> modal response unsatisfactorily. Also it can be observe from the corresponding identified IF that the extracted modal response is somewhat contaminated by the 3<sup>rd</sup> mode.

**3<sup>rd</sup> Mode:** The extracted modal response of the 3<sup>rd</sup> mode is unsatisfactory.

*Beam Retraction Scenario:*

Figure 4.17 shows the HVD results using the BSG signal.

**1<sup>st</sup> Mode:** The HVD is able to extract the 1<sup>st</sup> modal response from 1 to 9 seconds. During this interval, the identified IF fluctuates about the corresponding frozen IF.

**2<sup>nd</sup> Mode:** The HVD is able to extract the 2<sup>nd</sup> modal response from 1 to 5 seconds. During this interval, the identified IF follows the corresponding frozen IF well. However, after that the identified IF is not sensible due to weak information about the 2<sup>nd</sup> mode.

**3<sup>rd</sup> Mode:** The HVD is able to extract the 3<sup>rd</sup> modal response from 1 to 5 seconds. During this interval, the identified IF follows the corresponding frozen IF well. However, after that the identified IF is not sensible due to weak information about the 3<sup>rd</sup> mode.

*Beam Retraction Scenario:*

Figure 4.18 shows the HVD results using the TAC signal.

**1<sup>st</sup> Mode:** The HVD is able to extract the 1<sup>st</sup> modal response from 4 to 9 seconds. During this interval, the identified IF fluctuates about the corresponding frozen IF. During 0 to 4 seconds, the HVD extracts the higher modes due to their energy level being higher than the 1<sup>st</sup> mode.

**2<sup>nd</sup> Mode:** The HVD extracts the 2<sup>nd</sup> modal response unsatisfactorily except from 4 to 5 seconds. During this interval, the identified IF follows the corresponding frozen IF well.

**3<sup>rd</sup> Mode:** The HVD extracts the 3<sup>rd</sup> modal response from 4 to 5 seconds. However, during other time instant the decomposition is unsatisfactory.

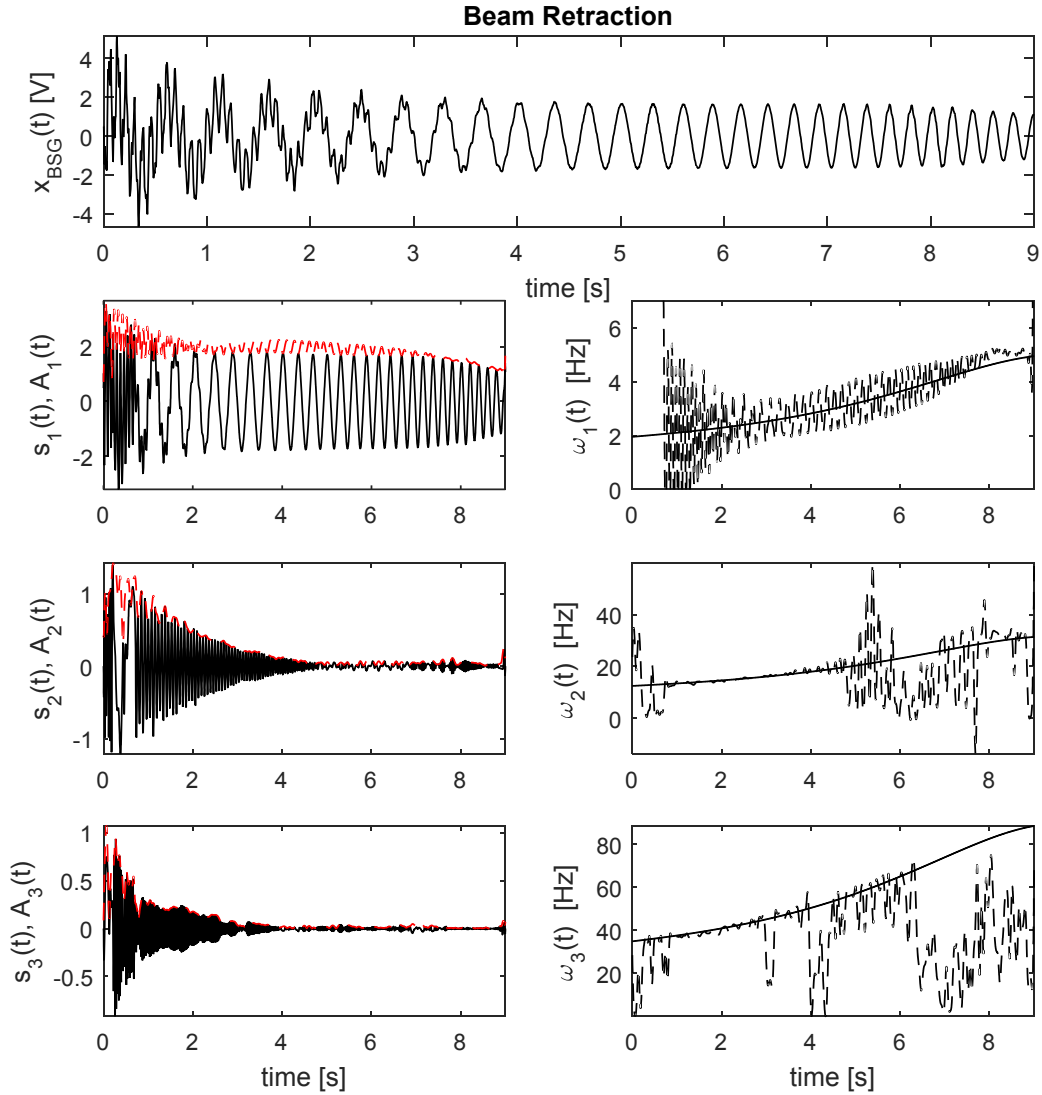


Figure 4.17: Beam retraction: BSG vibration signal with the corresponding decomposed components obtained from the HVD method. The identified IFs (dash-dot) are compared with the frozen IFs (solid).

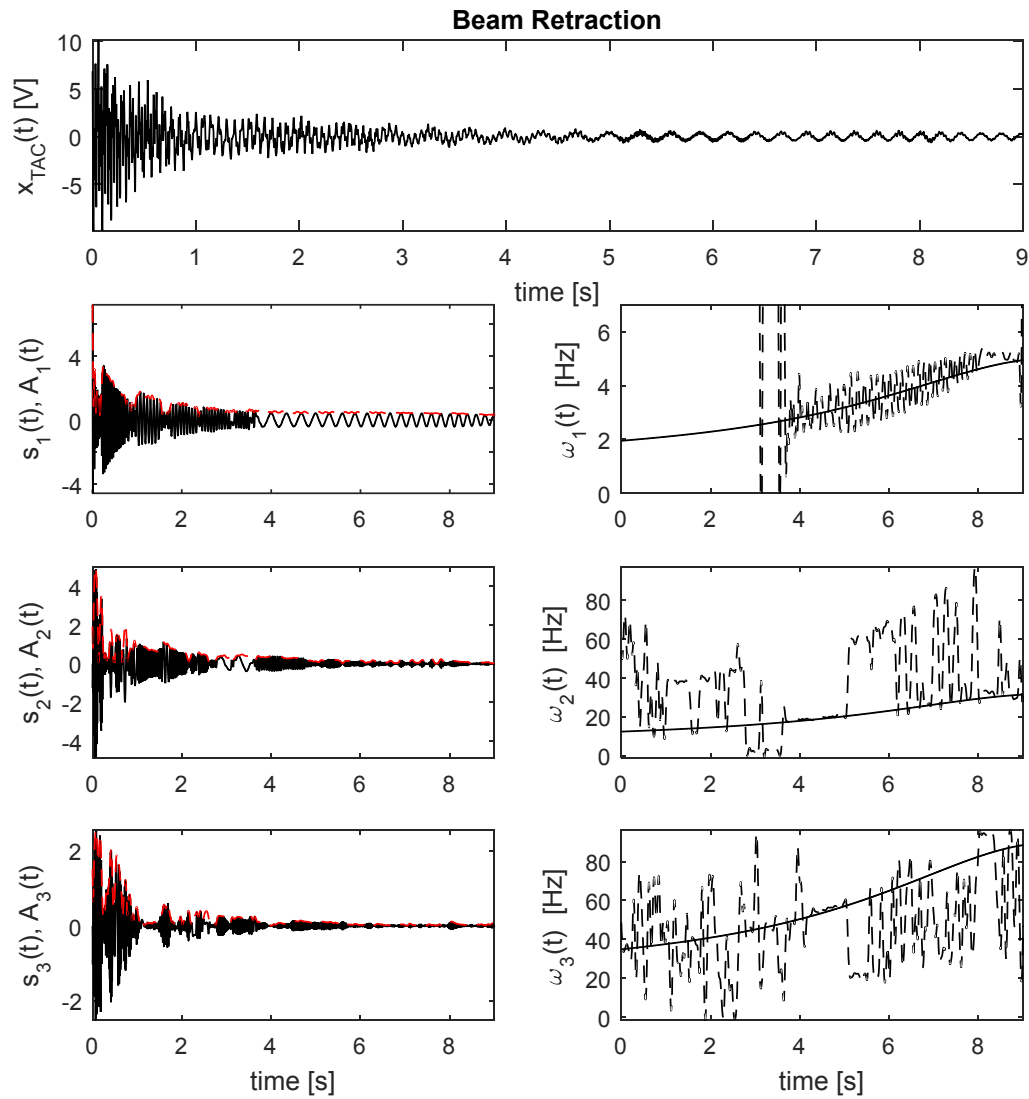


Figure 4.18: Beam retraction: TAC vibration signal with the corresponding decomposed components obtained from the HVD method. The identified IFs (dash-dot) are compared with the frozen IFs (solid)

It is important to note that in order for the HVD to work satisfactorily the amplitude of the multi-component nonstationary signal should vary slowly because the average IF depends also on the time derivative of the amplitude; which is represented by the 3<sup>rd</sup> term in equation (4.7.8). The contribution from this term affects the average IF even after the filtering process. Figure 4.15 to Figure 4.18 also show the envelope of all the decomposed components of the initial signals (in red). The envelopes of these components are all mixed together. Practically it means that the decomposed components are piecewise function of the initial signal. The HVD method decomposes the first mode satisfactorily from all four signals presented. This is because in all four vibration signals the first mode is mainly dominant. Even though, the identification of the first IF follows closely the corresponding frozen IF, the frequency resolution is still very low. This is one of the limitations of the HVD method as it is stated in (Feldman, 2006; 2011).

#### **4.9 Identification of the Instantaneous Frequencies of the Axially-moving Beam Using the HVD Method plus the TVAR Modelling**

The accuracy of the first identified IF could further be improved by employing the TVAR method with model order  $p = 2$  to estimate the IF of decomposed first modal response  $s_1(t)$  obtained from the HVD method. Using the time-varying coefficients  $a_i(t)$  of the TVAR method, we can estimate the IF. The TVAR method gives freedom to predict the variance of the measurement noise  $\sigma_v^2$  in the initial signal and the variance of the process noise  $\sigma_w^2$  in the time-varying parameters of the initial signal. As a result, the accuracy is further improved as it is illustrated in Figure 4.19 and Figure 4.20. Further observation can be made by dividing the identified IF obtained from the HVD method and the HVD plus TVAR method into three intervals. The observations are the same for both of the scenarios and they are stated below,

*0 to 1 second interval:*

In this interval, we observe the end effects from the HVD method and also from the HVD plus TVAR method. In the HVD method the end effects come from the incomplete periodicity at the beginning of  $s_1(t)$ . And in the HVD plus TVAR method the end effects come from the Kalman filter. The identified IF resolution is almost the same for these two methods. It should be noted that in Figure 4.20 the identified IF obtained from the HVD plus TVAR method is not following the corresponding frozen IF. This is due to the fact that we used the decomposed first modal responses obtained from the HVD method.

*1 to 8 second interval:*

During this interval, the identified IF obtained by the HVD plus TVAR method follows well the corresponding frozen IF compared with the identified IF from the HVD method.

*8 to 9 second interval:*

During this interval, the end effects occur again because of the aforementioned issue present in both of these methods.

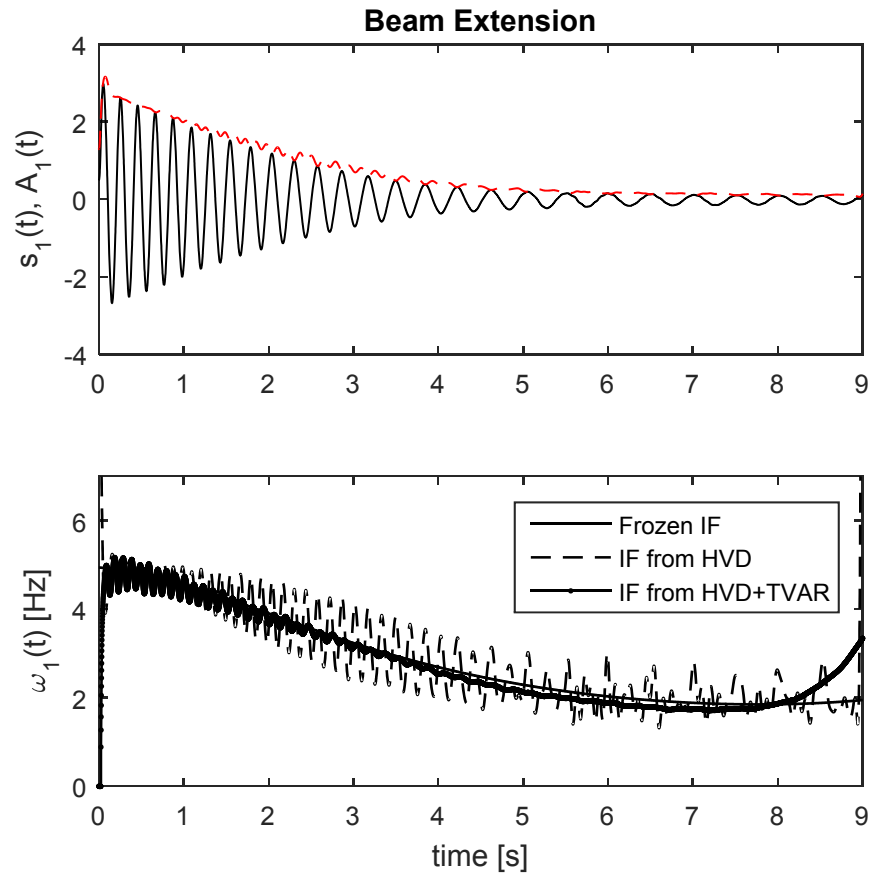


Figure 4.19: Beam extension: Comparisons between the IF obtained from the HVD method, the IF obtained the HVD plus TVAR method with the corresponding frozen IF.

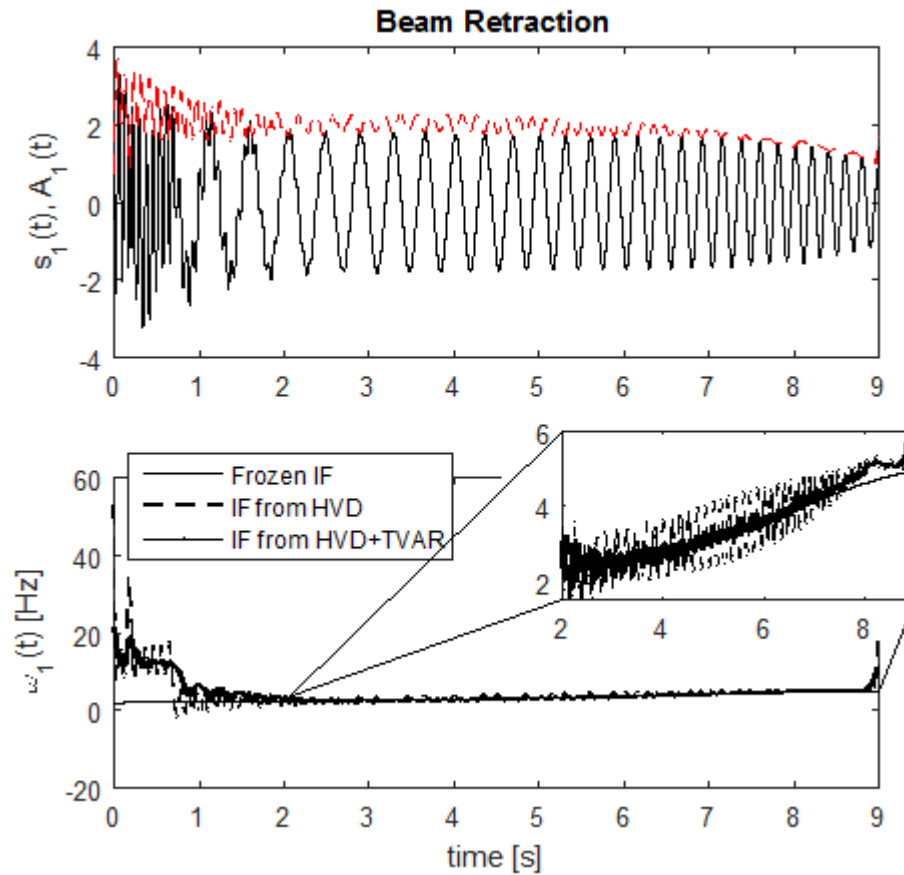


Figure 4.20: Beam retraction: Comparisons between the IF obtained from the HVD method, the IF obtained the HVD plus TVAR method with the corresponding frozen IF.

#### 4.10 Summary

Based on the results presented in this chapter, the following conclusions can be drawn:

1. The proposed method fails to identify the IFs because the vibration signals are not only amplitude modulated but also frequency modulated.

2. A better ridge tracking algorithm could be employed to identify the IF of all the vibratory mode as presented in (Liu, 2007)
3. The WT could perform better in tracking the IF, if the modal decomposition is achieved first. This could be done by utilizing Wavelet Packet Transform (WPT) (Sadhu, 2013).
4. The HVD would perform better if the energy of all vibratory mode decay slowly also considering that the vibration signal is contaminated with high SNR.
5. A better frequency resolution could be achieved if the HVD method is integrated with TVAR modelling for IF identification.

# Chapter 5

## Conclusions and Future Works

### 5.1 Conclusions

A novel damage detection technique is proposed using the blind source separation (BSS) method integrated with the time-varying auto-regressive (TVAR) modeling. The second-order blind identification (SOBI) is employed first to decompose the mono-harmonic responses from the vibration data where each of the undamaged natural frequencies has an abrupt change (i.e., mode-mixing). Then the TVAR modeling is utilized to track the damage instant and detect the severity of frequency changes. In this way, the limitation of the SOBI method is overcome with the TVAR modeling and frequencies of both the states are delineated. Moreover, since each of the modal responses resulting from the SOBI contains single frequency, a low model order of the TVAR modeling is sufficient enough to capture the dynamics of the modal responses. Therefore, the complexity in selecting an appropriate model order of the time-series model is avoided.

The proposed algorithm is employed to identify both discrete and progressive damages based on the output-only measurements. In the case of discrete damage, a numerical 5-DOF system and two experimental 3-DOF systems are studied. In addition, the earthquake-excited response of the UCLA Factor building is also presented to corroborate the performance of the proposed method with the computationally intensive SSI method. In the case of progressive or continuous damage, the proposed algorithm is first employed using numerical simulation. And it is observed that the proposed method is not capable of identifying the instantaneous frequencies (IF) of the axially-moving cantilever beam. Thereafter, the other two existing methods, the wavelet transform (WT) and Hilbert vibration decomposition (HVD), are utilized to identify the IFs of the axially-moving cantilever beam.

These two methods are applied on the experimental data of the axially-moving cantilever beam. The WT is able to identify the IFs through a simple ridge detection method. The HVD method is able to extract the first vibratory modal response with its corresponding IF but fails to extract the higher vibratory modes. It is observed that the HVD performs better if

the vibration signal is slow-varying in amplitude. The identified IFs obtained from the two methods are also compared with the frozen IFs. Even though proper extraction of the first modal response is achieved by the HVD, its corresponding identified IF resolution is not very accurate. Therefore, the HVD integrated with TVAR modeling is utilized to further improve the accuracy of the identified IF since the TVAR model gives freedom to predict the variance of the measurement noise in a signal and the variance of the process noise in the time-varying parameters of the signal.

## **5.2 Contributions**

The main contributions of this thesis are listed below.

- a) The SOBI method cannot separate the mixed modal responses; therefore, by employing the TVAR modeling, we can overcome this limitation of the SOBI method.
- b) The estimation of parameters of vibration signal with the TVAR modeling is computationally intensive since it involves relatively higher modal orders. Proper selection of model order is crucial in order to obtain minimum estimation error of the vibration signal. So, by utilizing the SOBI method first, we can now estimate individual components (i.e., modal responses) of the vibration signal with low model order. In this way we are eliminating the computational extensive work of selecting the proper model order.
- c) The proposed algorithm (i.e., SOBI plus HT) can identify the damage instant if the difference between the undamaged and damage frequencies is significant.
- d) The proposed algorithm (i.e., SOBI plus TVAR) can identify the damage instant more accurately compare to the HT method.

- e) Simple ridge tracking method in chapter 4, produces satisfactory results for identification of instantaneous frequencies, especially the lower instantaneous frequencies of the axially-moving cantilever beam.
- f) The HVD plus the TVAR method results in higher frequency resolution.

### **5.3 Future Works**

Further improvement of this research is needed. The following are some of the suggestions,

- The proposed algorithm is needed to be validated against low SNR value.
- The present research should be further extended to include the location of damage as well as prediction of damage given the existing damage situation at any point of interest.
- The proposed algorithm should be further exploited for the case of underdetermined damage detection (e.g., greater number of modes than the number of sensors).
- Windowing technique of the proposed algorithm should be explored for the case of progressive damage.

## References

- Amezquita-Sanchez, J. P., & Adeli, H. (2014). Synchrosqueezed wavelet transform-fractality model for locating, detecting, and quantifying damage in smart highrise building structures. *Smart Material and Structures*, 24, DOI:10.1088/0964-1726/24/6/065034.
- Antoni, J. (2005). Blind separation of vibration components: Principles and demonstration. *Mechanical Systems and Signal Processing*, 19, 1166-1180.
- Bao, C., Hao, H., & Li, Z.-X. (2013). Multi-stage identification scheme for detecting damage in structures under ambient excitations. *Smart Materials and Structures*, 22, DOI:10.1088/0964-1726/22/4/045006.
- Behmanesh, I., & Moaveni, B. (2014). Probabilistic identification of simulated damage on the Dowling Hall footbridge through Bayesian finite element model updating. *Structural Control and Health Monitoring*, DOI:10.1002/stc.1684.
- Belouchrani, A., Abed-Meraim, K., Cardoso, J., & Moulines, E. (1997). A blind source separation technique using second-order statistics. *IEEE Transactions on Signal Processing*, 45(2), 434-444.
- Bertha, M., & Golinval, J.-C. (2014). Identification of a Time-Varying Beam Using Hilbert Vibration Decomposition. *In Proceedings of IMAC XXXII*. Orlando.
- Bodeux, J. B., & Golinval, J. C. (2001). Application of ARMAV models to the identification and damage detection of mechanical and civil engineering structures. *Smart Materials and Structures: Institute of Physics Publishing*, 10, 479-489.
- Carden, E., & Fanning, P. (2004). Vibration-based condition monitoring: A review. *Structural Health Monitoring*, vol, 3(4), 355-377.
- Chao, S.-H., Loh, C.-H., & Tseng, M.-H. (2014). Structural damage assessment using output-only measurement: Localization and quantification. *Journal of intelligent Material Systems and Structures*, 25(9), 1097-1106.
- Chen, B., & Nagarajaiah, S. (2011). Observer-based structural damage detection using genetic algorithm. *Structural Control and Health Monitoring*, DOI:10.1002/stc.512.
- Chen, B., Chen, Z.-w., Wang, G.-j., & Xie, W.-p. (2014). Damage Detection on Sudden Stiffness Reduction Based on Discrete Wavelet Transform. *The Scientific World Journal, Hindawi Publishing Corporation*, 2014, 1-16.

- Chen, S.-F., Hung, T.-Y., & Loh, C.-H. (2015). Analysis of traffic-induced vibration and damage detection by blind source separation with application to bridge monitoring. *Sensors and Smart Structures Technologies for Civil, Mechanical, and Aerospace Systems*.
- Deng, L. (2002). *Modelling and Identification of an Axially Moving Cantilever Beam*. Thunder Bay, Ontario: Lakehead University.
- Doebling, S., Farrar, C., Prime, M., & Shevitz, D. (1996). Damage identification and health monitoring of structural and mechanical systems from changes in their vibration characteristics: A literature review, A Technical Report LA-1370-MS, LosAlamos National Laboratory, Los Alamos, NM.
- Dziedziech, K., Staszewski, W. J., & Uhl, T. (2015). Wavelet-based modal analysis for time-variant systems. *Mechanical Systems and Signal Processing*, 50-51, 323-337.
- Dziedziech, K., Staszewski, W. J., Basu, B., & Uhl, T. (2015). Wavelet-based detection of abrupt changes in natural frequencies of time-variant systems. *Mechanical Systems and Signal Processing*.
- Feldman, M. (2006). Time-varying vibration decomposition and analysis based on the Hilbert transform. *Journal of Sound and Vibration*, 295, 518-530.
- Feldman, M. (2011). Hilbert transform in vibration analysis. *Mechanical Systems and Signal Processing*, 25, 735-802.
- Feng, L., Yi, X., Zhu, D., Xie, X., & Wang, Y. (2015). Damage detection of metro tunnel structure through transmissibility function and cross correlation analysis using local excitation and measurement. *Mechanical Systems and Signal Processing*, 60-61, 59-74.
- Garcia, D., & Trendafilova, I. (2014). A multivariate data analysis approach towards vibration analysis and vibration-based damage assessment: Application for delamination detection in a composite beam. *Journal of Sound and Vibration*, 333, 7036-7050.

- Ghahari, S., Abazarsa, A., Ghannad, M., & Taciroglu, E. (2013). Response-only modal identification of structures using strong motion data. *Earthquake Engineering and Structural Dynamics*, 42(1), 1221-1242.
- Gnananathan, Q. (2005). *Control of Lateral Vibration of an Axially Moving Cantilever Beam Using Piezoelectric Actuators*. Thunder Bay, Ontario: Lakehead University.
- Hazra, B., & Narasimhan, S. (2010). Wavelet-based blind identification of the UCLA Factor building using ambient and earthquake responses. *Smart Materials and Structures*, 19(2), 025005.
- Hazra, B., Sadhu, A., Roffel, A., & Narasimhan, S. (2012). Hybrid time-frequency blind source separation towards ambient system identification of structures. *Computer Aided Civil and Infrastructure Engineering*, 27(5), 314-332.
- Hazra, B., Sadhu, A., Roffel, A., Paquet, P., & Narasimhan, S. (2012). Underdetermined blind identification of structure by using the modified cross-correlation method. *Journal of Engineering Mechanics, ASCE*, 138(4).
- Hsu, T.-Y., Huang, S.-K., Lu, K.-C., Loh, C.-H., Wang, Y., & Lynch, J. P. (2011). On-line structural damage localization and quantification using wireless sensors. *Smart Materials and Structures*, 20, DOI:10.1088/0964-1726/20/10/105025.
- Kerschen, G., Poncelet, F., & Golinval, J. (2007). Physical interpretation of independent component analysis in structural dynamics. *Mechanical Systems and Signal Processing*, 21, 1561-1575.
- Kesavan, K. N., & Kiremidjian, A. S. (2011). A wavelet-based damage diagnosis algorithm using principal component analysis. *Structural Control and Health Monitoring*, DOI:10.1002/stc.462.
- Kohler, M., Davis, M., & Safak, E. (2005). Earthquake and ambient vibration monitoring of the steel-frame UCLA Factor building, Earthquake Spectra. *Earthquake Engineering Research Institute*, 21(3), 1-22.

- Kunwar, A., Jha, R., Whelan, M., & Janoyan, K. (2013). Damage detection in an experimental bridge model using Hilbert-Huang transform of transient vibrations. *Structural Control and Health Monitoring*, 20, 1-15.
- Kuwabara, M., Yoshitomi, S., & Takewaki, I. (2012). A new approach to system identification and damage detection of high-rise buildings. *Structural Control and Health Monitoring*.
- Lin, S., Yang, J., & Zhou, L. (2005). Damage identification of a benchmark building for structural health monitoring. *Smart Materials and Structures, Institute of Physics Publishing*, 14, S162-S169.
- Liu, K. (June 2007). Parameter Identification of Linear Time-Varying Systems Using Wavelet Analysis. *The Proceedings of VS Tech 2007*. Lanzhou, China.
- Magalhaes, F., Cunha, A., & Caetano, E. (2012). Vibration based structural health monitoring of an arch bridge: From automated OMA to damage detection. *Mechanical Systems and Signal Processing*, 28, 212-228.
- Mita, A., & Thu, H. (2013). Damage Detection Method Using Support Vector Machine and First Three Natural Frequencies for Shear Structures. *Open Journal of Civil Engineering*, 3, 104-112.
- Nair, K., Kiremidjian, A., & Law, K. (2006). Time series-based damage detection and localization algorithm with application to the asce benchmark structure. *Journal of Sound and Vibration*, 291, 349-368.
- Nayeri, R., Masri, S., Ghanem, R., & Nigbor, R. (2008). A novel approach for the structural identification and monitoring of a full-scale 17-story building based on ambient vibration measurements. *Smart Materials and Structures*, 17(2), 1-19.
- Nguyen, D. (2009). Measuring Instantaneous Frequency of Local Field Potential Oscillations using the Kalman Smooth. *Journal of Neuroscience Method*, 187, 365-367.
- Noh, H. Y., Nair, K. K., & Kiremidjian, A. S. (2009). Application of time series based damage detection algorithms to the benchmark experiment at the National Center for

- Research on Earthquake Engineering (NCREE) in Taipei, Taiwan. *Smart Structures and Systems*, 5(1), 000.
- Park, J.-W., Sim, S.-H., & Jung, H.-J. (2013). Wireless sensor network for decentralized damage detection of building structures. *Smart Structures and Systems*, 12(3-4), 399-414.
- Peijun, S., & A.A., B. (1998). High-Resolution Instantaneous Frequency Estimation Based On Time-Varying AR Modeling. *IEEE*, 109-112.
- Poncelet, F., Kerschen, G., Golinval, J., & Verhelst, D. (2007). Output-only modal analysis using blind source separation techniques. *Mechanical Systems and Signal Processing*, 21(6), 2335-2358.
- Ramos, J., Reyes, J., & Barocio, E. (2014). An Improved Hilbert Vibration Decomposition Method for Analysis of Low Frequency Oscillations. *IEEE*.
- Ravi Shankar Reddy, G., & Rao, R. (2014). Non-stationary Signal Analysis using TVAR Model. *International Journal of Signal Processing, Image Processing and Pattern Recognition*, 7(2), 411-430.
- Rodriguez, R., Esobar, J. A., & Gomez, R. (2010). Damage detection in instrumented structures without baseline modal parameters. *Engineering Structures*, 32, 1715-1722.
- Rutten, C., Nguyen, V., & Golinval, J. (2011). Comparison of output-only methods for condition monitoring of industrials systems. *9th International Conference on Damage Assessment of Structures: Journal of Physics*. 305. Journal of Physics.
- Sadhu, A. (2013). *Decentralized Ambient System Identification of Structures, PhD Thesis, Univeristy of Waterloo*. Waterloo, Ontario, Canada.
- Sadhu, A., & Hazra, B. (2013). A novel damage detection algorithm using time-series analysis-based blind source. *Shock and Vibration, IOS Press*, 20(3), 423-438.
- Sadhu, A., Hazra, B., & Narasimhan, S. (2012). Blind identification of earthquake-excited structures. *Smart Materials and Structures, IOP Publishing*, 21(4), 045019.

- Sadhu, A., Hazra, B., & Narasimhan, S. (2013). Decentralized modal identification of structures using parallel factor decomposition and sparse blind source separation. *Mechanical Systems and Signal Processing*, *41*(1), 396-419.
- Sadhu, A., Narasimhan, S., & Goldack, A. (2014). Decentralized modal identification of a pony truss pedestrian bridge using wireless sensors. *Journal of Bridge Engineering*, *ASCE*, *19*(6).
- Skolnik, D., Lei, Y., Yu, E., & Wallace, J. (2006). Identification, model updating, and response prediction of an instrumented 15-storey steel-frame building. *Earthquake Spectra*, *Earthquake Engineering Research Institute*, *22*(3), 781-802.
- Spiridonakos, M., Yadav, N., & Chatzl, E. (2014). Identification and damage detection of a shear frame model based on a blind source separation method. *7th European Workshop on Structural Health Monitoring*.
- Su, W. C., Liu, C. Y., & Huang, C. S. (2014). Identification of Instantaneous Modal Parameter of Time-Varying System via a Wavelet-Based Approach and its Application. *Computer-Aided Civil and Infrastructure Engineering*, *29*, 279-298.
- Tibaduiza, D. A., Mujica, L. E., Rodellar, J., & Guemes, A. (2015). Structural damage detection using principal component analysis and damage indices. *Journal of Intelligent Material Systems and Structures*, 1-16.
- Wang, S., & Liu, M. (2009). The Study on the Acceleration Signal Processing Based on the TVAR Algorithm. *WASE International Conference on Information Engineering*, *191*, 70-73.
- Wang, Z. (2011). *Hilbert Transform Applications in Signal Analysis and Non-Parametric Identification of Linear and Nonlinear Systems*. Missouri University of Science and Technology.
- Xu, Y., & Chen, J. (2004). Structural Damage Detection Using Empirical Mode Decomposition: Experimental Investigation. *Journal of Engineering Mechanics*, *ASCE*, *130*, 1279-1288.

- Yan, A. -M., Kerschen, G., Boe, P. D., & Golinval, J. -C. (2005). Structural damage diagnosis under varying environmental conditions-part I: A linear analysis. *Mechanical Systems and Signal Processing*, *19*, 847-864.
- Yan, Y. J., Cheng, L., Wu, Z. Y., & Yam, L. H. (2007). Development in vibration-based structural damage detection technique. *Mechanical Systems and Signal Processing*, *21*, 2198-2211.
- Yang, J., Lei, Y., Wu, Z., & Huang, N. (2004). Hilbert-Huang based approach for structural damage detection. *Journal of Engineering Mechanics, ASCE*, *130(1)*, 85-95.
- Yang, Y., & Nagarajaiah, S. (2014). Blind identification of damage in time-varying systems using independent component analysis with wavelet transform. *Mechanical Systems and Signal Processing*, *47*, 3-20.
- Yao, R., & Pakzad, S. (2012). Autoregressive statistical pattern recognition algorithms for damage detection in civil structures. *Mechanical Systems and Signal Processing*, *31*, 355-368.
- Yun, G. J., Lee, S. G., Carletta, J., & Nagayama, T. (2011). Decentralized damage identification using wavelet signal analysis embedded on wireless smart sensors. *Engineering Structures*, *33*, 2162-2172.
- Zang, C., Friswell, M., & Imregun, M. (2004). Structural damage detection using independent component analysis. *Structural Health Monitoring*, *2*, 69-83.
- Zhou, Y. L., Figueiredo, E., Maia, N., Sampaio, R., & Perera, R. (2015). Damage detection in structures using transmissibility-based Mahalanobis distance. *Structural Control And Health Monitoring*.